

THE ROLE OF ACIDITY IN HETEROGENEOUS NICKEL CATALYSTS FOR
THE OLIGOMERIZATION OF LIGHT OLEFINS

by

Martin J. Menart

Copyright by Martin J. Menart 2018

All Rights Reserved

A thesis submitted to the Faculty and the Board of Trustees of the Colorado School of Mines in partial fulfillment of the requirements for the degree of Doctor of Philosophy (Applied Chemistry).

Golden, Colorado

Date: _____

Signed: _____
Martin J. Menart

Signed: _____
Dr. Ryan M. Richards
Thesis Advisor

Signed: _____
Dr. Jesse E. Hensley
Thesis Advisor

Golden, Colorado

Date: _____

Signed: _____
Dr. Thomas Gennett
Professor and Head
Department of Chemistry

ABSTRACT

Nickel supported on amorphous silica aluminas (ASAs) are promising catalysts for the oligomerization of light olefins to liquid fuels. They are readily prepared and utilized, possess high activity towards ethylene and propylene, and are made from earth-abundant, cost-effective, and commercially-available materials. The material properties of these catalysts were characterized by elemental analysis, TPR, NH₃ TPD, pyridine and CO DRIFTS, XAS, XPS, XRD, ²⁷Al MAS NMR, N₂ physisorption, and SEM imaging.

A representative dehydrated mixed alcohol stream containing a blend of ethylene and propylene in a 2.8:1 ratio was oligomerized using a fixed-bed reactor system at conditions of T_{reactor} = 120 °C, P_{total} = 200 psig, and WHSV = 0.75-1.0. Conversion and productivity values were determined by on-line GC analysis. Aromatic-free olefins in the C₄-C₁₄ range were produced over the catalysts at rates of 95-125 g kg_{cat}⁻¹ h⁻¹. Conversions values ranged between 7.2-11.9% and 29.8-34.0% for ethylene and propylene, respectively, with mass balances of 83-95%.

The formation of active nickel centers for ethylene conversion required the presence of anionic, Brønsted acidic support sites. Catalytic activity was further correlated with formation of reducible, Lewis acidic nickel sites. A comparison of two ASA supports having different aluminum content found their interactions with nickel to be substantially different. The incorporation of nickel on the more aluminum rich ASA produced more reducible nickel species, introduced greater Lewis acidity, and had a lower impact on Brønsted acidity. Despite these differences in nickel speciation, the Ni 2p_{3/2} peak in XPS appeared at 856.0 eV on both supports, indicative of an electronic environment similar to Ni(OH)₂.

By sum of *in situ* XAS and CO DRIFTS experiments, the active sites are proposed to be 5-coordinate nickel species that coordinate two ethylene molecules by release of a hemilabile support interaction. These hemilabile bond exchanges occur by interaction between nickel, terminal silanols, and coordinatively-flexible aluminum sites in ASA. This conclusion is supported by the disappearance of free silanols upon binding of Ni cations by CO, perturbations in the EXAFS fits of nickel upon ethylene exposure without change in coordination number, and changes in the coordination of Al upon dehydration and nickel incorporation.

TABLE OF CONTENTS

ABSTRACT.....	iii
LIST OF FIGURES	x
LIST OF TABLES	xv
ACKNOWLEDGEMENTS.....	xvii
CHAPTER 1 INTRODUCTION.....	1
1.1 Fuels from Biomass.....	1
1.1.1 International Goals for Biofuel Production	2
1.1.2 Targeting Fuels from Pyrolysis Oil	5
1.1.3 Gasoline Specifications	8
1.1.4 Diesel Specifications	10
1.1.5 Jet Specifications	11
1.1.6 Requirements for Converting Biomass Intermediates to Fuels	12
1.1.7 Comparing Conversion Product Properties to Fuel Specifications	12
1.1.8 Promising Strategies for Pyrolysis Oil Upgrading	12
1.1.9 Other Upgrading Considerations	13
1.2 The Oligomerization of Light Olefins by Heterogeneous Catalysts	14
1.2.1 Mechanisms for the Oligomerization of Ethylene and Higher Olefins	16
1.2.2 On the Nature of Active Sites for Olefin Oligomerization.....	20
1.2.3 The Co-monomer Effect.....	23

1.3	Goals and Structure of Thesis	25
1.4	Expected Impact.....	25
CHAPTER 2	INTERPRETING NICKEL ACTIVE SITES IN HETEROGENEOUS OLIGOMERIZATION CATALYSTS.....	26
2.1	Introduction	26
2.2	Experimental	28
2.2.1	<i>In situ</i> X-ray Absorption Spectroscopy	28
2.2.2	Model Compound Synthesis.....	29
2.2.3	Nickel Catalyst Synthesis	30
2.2.4	Thermogravimetric Analysis	30
2.2.5	N ₂ Physisorption.....	30
2.2.6	NH ₃ -TPD and TPR.....	31
2.2.7	X-ray Diffraction	31
2.2.8	Solid-state ²⁷ Al MAS NMR.....	32
2.2.9	Pyridine and CO DRIFTS	32
2.2.10	Crystal Structure Models.....	33
2.3	Results.....	33
2.3.1	TPR.....	33
2.3.2	Solid State ²⁷ Al MAS NMR	35
2.3.3	Synthesis of XAS Model Compounds.....	37
2.3.4	X-ray Absorption Spectroscopy	44

2.3.5	DRIFTS Experiments	57
2.4	Discussion	70
2.5	Conclusions	75
2.6	Acknowledgements	76
CHAPTER 3	THE OLIGOMERIZATION OF LIGHT OLEFINS	77
3.1	Introduction	77
3.2	Methods and Materials	79
3.2.1	Catalyst Synthesis.....	80
3.2.2	Catalyst Characterization.....	80
3.2.3	Reaction Testing.....	83
3.2.4	Catalyst Cost Estimates	85
3.3	Results	85
3.3.1	Support Study Characterization.....	85
3.3.2	Support Study Catalytic Performance	87
3.3.3	Techno-Economic Analysis of Supported Nickel Catalysts	90
3.3.4	Influence of Synthesis Conditions on Ni/ASA Material Properties	91
3.3.5	Relation of Material Properties to Catalytic Performance	94
3.3.6	Effect of Aluminum Content in Amorphous Silica Alumina Supports.....	99
3.3.7	Catalytic Properties of the ASA Supports	107
3.4	Discussion	108

3.5	Conclusion.....	111
3.6	Acknowledgements	111
CHAPTER 4	RU-SN/AC FOR THE AQUEOUS PHASE REDUCTION OF SUCCINIC ACID TO 1,4-BUTANEDIOL UNDER CONTINUOUS PROCESS CONDITIONS	113
4.1	Abstract	113
4.2	Catalyst Synthesis	115
4.3	Chemisorption Methods	116
4.4	CO and H ₂ Affinity and TPRs of Bifunctional Catalysts	116
4.5	Conclusion.....	120
4.6	Author Information	120
4.7	Acknowledgements	121
CHAPTER 5	<i>CIS,CIS</i> -MUCONIC ACID: SEPARATION AND CATALYSIS TO BIO- ADIPIC ACID FOR NYLON-6,6 POLYMERIZATION	122
5.1	Abstract	122
5.2	Catalyst Synthesis	123
5.3	Chemisorption Methods	125
5.4	Chemisorption Results	126
5.5	Conclusion.....	127
5.6	Author Information	127
5.7	Acknowledgements	128
CHAPTER 6	DEACTIVATION OF MULTILAYERED MFI NANOSHEET ZEOLITE DURING UPGRADING OF BIOMASS PYROLYSIS VAPORS.....	129

6.1	Abstract	129
6.2	Chemisorption and DRIFTS Methods.....	130
6.3	Results	131
6.4	Conclusion.....	132
6.5	Author Information	132
6.6	Acknowledgements	132
CHAPTER 7	SUMMARY, CONCLUSIONS, AND FUTURE WORK.....	133
7.1	Summary and Conclusions.....	133
7.2	Future Work	136
REFERENCES	139
APPENDIX A	PERMISSIONS	154

LIST OF FIGURES

Figure 1.1	U.S. transportation fuel consumption by type for 2009 to 2014 ⁵ , with projected values for 2020, 2030, and 2040 based on the reference case predictions from the Annual Energy Outlook for 2015. ⁶	2
Figure 1.2	U.S. renewable fuel production set by the Renewable Fuel Standard for 2010 to 2022. ⁵	4
Figure 1.3	Cost of upgrading pyrolysis oil by hydrotreatment as a function of oxygen content in the final product. Reproduced from McCormick et al. ¹³	6
Figure 1.4	Oxygenates present in pyrolysis oil and their distillation fraction. Reproduced from Christensen et al. ¹⁷	7
Figure 1.5	Structure of synthetic iso-paraffin farnesane.	11
Figure 1.6	Schematic catalytic cycle of ethylene dimerization and 1-butene isomerization. Reproduced from de Souza et al. ⁴²	16
Figure 1.7	Main reaction pathways for the oligomerization of ethylene and higher oligomers over Ni-exchanged molecular sieves. Reproduced from Lallemand et al. ⁴³	17
Figure 1.8	Proposed mechanism for co-oligomerization separate site mechanism.	18
Figure 1.9	Proposed mechanism for co-oligomerization over only Ni cation sites.	18
Figure 1.10	Proposed mechanism for co-oligomerization over only Brønsted acid sites.	19
Figure 1.11	The oligomerization of ethylene by cationic nickel when stabilized by an agostic interaction with a β -hydrogen of the growing carbon chain. Reproduced from Brogaard et al. ⁴⁴	20
Figure 1.12	The effect of site poisoning a NiSO ₄ /Al ₂ O ₃ catalyst with NaOH on the conversion of ethylene, propylene, and butene. Reproduced from Cai. ⁵⁴	21
Figure 1.13	Models of three-coordinated (left) and four-coordinated (right) Ni cations in silica MCM-41. The nickel, silicon, oxygen, and hydrogen atoms are depicted in blue, yellow, red, and white, respectively. Reproduced from Tanaka et al. ⁷⁰	24

Figure 2.1	Temperature-programmed reduction profiles of the ASA support and Ni catalysts.	34
Figure 2.2	^{27}Al MAS NMR spectra of ASA before and after nickel incorporation.	36
Figure 2.3	XRD pattern of model compound NiCr_2O_4	38
Figure 2.4	Filtered (left) and centrifuged (right) KNiPO_4 hydrate prior to calcination.....	39
Figure 2.5	Filtered (left) and centrifuged (right) KNiPO_4 after calcination.	40
Figure 2.6	XRD pattern of the calcined model compound KNiPO_4 obtained from the centrifuged supernatant.	41
Figure 2.7	XRD pattern of calcined model compound KNiPO_4 obtained from filtered crystals.....	42
Figure 2.8	Crystal structure of NiO . Nickel is depicted as gray spheres, and oxygen as red spheres.	42
Figure 2.9	Crystal structure of KNiPO_4 . Nickel is depicted as gray spheres, oxygen as red spheres, potassium as dark purple spheres, and phosphorous as light purple spheres.	43
Figure 2.10	Crystal structure of NiCr_2O_4 . Nickel is depicted as gray spheres, oxygen as red spheres, and chromium as blue spheres.	43
Figure 2.11	Ni K-edge XAS spectra for model compounds NiCr_2O_4 , KNiPO_4 , and NiO	44
Figure 2.12	Ni K-edge XAS spectra for catalyst samples Ni/SiO_2 , $\text{Ni/Al}_2\text{O}_3$, Ni/Al-MCM-41 , Ni/ASA	46
Figure 2.13	High-resolution Ni K-edge pre-edge features for model compounds NiCr_2O_4 , KNiPO_4 , and NiO	46
Figure 2.14	High-resolution Ni K-edge pre-edge features for catalysts Ni/SiO_2 , $\text{Ni/Al}_2\text{O}_3$, Ni/Al-MCM-41 , Ni/ASA , and Ni+Na/ASA	47
Figure 2.15	Plot of pre-edge information for the model compounds (red circles) and catalysts (black triangles) showing relation between coordination number and pre-edge properties.	48

Figure 2.16	Fitted EXAFS nearest-neighbor distance and pre-edge intensity of the model compounds (red circles) and catalysts (black triangles).....	50
Figure 2.17	High-resolution Ni K pre-edge features for catalysts after exposure to ethylene. Spectra of the pretreated catalysts before exposure to ethylene are shown in gray.....	50
Figure 2.18	Magnitude of the Fourier-transform of the Ni K-edge EXAFS spectra of the model compounds.	51
Figure 2.19	Magnitude of the Fourier-transform of the Ni K-edge EXAFS spectra of the pretreated catalysts.	53
Figure 2.20	Magnitude of the EXAFS Fourier-transform of Ni/SiO ₂ before and after exposure to ethylene.....	53
Figure 2.21	Magnitude of the EXAFS Fourier-transform of Ni/Al ₂ O ₃ before and after exposure to ethylene.....	54
Figure 2.22	Magnitude of the EXAFS Fourier-transform of Ni/ASA before and after exposure to ethylene.....	55
Figure 2.23	Magnitude of the EXAFS Fourier-transform of Ni+Na/ASA before and after exposure to ethylene.....	56
Figure 2.24	Magnitude of the EXAFS Fourier-transform of Ni/Al-MCM-41 before and after exposure to ethylene.....	56
Figure 2.25	Difference spectra of the CO ₂ infrared stretching region on activated (black) and reduced (red) Ni/ASA catalyst samples at low (dotted), medium (dashed), and high (solid) degrees of CO saturation at <i>ca.</i> -100 °C and low (<100 mbar) total pressure.	60
Figure 2.26	Difference spectra of CO infrared stretching region on activated (black) and reduced (red) Ni/ASA catalyst samples at low (dotted), medium (dashed), and high (solid) degrees of CO saturation at <i>ca.</i> -100 °C and low (<100 mbar) total pressure.....	66
Figure 2.27	Difference spectra of hydroxyl infrared stretching region on activated (black) and reduced (red) Ni/ASA catalyst samples at low (dotted), medium (dashed), and high (solid) degrees of CO saturation at <i>ca.</i> -100 °C and low (<100 mbar) total pressure.	69

Figure 2.28	Proposed active site structure for nickel catalysts involving hemilabile function of adjacent aluminum and terminal silanols.....	72
Figure 3.1	Schematic catalytic cycle of ethylene dimerization and 1-butene isomerization. Reproduced from de Souza et al. ¹⁵¹	78
Figure 3.2	X-ray diffraction patterns of nickel supported on ASA ₂₅ , MgO, and TiO ₂ supports. The peak positiond of the NiO and MgO (111), (200), and (220) facets are marked by asterisks.	86
Figure 3.3	Condensed liquid product composition for mixed olefin and pure ethylene feed streams over Ni/ASA ₂₅ . Mixed feed conditions: 120 °C, 200 psig, 0.75 WHSV. Ethylene feed conditions: 120 °C, 450 psig, 0.5 WHSV.	90
Figure 3.4	Impact of acidity types and sodium exchange on ethylene conversion.	95
Figure 3.5	Conversion of ethylene with respect to estimated nickel content.	96
Figure 3.6	Impact of acidity types and sodium exchange on propylene conversion.	97
Figure 3.7	Conversion of propylene as a function of nickel content for ASA.	98
Figure 3.8	Effect of nickel content on Brønsted to Lewis acid site ratio of Davicat catalyst as determined by pyridine-DRIFTS experiments.....	99
Figure 3.9	SEM of nickel supported on ASA ₁₅ and ASA ₂₅ silica-aluminas.	100
Figure 3.10	²⁷ Al MAS NMR spectra of ASA supports, BEA zeolite, and Al-MCM-41.	101
Figure 3.11	²⁷ Al MAS NMR spectra of Ni/ASA ₂₅ before and after drying.	102
Figure 3.12	TPR profiles comparing low-loading Ni after background subtraction of each support, respectively.....	105
Figure 3.13	X-ray photoelectron spectra of nickel-containing samples normalized to the Ni 2p _{1/2} peak intensity with binding energy positions of Ni(OH) ₂ , NiO, and Ni ⁰ as reported in Biesinger et al. ¹⁶¹ and of NiAl ₂ O ₄ as reported in Li et al. ¹⁶²	106
Figure 3.14	Raw X-ray photoelectron spectra of nickel-containing samples.....	107
Figure 4.1	Characterization of the Ru-Sn (1:1) and Ru powder activated carbon catalysts by temperature-programmed reduction.	119

Figure 4.2 High temperature TPR profile of Ru-Sn/PAC and inert control. 119

LIST OF TABLES

Table 1.1	Granted and conditionally granted waiver requests for oxygenate-containing fuels or fuel additives. ²⁰	10
Table 2.1	Literature values for surface-bound CO infrared peak positions.	64
Table 2.2	Literature values for surface hydroxyl infrared peak positions.....	68
Table 3.1	Surface area and acidic properties of ASA ₂₅ , TiO ₂ , and MgO supports.	86
Table 3.2	Reactor temperature (T) and pressure (P), conversion (X), selectivity of liquid products (S), and productivity values based on combined gas and liquid sample yields.	88
Table 3.3	Synthesis cost in 2015 dollars of nickel cation-type catalysts used for oligomerization based on an annual production scale of 1,000,000 lbs.....	91
Table 3.4	Reflux conditions, element content, and textural properties of the catalysts used for the synthesis conditions study.	92
Table 3.5	Effect of nickel incorporation on acid properties of the ASA ₂₅ -supported catalysts used for the synthesis conditions study.	93
Table 3.6	Conversion values of ethylene (X _{C2}) and propylene (X _{C3}), productivity to C ₄ -C ₇ products, and mass balances (MB) for Ni/ASA ₂₅ catalysts at TOS = 5 h, WHSV = 1, T = 120 °C, and P _{total} = 200 psig.	94
Table 3.7	Reflux conditions, element content, and textural properties of the ASAs.	100
Table 3.8	Acid properties of the ASA ₁₅ - and ASA ₂₅ -supported catalysts.....	103
Table 4.1	H ₂ chemisorption of fresh monometallic catalysts used in batch screening reactions for succinic acid reduction to BDO.	117
Table 4.2	Properties of fresh powder bimetallic catalysts used in batch screening reactions for succinic acid reduction to BDO.	118
Table 5.1	Metal dispersion based on chemisorption and metal content determined by ICP for the virgin activated carbon (AC) and silica powdered catalysts used in batch screening reactions for muconic acid hydrogenation.	126

Table 5.2	Metal content and dispersion of the fresh and post-reaction 1% Rh/AC granule catalyst used in the 100 h time-on-stream stability test for muconic acid hydrogenation.....	127
Table 6.1	Quantified acid sites and Brønsted to Lewis ratios of fresh and recovered MFI nanosheet and HZSM-5 samples after exposure to 5, 25, and 50 doses of cellulose during MBMS experiments.....	131

ACKNOWLEDGEMENTS

This work could not have been completed without the help and guidance of many people. First, I extend my immense gratitude to my advisors, Dr. Jesse Hensley and Professor Ryan Richards, who provided me their full support and encouragement, and patiently granted me great freedom and trust to pursue my research. Their guidance has aided me through professional, personal, and technical challenges alike. Through his zenful mentorship, Prof. Richards has instilled in me the importance of scientific outreach, community, and collaboration; his influence will forever be a part of my outlook as a scientist. I give my unending gratitude to Dr. Jesse Hensley. From my days as a SULI intern through my pursuit of a doctorate, Jesse has always given me his candid advice, critical input, and full support. I thank my thesis committee: Prof. Brian Trewyn, Prof. Mark Seger, and Prof. Moises Carreon for their challenging input and thought-provoking discussions on the direction of my research.

I acknowledge together the collective teams of Professors Richards, Trewyn, and Pylypenko at the Colorado School of Mines, who have fostered here a close community of researchers in heterogeneous catalysis. I thank the alumni of the Richards' group, Dr. Chris Cadigan, Dr. Chris Caskey, Dr. Jeremy Leong, Dr. Mengze Xu, and Dr. Sarah Shulda, who have been instrumental in the continuity of our group's knowledge and a source of guidance towards finishing my Ph.D. Thank you to all the current group members, Sam Gage, Amy Settle, Allie York, Luke Williams, and Samantha Medina for the time we share discussing research, revising presentations, and maintaining morale.

My appreciation goes out to the members of the Trewyn group, Megan Moyer, Malcolm Davidson, and Dr. Sridhar Budhi for their thoughtful insights and interesting collaborations on chemisorption. I would like to thank Prof. Svitlana Pylypenko, Mike Dzara, and Sam Gage for

contributing their expertise with XPS to my work. I acknowledge Ed Dempsey, Megan Rose, and Jeremiah Mashore for their earnest support in all manners technical and administrative. I thank the Department of Chemistry, Dr. Barbara Moskal, and Vertical Skills Academy for their financial support and the opportunity to lead outreach and teaching events for a great number of earnest young students. My appreciation goes to Profs. Allison Caster, Renee Falconer, Mark Seger, and Mark Eberhart for their excellence as teaching mentors, and to Joe Stranahan for assisting me with preparing an untold amount of chemicals for science shows.

I extend my heartfelt thanks to the many individuals in the National Bioenergy Center at the National Renewable Energy Laboratory whom I have had the rewarding experience of working with. I thank Dr. Josh Schaidle and Dr. Dan Ruddy for their thoughtful oversight in the synthesis, planning, and execution of my thesis work. I give special thanks to Dr. Singfoong Cheah and Dr. Jeff Miller for all their help and contributions with XAS experiments. I thank Dr. Derek Vardon and Dr. Gregg Beckham for the opportunity to contribute towards projects that could only be described as beyond ambitious in terms of scope and collaboration. I thank Dr. Michael Griffin, Dr. Susan Habas, Dr. Matthew Yung, Dr. Erick White, Connor Nash, and Jason Thibodeaux for their assistance and advice on all manners of catalyst characterization, product analysis, and reactor operation. I also thank Dr. Frederick Baddour, Dr. Kurt Van Allsburg, and Mary O'Connor for their thoughtful discussions and mutual appreciation of caffeine.

Finally, I thank deeply my family and friends, whose love and encouragement have nourished me and kept me whole along the way.

“c'est en forgeant qu'on devient forgeron”

“it is by forging that one becomes a smith”

-French proverb

Dedicated to my loving parents, Stephen and Merline, who have encouraged
and supported me along every step of this journey.

CHAPTER 1

INTRODUCTION

1.1 Fuels from Biomass

Liquid fuels derived from petroleum possess high energy density, flexibility to varied operating conditions, and proven compatibility with today's infrastructure.¹ However, concerns over global climate change as a result of combustion and the long term availability of the resource has prompted demand for alternatives. Heavy trucks and air traffic are confined to liquid fuels and will be so for the foreseeable future. Extensive infrastructure exists to process and consume liquid fuels. It is therefore desirable to develop renewable liquid fuels with properties like today's gasoline, diesel, and jet as we transition away from fossil fuel dependence. Biomass is likely to be the only renewable carbon source available for the production of these liquid fuels.² A U.S. Department of Energy study indicated that more than 1.3 billion tons of sustainable and primarily lignocellulosic biomass could be harvested for biofuel production by 2030.³

Biomass can provide unique intermediates to fuels, with several processing pathways enabling varying degrees of specificity in products and harshness in operating conditions. The intrinsic oxygen content of biomass sets it apart from standing infrastructure for energy consumption, production, and distribution in transportation applications. At the intersect of oxygenated, bio-derived compounds, and the petroleum-based, hydrocarbon fuels of today, lies a poorly defined middle ground where opportunities exist for advancement in fuels, engines, and sustainable energy for transportation. This review seeks to engage each of those areas of understanding, and points to relevant catalytic methods for producing suitable fuels from

biomass that may or may not directly mimic the purely hydrocarbon sources of today.

1.1.1 International Goals for Biofuel Production

By estimate of the International Energy Agency, biofuels have the global potential to displace 27% of petroleum fuels for transportation by 2050, thereby accomplishing a 20% reduction in GHG emissions for this sector.⁴ This degree of implementation will require a rapid change in fuel-producing infrastructure, as present consumption rates of petroleum-based fuels are substantial. Figure 1.1 shows transportation fuel consumption in the U.S. by fuel type for the period of 2009 to 2014⁵, with projected values for 2020, 2030, and 2040 based on the reference case predictions from the Energy Information Administration’s Annual Energy Outlook for 2015.⁶

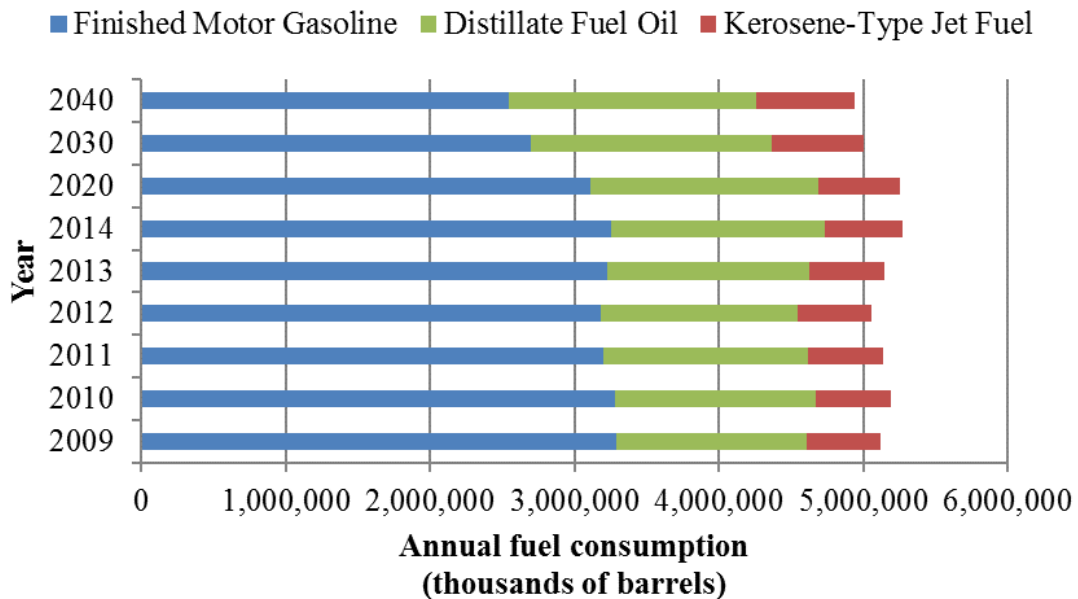


Figure 1.1 U.S. transportation fuel consumption by type for 2009 to 2014⁵, with projected values for 2020, 2030, and 2040 based on the reference case predictions from the Annual Energy Outlook for 2015.⁶

Total fuel consumption was relatively constant from 2009 to 2014 at approximately 5 billion barrels per year of finished fuels and is predicted to decrease by only 5% by 2040. On an energetic basis, transportation in the U.S. and OECD Europe (those part of the Organization for Economic Co-operation and Development) amounted to 26.9 and 17.7 quadrillion BTUs, respectively, in 2013. On a global basis, the demand for energy for transportation was 96.2 quadrillion BTUs.⁷

Presently, diesel and jet represent almost 40% of U.S. transportation fuel consumption. Looking forward to 2040, the gasoline market share in the U.S. is expected to decline by 20%. Meanwhile, demands for diesel and jet fuel are expected to increase by 20% and 30%, respectively. These changes in market share are expected to arise from advancements in vehicle technologies which displace gasoline, with a greater share of hybrid, flex-fuel, diesel, and electric vehicles being deployed.⁶ Given these market projections, and the relative difficulty in deploying alternatives to liquid fuels for diesel and jet applications, technologies that enable biodiesel and biojet production from biomass will be the most important.

An estimated 20% of GHG emissions in the EU are from transportation.⁸ In an effort to reduce this contribution, The European Commission's Renewable Energy Directive for 2009 through 2028 targets 10% of transportation to be bio-fuel powered by 2020.⁸ Additionally, the Fuel Quality Directive for 2009 to 2030 aims to achieve a 6% reduction of transport fuel-derived GHG emissions within the same timeframe.⁹ Recognizing a competition between food and fuel agriculture, this directive further states that those biofuels produced from cereals and other starch rich crops, sugars, and oil crops are limited to be no more than 5% of transportation fuels used in the EU. Furthermore, this amendment would define a life cycle analysis-based sustainability criterion for biofuels.

Similarly, the U.S. has set expectations for renewable fuel production under the Renewable Fuel Standard (RFS2), part of the Energy Independence and Security Act of 2007.¹⁰ Figure 1.2 presents U.S. renewable fuel production goals based on RFS2. A minimum of 36 billion gallons of renewable biofuels are to be produced and sold per year by 2022.

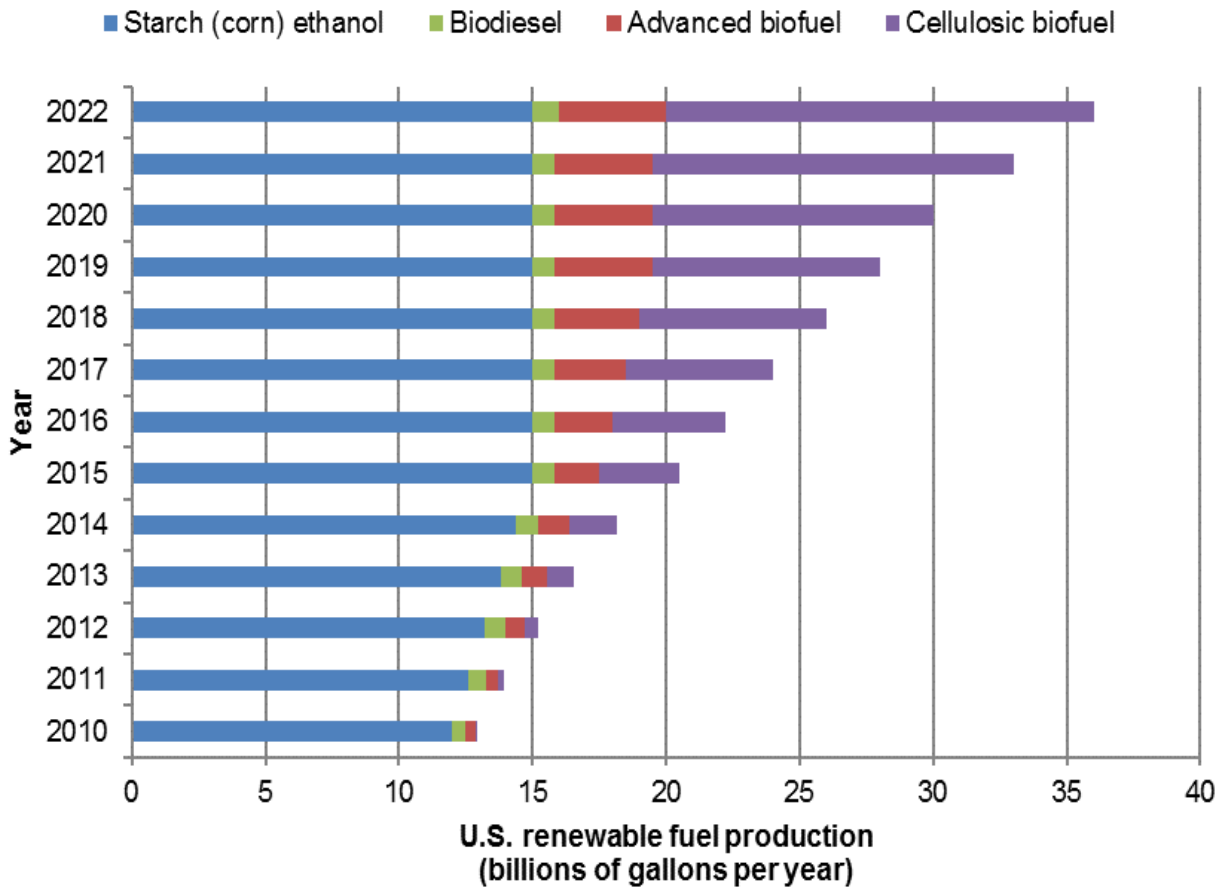


Figure 1.2 U.S. renewable fuel production set by the Renewable Fuel Standard for 2010 to 2022.⁵

Advanced biofuels, or those that reduce GHG emission by at least 50% relative to petroleum-based fuels, will contribute 21 billion gallons to the total volume. Cellulosic biofuels are an additional class of biofuels nested into advanced biofuels, are those which are produced

from renewably-derived cellulose, hemicellulose, and/or lignin and reduce GHG emissions by at least 60%. This class of biofuels is expected to reach production levels comparable to corn ethanol by 2022. Cellulosic feedstocks approved by the EPA include crop residue, slash, forest residue, annual cover crops, yard waste, food waste, and municipal solid waste.

In 2013, the production of renewable fuels in the U.S. consisted of primarily corn ethanol blended with gasoline. This amounted to 12% of gasoline consumption and 7% of all transportation fuels. Based on predictions from the Annual Energy Outlook, RFS2 expectations for renewable fuel production will increase to 12% of *total* transportation fuel consumption in 2020. Given these blending rates and that the GHG emissions from traditional corn ethanol are estimated to be 19% lower than conventional gasoline¹¹, the overall reduction in GHG emissions will be approximately 5%. These estimates put the U.S. and EU on a similar footing for expected contributions by liquid renewable fuels to the transportation energy market.

1.1.2 Targeting Fuels from Pyrolysis Oil

The fuel properties of pyrolysis oil can be improved through hydrotreating, where hydrogen is co-fed to a reactor at high temperatures in the presence of a catalyst. By this means, oxygen is removed from the oil. However, costs increase rapidly as more hydrogen is added,¹² as shown in Figure 1.3. Consequently, it is desirable to retain as much oxygen as possible, while still obtaining sufficient fuel properties in the finished product. It is unlikely that a single process will be able to take a pyrolysis oil inlet stream and selectively produce desirable compounds. A more realistic strategy is to understand the primary compounds in pyrolysis oils, identify what is causing the discrepancy between their properties and those mandated by fuel regulations, and develop processes capable of upgrading subsets of pyrolysis compounds to create viable fuels.

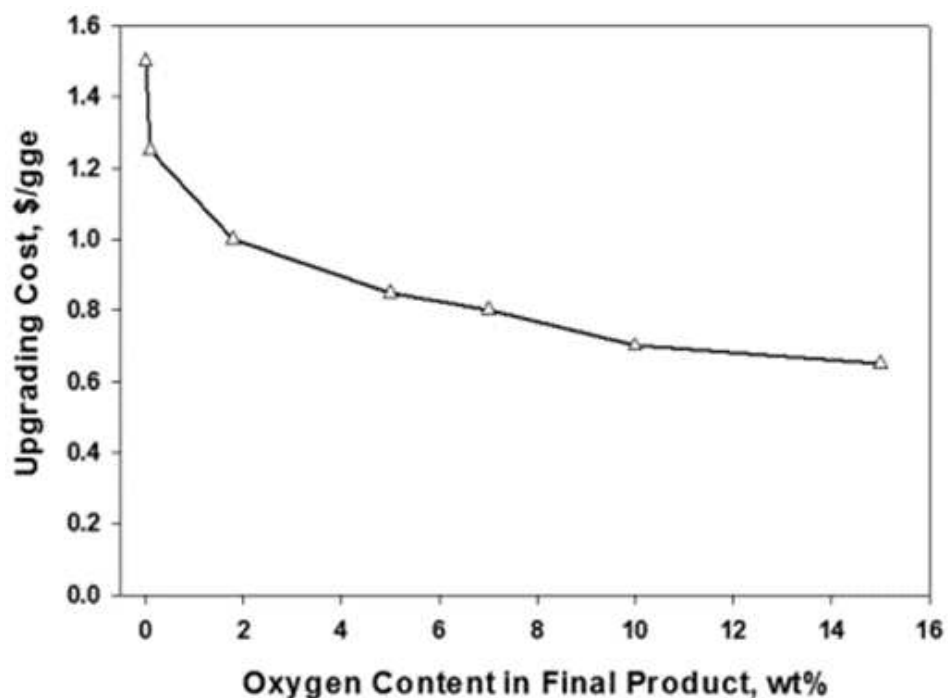


Figure 1.3 Cost of upgrading pyrolysis oil by hydrotreatment as a function of oxygen content in the final product. Reproduced from McCormick et al.¹²

McCormick and co-workers have analysed hydrotreated pyrolysis oil and determined the oxygenated compounds present in the various distillate fractions.¹³ The primary components found in this study and their boiling fraction are shown in Figure 1.4. The low boiling components consisted primarily of furans, namely 2,5-dimethylfuran, methyltetrahydrofuran, and 2-methylfuran. Higher boiling species were almost solely aromatic in nature, with the products being identified as mainly derivatives of phenol, guaiacol, and anisole.¹² Taldmadge et al. considered integration of pyrolysis hydrotreating into a refinery.¹⁴ Climent et al. defined a series of routes from platform molecules such as levulinic acid, fatty acids, and polyols to fuel additives by combining oxygen removal processes with molecular weight adjustment *via* C-C coupling reactions.¹⁵ Corma et al. investigated routes from the molecule Sylvan (2-methylfuran) to diesel fuel.¹⁶

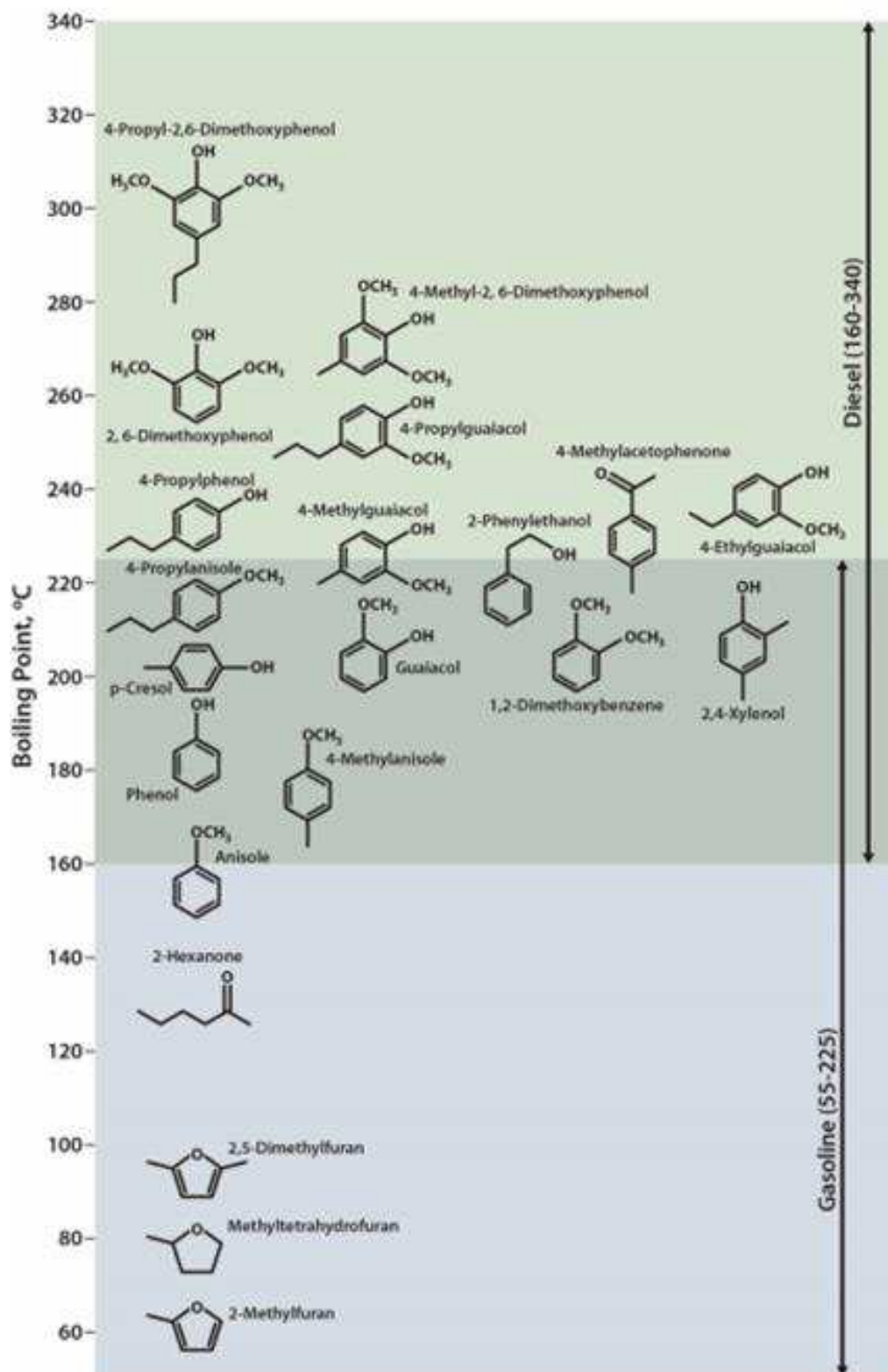


Figure 1.4 Oxygenates present in pyrolysis oil and their distillation fraction. Reproduced from McCormick et al.¹²

1.1.3 Gasoline Specifications

All liquid fuels must meet current fuel specifications regardless of origin if used neat or as a blendstock. In the U.S., biofuels must either meet these specifications or obtain an EPA-approved waiver. The American Society for Testing and Materials (ASTM) publishes transportation fuel standards in the United States. The European Committee for Standardization (CEN) publishes analogous standards in Europe. The European Union most recently defined its fuel specifications in Fuel Quality Directive for 2009 to 2030.

The ASTM gasoline standard (D4814) describes five distillate classes.¹⁷ The classes are ranked by their vapor pressure at 100 °F, or Reid vapor pressure (RVP). Class AA has the lowest RVP at a maximum of 54 kPa while Class E has the highest at 103 kPa. Each class must follow a distillation schedule with maximum temperature requirements for 10, 50, 90 vol%, and complete evaporation. A maximum of 2 vol% residue may remain. The Driveability Index (DI) is used to ensure compatibility between different distillate classes and ethanol contents to ensure cold start and warm-up driveability, given ethanol's low vapor pressure at cold temperatures. All distillate classes must meet additional criteria for lead, sulfur, and gum impurities, copper corrosiveness, and oxidative stability. The high end of volatility in gasoline is regulated to prevent vapor lock, a condition where fuel vaporizes in the fuel line and shuts down the engine. No gasoline sold in the U.S. may contain benzene in concentrations higher than 0.62% by volume. In the EU, benzene may be present in concentrations up to 1%.⁹ Additionally, the fuel must contain less than 35% aromatics and 18% olefins.

The antiknock rating is a fuel's ability to resist autoignition ahead of the flame front initiated by the spark, also called knocking or ping. Severe knocking results in loss of power and can damage engines over time. The antiknock index (AKI) is the arithmetic average of this rating

measured in the lab (RON) and on the road (MON) relative to isooctane. Most vehicles on the road today can use fuel with an AKI of 87. This restriction is relaxed at higher altitude because the air-fuel mixture has lower density in the cylinder, with fuels having octane ratings as low as 84 may be sold in the mountains.¹⁷

The Substantially Similar Rule originates in the Clean Air Act, section 211(f), and prohibits use of any fuel or fuel additive that is not substantially similar to current fuel unless a waiver is obtained by the EPA.¹⁸ Specifically, the fuel must be composed of carbon, hydrogen, oxygen, nitrogen, or sulfur and be some combination of hydrocarbons, aliphatic ethers, or aliphatic alcohols. The fuel may be up to 0.3 vol% methanol, or up to 2.75 vol% methanol with an equal volume of butanol or larger alcohol. The fuel must not contain more than 2.0 wt% oxygen, unless the fuel contains aliphatic ethers and/or alcohols (excluding methanol) in which it may be up to 2.7 wt% oxygen. In addition, the fuel must meet ASTM D4814 gasoline standards. Exceptions to this rule, such as E10 with an oxygen content of 3.5 wt%, may be obtained through EPA waiver.

Granted waiver requests for oxygen-containing fuels or fuel additives that differ from section 211(f) of the Clean Air Act “substantially similar” clause are shown in Table 1.1.¹⁹ Presently, the list of approved oxygenates includes C₁-C₈ alcohols and methyl tert-butyl ether (MTBE). Most applications were filed between the late 1970’s and late 1980’s. The only waiver to be processed in the last twenty-five years is that of 15% ethanol, or E15. Submitted by Growth Energy on behalf of 52 U.S. ethanol manufacturers, E15 was granted a partial waiver in 2010.

Table 1.1 Granted and conditionally granted waiver requests for oxygenate-containing fuels or fuel additives.¹⁹

Applicant	Fuel or additive	Year
Growth Energy	Ethanol (15%)	2011
Sun Refining and Marketing Co.	MTBE (15%)	1988
Texas Methanol Corp.	Methanol (5%), C ₂ -C ₈ cosolvent alcohols (2.5%), specified corrosion inhibitor	1988
E.I. DuPont de Nemours & Company	Methanol (5%), cosolvent alcohols (2.5%), specified corrosion inhibitor	1985
Synco 76 Fuel Corp.	Ethanol (10%), proprietary additive	1982
ARCO	Methanol and TBA (up to 4.75%, limit of 3.5% oxygen)	1981
Sun Petroleum Products Co.	Methanol and TBA (0-5.5%)	1979
ARCO	MTBE (0-7%)	1979
ARCO	TBA (0-7%)	1979
Gas Plus, Inc.	Anhydrous ethanol (0-10%)	1978

1.1.4 Diesel Specifications

Diesel fuel oils are defined by seven grades on the basis of distillate weight and sulfur content.²⁰ Applications of each fuel are load-based. For example, Grade No. 2-D S15 is a general purpose, middle distillate fuel suitable for conditions of varying speed and load while Grade No. 4-D is a blend of heavy distillate and residual oil for low- and medium-speed engines under constant load.

The requirements for each grade are flash point, cloud point, water and sediment, carbon residue, ash, distillation, sulfur, copper corrosion, cetane number, cetane index, aromaticity, lubricity, and conductivity. The purpose of each property may be discussed in groups where performance, safety concerns, or environmental concerns dictate the specification.

1.1.5 Jet Specifications

Jet specification D1655 defines fit-for-purpose performance metrics for fuels produced from petroleum, oil sand, or shale derived feedstocks.²¹ At present, only two alternative feedstocks have endured sufficient testing to allow separate specification under standard D7566. These fuels are hydroprocessed synthesized paraffinic kerosene (SPK) produced via Fischer-Tropsch chemistry and hydroprocessed esters and fatty acids (HEFA).²² There is no basis to assume that fuels derived from other sources meeting these specifications would be fit-for-purpose. Nonetheless, these specifications serve as guidelines for other potential sources.

Standards for jet fuel are more stringent, with no oxygenates being allowed.²² However, routes to jet fuel through biomass are possible *via* gasification technologies. Presently, synthetic paraffinic kerosene (SPK) can be introduced at blend volumes of up to 50% after production by Fischer-Tropsch technology, alongside the necessary hydrotreating, hydrocracking, and hydroisomerization required to meet the specified fuel properties. Additionally, the fifteen carbon-containing hydrocarbon farnesane (Figure 1.5) can be added at up to 10 vol% as a synthetic iso-paraffin (SIP).

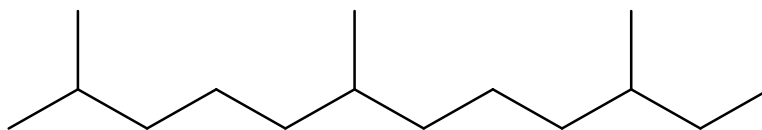


Figure 1.5 Structure of synthetic iso-paraffin farnesane.

1.1.6 Requirements for Converting Biomass Intermediates to Fuels

Pyrolysis oils contain oxygen in a number of functionalities: water, alcohols, acids, aldehydes, ketones, esters, and aromatics. Partially deoxygenated pyrolysis oils must therefore be shown to contain less than 2.7 wt% oxygen present as only alcohols and aliphatic ethers to meet D4814.

1.1.7 Comparing Conversion Product Properties to Fuel Specifications

Environmental regulations require that oxygenates be removed either selectively to leave only ethers and C₂₊ alcohols for standard gasoline or completely for reformulated gasoline (RFG). Lignocellulosics have been shown to deoxygenate thermochemically over ZSM-5 and Ga-doped ZSM-5 to form a pool of olefins (14-28% selectivity) and aromatics typically described as benzene, toluene, and xylene (BTX), with benzene being the major aromatic (17-45% selectivity).²³ This product pool would not meet RFG regulations by itself. Alternatively, liquid phase aldol condensations between furfurals and acetone or propanal over MgO-ZrO₂ have been shown to produce C₁₂ and C₁₅ condensates with excellent selectivity (>90%).²⁴ These products exhibit several sites of unsaturation and oxygen content in the range of 20 wt%. It is therefore possible to envision hydrodeoxygenation from these intermediates to gasoline range molecules. These two catalytic pathways emphasize the need for judicious consideration of today's fuel specifications to effectively design catalysts for tomorrow's renewable fuel production.

1.1.8 Promising Strategies for Pyrolysis Oil Upgrading

The two main strategies for deoxygenating whole pyrolysis oil are hydrodeoxygenation (HDO) and zeolite cracking. Within these broad categories several deoxygenation mechanisms can take place, including decarboxylation/decarbonylation, hydrogenolysis, hydrodeoxygenation,

cracking, and hydrogenation. A more detailed description of these mechanisms can be found elsewhere.²⁵ The goal of these processes is not always to completely remove all of the oxygen content. Certain oxygenates can improve fuel performance. In the United States gasoline must contain at least 2 wt% oxygen, accomplished by ethanol blending.²⁵ Although diesel and jet fuels are not currently blended with oxygenates, studies have indicated that this could decrease soot formation. For example, dimethyl ether has been investigated for use in diesel engines.²⁶

Current engines have evolved with the petroleum industry to run most effectively on the regulated hydrocarbon blends that have become standard, so it is no surprise that highly oxygenated fuels cannot be directly used. Oxygen content itself is not necessarily indicative of a low-quality fuel; this depends on the functional group it is contained in. Effort should be directed towards developing both biomass derived fuels as well as engines that can efficiently use them. This has already started to occur in Brazil, where biomass derived alcohol fuels are produced in large volumes.²⁷ Modifications were made to existing internal combustion engines by redesigning components to better handle oxygenated fuels. For example, the carburetor was altered to change the ratio of air to fuel, a new intake manifold was designed to provide the necessary heating to compensate for alcohols evaporating less easily than gasoline, and the compression ratio was increased to utilize the high octane rating of alcohol fuels.²⁷ If the goal is to produce a new fuel from pyrolysis oil rather than to convert it into the exact hydrocarbon mixture found in petroleum derived fuels, the upgrading process will be much less complicated and expensive.

1.1.9 Other Upgrading Considerations

The removal of all oxygen functionalities from pyrolysis oil to make a purely hydrocarbon fuel that mimics petroleum-derived compounds would ensure compliance with the

existing fuel specifications regarding oxygen content, but not necessarily ensure compliance with other properties such as aromatic content, distillation points, octane rating, etc. Also, it requires that most of the compounds in the oil be upgraded. Technologies exist to perform many of these conversions, such as those described above, but this still requires many different reactions be performed before the pyrolysis oil can be used as a fuel. Even with reactions tuned to efficiently produce a target compound from a pyrolysis intermediate, separating these oxygenates and using different reactors, catalysts, and process conditions would likely require a complicated plant design with high capital costs. It would be advantageous to be able to use some of the oxygenate products, either directly or after minimal upgrading.

Getting new oxygenated compounds approved for use in fuels will require research be directed towards studying how they behave in engines, which will take a substantial amount of time. Over time petroleum fuels and engines have coevolved to effectively work together.²⁸ For example, adding oxygenates to diesel fuel reduces the amount of soot production, with the type of oxygenate influencing the extent of this reduction.²⁹ Though it will not be quick or simple to understand what types of functionalities could be benign or even beneficial in a liquid fuel, this may be worth exploring in order to make fuel production from biomass pyrolysis a viable option.

1.2 The Oligomerization of Light Olefins by Heterogeneous Catalysts

Prior research efforts by the Bioenergy Technology Office (BETO) have demonstrated a pathway to mixed alcohols by biomass gasification to syngas and subsequent conversion to alcohols over a K-CoMoS_x type catalyst.³⁰ The production of these mixed alcohols (C₂-C₄) was estimated to become economical at a minimum price of \$3.11 per gallon of gasoline equivalent.³¹ However, diesel and jet remain as applications where longer chain hydrocarbons (C₁₀-C₂₀) are required, and where long-term strategies that rely on alternatives to liquid fuels (e.g.

electrification) are less feasible. For diesel fuel, the oxygenated quality of biomass derivatives may present advantages in terms of reducing particulate matter production.³² However, the aromatic structure of compounds found in biomass makes them poor diesel substituents on the basis of their low cetane value.¹² Additionally, the polar nature of oxygenates makes them prone to phase separation issues in the nonpolar diesel fuel unless long alkyl chains are adjoined to the oxygenated aromatic. In short, the hydrocarbon backbone should be primarily linear for the preservation of cetane value, as in conventional biodiesel.

More recently, efforts have focused on converting these mixed alcohols to light olefins, namely ethylene and propylene, by catalytic dehydration over a commercial SAPO-34 solid acid catalyst.³³ The present project aims to study the oligomerization of said olefins as a means to produce compounds in the gasoline and distillate range using a commercial catalyst, with jet and diesel being the most desirable products. Additionally, oligomerization may be applied to light olefins obtained from the methanol-to-olefins process (MTO).³⁴

The oligomerization of light olefins is a potential pathway to aromatic-free, liquid transportation fuels *via* the biomass gasification platform. Recent work at NREL has shown that a mixture of alcohols produced from syngas over a K-CoMoS_x type catalyst^{30, 35} can be dehydrated with high yield over a SAPO-34 solid acid catalyst to form an ethylene-rich mixture of primarily ethylene and propylene.³⁶ The focus of the current work is to investigate the characteristics of heterogeneous catalysts capable of oligomerization of these light olefins to C₅-C₂₂ products. Nickel supported on solid-acid catalysts, such as zeolites, mesoporous silica-alumina, and silica-alumina, has become the most promising and well-studied class of materials for this purpose.³⁷⁻³⁹ MOF-type structures have also been utilized to couple ethylene with very high selectivity towards 1-butene.⁴⁰

1.2.1 Mechanisms for the Oligomerization of Ethylene and Higher Olefins

Figure 1.6 is a schematic for the dimerization and isomerization of ethylene over a nickel complex (from de Souza et al.).⁴¹ The key steps in this mechanism are ethylene coordination, insertion, isomerization, and elimination.

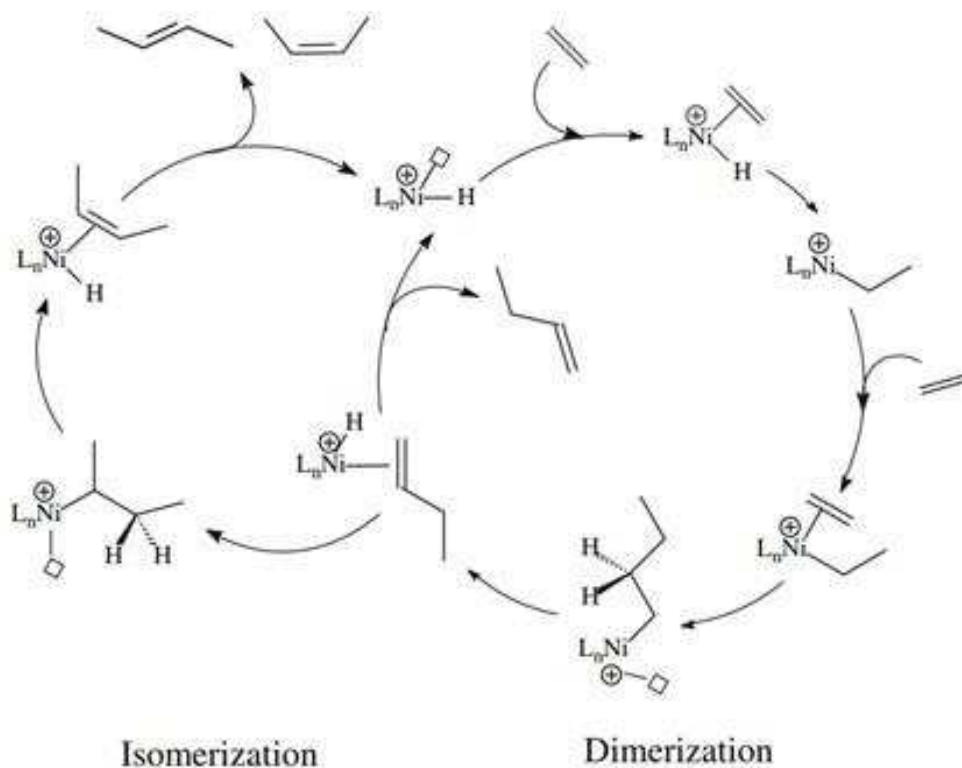


Figure 1.6 Schematic catalytic cycle of ethylene dimerization and 1-butene isomerization. Reproduced from de Souza et al.⁴¹

Nickel acts catalytically through an interaction with ethylene's π -electrons. The electron density of nickel is a key factor for the relative rates of these steps. Subsequently, the choice of catalyst is expected to modify the electron binding energy of nickel, possibly giving insights into the balance of electron density required for a highly active, yet highly selective catalyst.

Additionally, Brønsted acid sites are responsible for oligomerization of higher olefins, namely

propylene and above (Figure 1.7). The bifunctional nature of these catalysts has been described by Lallemand et al, whereby Ni^+ cations are responsible for the formation of butene from ethylene coupling, and further coupling is accomplished by Brønsted sites to yield higher carbon number products.⁴²

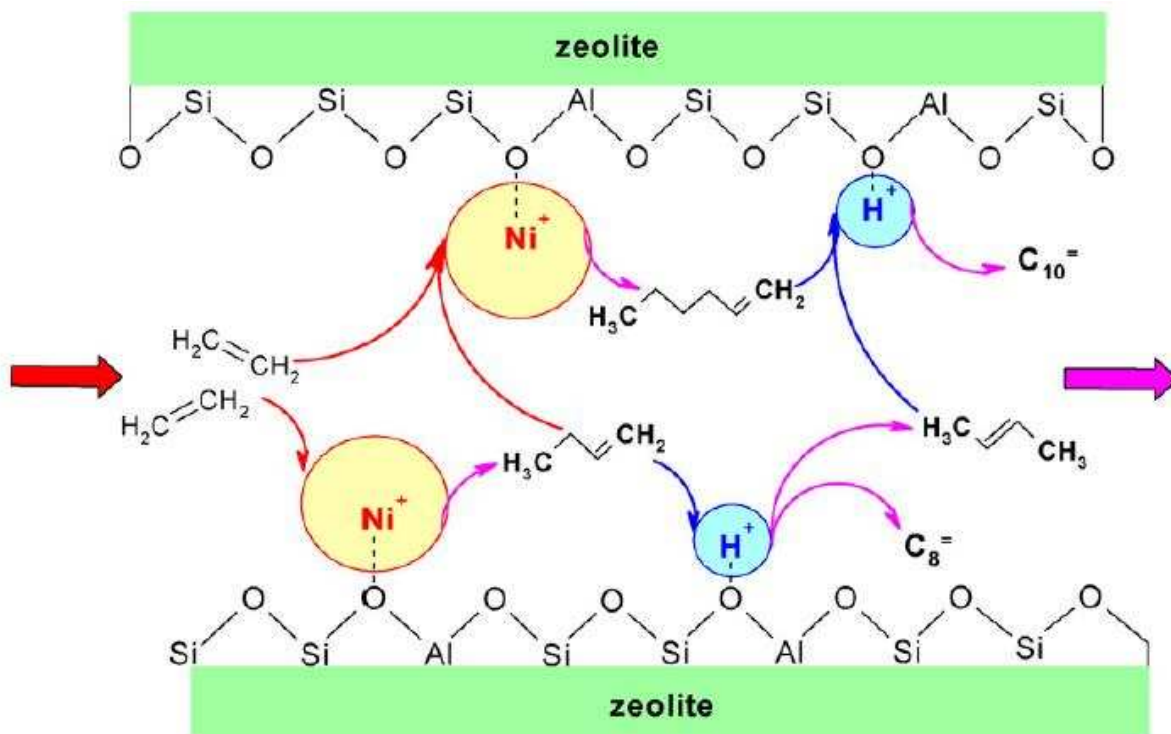


Figure 1.7 Main reaction pathways for the oligomerization of ethylene and higher oligomers over Ni-exchanged molecular sieves. Reproduced from Lallemand et al.⁴²

Based on seed experiments, the co-oligomerization of light olefins was observed to proceed first through coupling of ethylene and propylene, with no butene being formed. There are several possible mechanisms to explain this observation. First, activation of ethylene and propylene may occur over separate active sites (Figure 1.8). In the separate site mechanism, ethylene is activated over Ni cations, and propylene is activated over Brønsted acid sites. Further reaction between the activated species requires close proximity between the active sites.

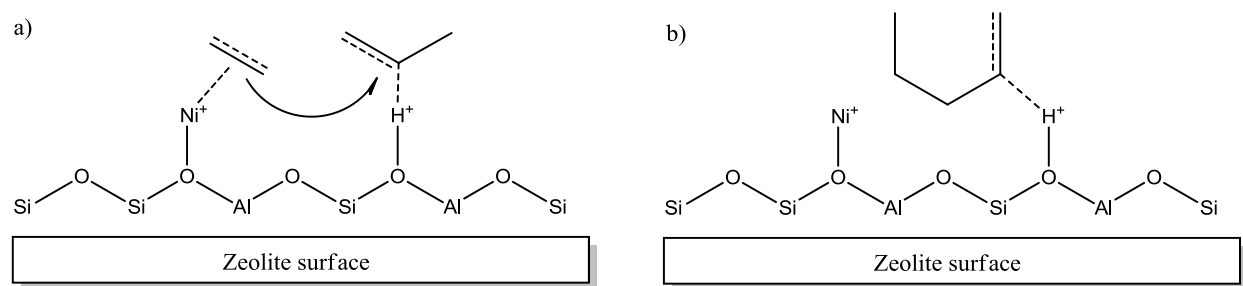


Figure 1.8 Proposed mechanism for co-oligomerization separate site mechanism.

Co-oligomerization may also proceed by activation of both species over a single site, being either the Ni cation (Figure 1.9) or Brønsted acid site (Figure 1.10). For nickel, it is expected that ethylene is the first species activated. Coordination and subsequent insertion with propylene leads to the pentene product. Over Brønsted acid sites, propylene and higher oligomers are most likely the first intermediates formed, where pentene is formed by insertion of ethylene.

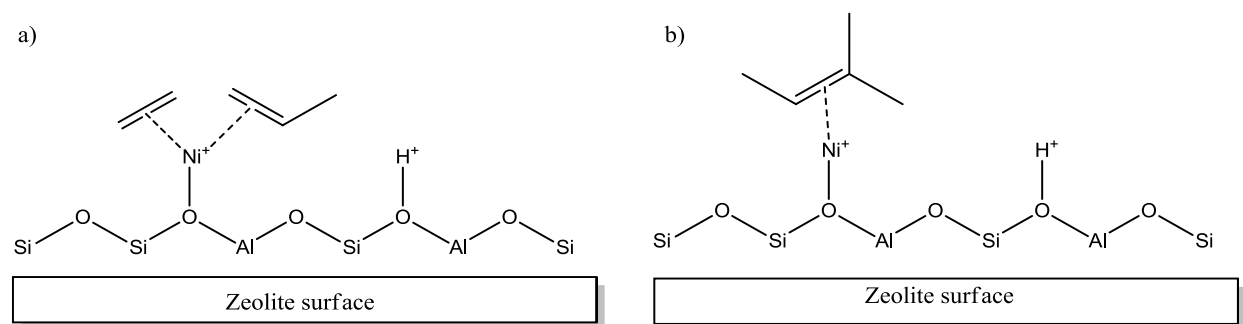


Figure 1.9 Proposed mechanism for co-oligomerization over only Ni cation sites.

The bifunctional nature of these catalysts enables them to contribute to the oligomerization pathway by two separate mechanisms. In the coupling of propylene and higher olefins, Brønsted acid sites produce sufficiently active surface intermediates by protonation of the secondary carbon to react and form dimeric and heavier products in a mechanism termed

hetero-oligomerization.³⁷ Conversely, the activation of ethylene requires the use of a metallic catalyst, most commonly nickel, to produce coupling products *via* a migratory insertion pathway, termed *homo-oligomerization*.⁴³ Although numerous works have correlated the activity of nickel sites with the Brønsted acidity of the support,^{38, 44-45} it has been recently proposed that weaker acid sites, such as silanols, aluminols, and Lewis acids, may in fact be responsible for the formation of the most active nickel species.⁴⁶⁻⁴⁸

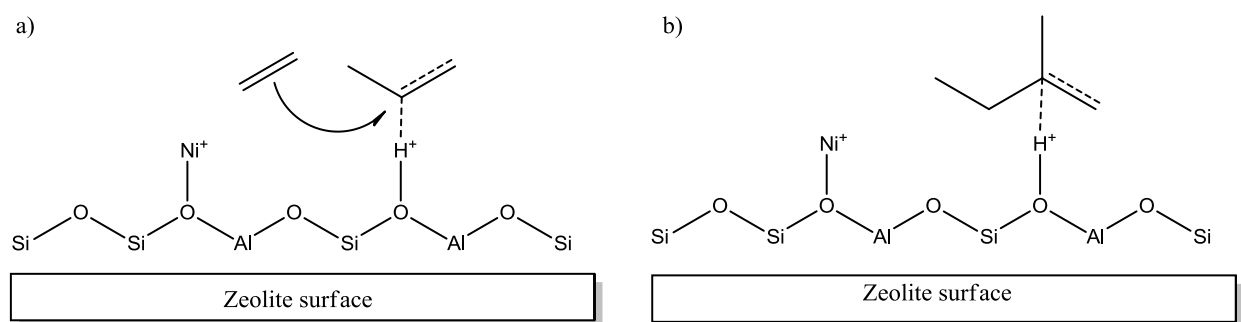


Figure 1.10 Proposed mechanism for co-oligomerization over only Brønsted acid sites.

Proton transfers from the complexed reactant to an adjacent oxygen in the support have been proposed as important steps in aldol reactions catalyzed by Lewis acidic zeolites⁴⁹ and ethylene polymerization by silica-grafted Cr(III).⁵⁰ The role of this step in ethylene oligomerization on heterogeneous nickel catalysts has also been suspected, although not in the catalytic cycle itself but in the formation of the active nickel species with consequent production of 1,3 butadiene.⁴³ The stability of the coordinated ethylene has been correlated with the interaction between nickel and a hydrogen atom on the ethylene, termed an agostic bond.⁵¹ A reaction pathway for ethylene oligomerization that is stabilized by the agostic bond has been calculated by Brogaard et al., as shown in Figure 1.11.⁴³

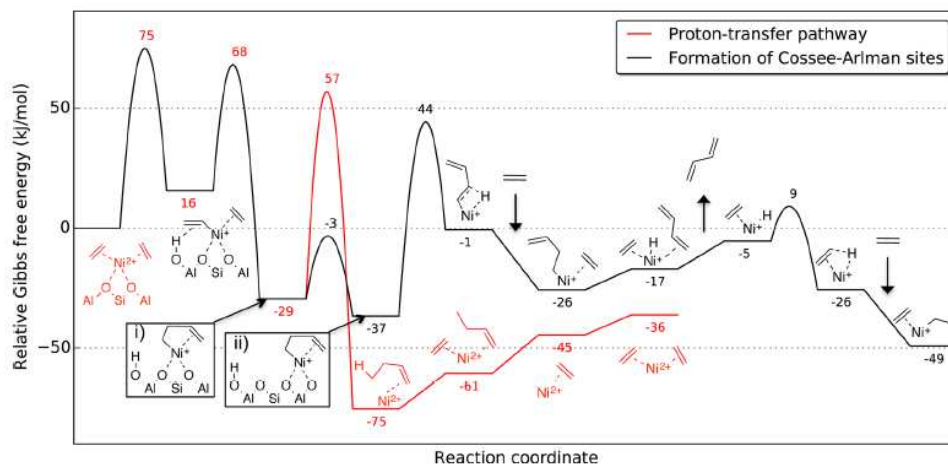


Figure 1.11 The oligomerization of ethylene by cationic nickel when stabilized by an agostic interaction with a β -hydrogen of the growing carbon chain. Reproduced from Brogaard et al.⁴³

1.2.2 On the Nature of Active Sites for Olefin Oligomerization

Increasing calcination temperature on ferrierite zeolites was found to correlate with an enhanced selectivity for 1-butene conversion to C3-C5 olefins at 620 K.⁵² This effect was attributed to the increased number of Lewis acid sites that formed upon the dehydroxylation of Brønsted sites during calcination, which took part in oligomerization of butenes followed by cracking/hydrogen transfer reactions. Brønsted acidity was correlated with isobutene production by isomerization of the carbon double bond.

Cai performed acid and metal site poisoning studies on the oligomerization of ethylene, propylene, and butylene over NiSO₄-based catalysts.⁵³ The conversion of propylene was found to be less sensitive to acid site neutralization with NaOH than either ethylene or butene.

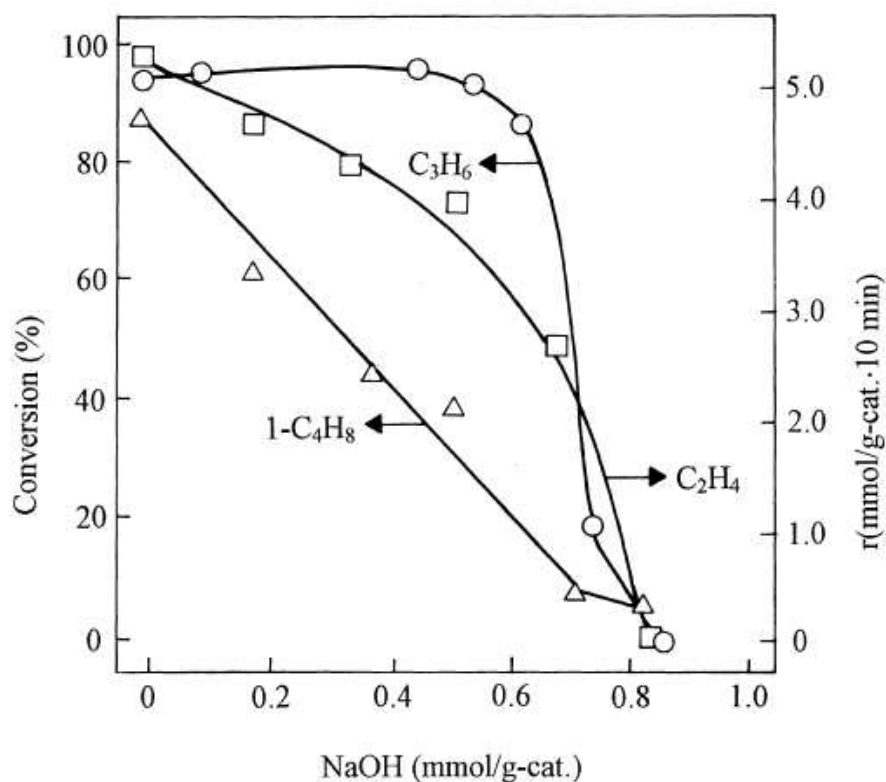


Figure 1.12 The effect of site poisoning a $\text{NiSO}_4/\text{Al}_2\text{O}_3$ catalyst with NaOH on the conversion of ethylene, propylene, and butene. Reproduced from Cai.⁵³

Metal site poisoning by exposure of the catalyst to CO caused a drastic reduction in ethylene conversion, and furthermore reduced propylene conversion, but had little effect on butene conversion. These results suggested that ethylene was converted exclusively by nickel sites, propylene by a mixture of nickel and acid sites, and butene by acid sites.

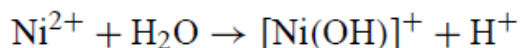
Penkova et al. studied the state of nickel ions supported on Al-BEA zeolite and dealuminated BEA zeolite.⁵⁴ Ion exchange of the Al-containing BEA zeolite was found to impart nickel with less reducibility than Ni on the dealuminated zeolite. DRIFTS experiments with adsorption of CO and NO lead the authors to conclude that nickel on the dealuminated zeolite was coordinatively saturated or inaccessible due to its incorporation in hydroxyl nests and defect sites created by the removal of aluminum. Treatment with CO at 623 K for 1 h converted some

of the Ni^{2+} species to Ni^+ by reduction. The authors noted that some inaccessibility may be due to zeolitic O-rings being large enough for the small Ni cations (0.69 Angstrom radius) to slip inside. Hadjiivanov reported the formation of Ni^+ species upon interaction with CO at room temperature.⁵⁵

Bentaleb et al. observed the reducibility of nickel dispersed on an alumina support to be diminished by the use of viscous media during ion exchange and calcination.⁵⁶ The authors attributed the viscosity of the media to an improvement in the dispersion of nickel by hindering the transport effects that occur during solvent evaporation. The least reducible material was prepared with nickel nitrate hexahydrate in the presence of citric acid, which potentially increased chemical interactions of nickel with aluminum due to the low pH formed during impregnation. These results are at odds with an earlier paper by the same author, in which impregnation of nickel in the presence of citric acid was found to improve reducibility with the explanation that nickel was chelated by citric acid and thus could not interact strongly with the support.⁵⁷

During nickel deposition, aluminum may leach from the support and combine in solution with the forming nickel hydroxide phase to result in nickel aluminates upon calcination.⁵⁸

An increase in nickel content of NaMOR by ion exchange with nickel nitrate was shown to result in an increase of acid site concentration.⁵⁹ This increase was accompanied by a growth of the 3602 cm^{-1} peak in FT-IR that corresponds to bridging hydroxyl groups (Al-OH-Si), and a shift towards 3619 cm^{-1} . Ammonia TPD performed at dosing temperatures of $120\text{ }^\circ\text{C}$ revealed a trend of 1.9 acid sites introduced per nickel, while dosing at $150\text{ }^\circ\text{C}$ measured only 1.2 acid sites created per nickel. These results suggested that nickel incorporation resulted in the formation of a weak Lewis site from the metal and an additional Brønsted site *via* the following reaction:



This thermal reduction has been shown to occur on Cu(II) cations under inert thermal treatment.⁶⁰

Ethylene and Cl^- exhibit a strong *trans* influence and interfere with each other's bonding if positioned *trans* to each other.⁶¹

Nickel (II) hydroxide dehydration to form NiO occurs primarily in the temperature range of 250-340 °C.⁶² Meanwhile, the activation of alumina occurs primarily in the range of 500-800 °C.⁶³

1.2.3 The Co-monomer Effect

The effect of co-feeding ethylene and propylene to oligomerization catalysts is not well studied. However, a so-called “co-monomer effect“ is known in polymerization, in which higher olefins are thought to contribute greater electron density to the metal active site, and subsequently modify catalytic active, supposedly by the increased basicity of longer α -olefins.⁶⁴ Per Conant, the lessened degree of unsaturation “felt” by alkenes only increases slightly after having greater substitution than ethylene.⁶⁵ This effect has been termed hyperconjugation. Propylene, in general, had the greatest comonomer effect. This can perhaps be viewed as a tradeoff between basicity at the α -unsaturation, which does not increase substantially beyond propylene, and steric effects, which clearly depend on the degree of substitution. It is thus hypothesized that the activity of nickel oligomerization catalysts may be different for mixed olefins versus a feed of pure ethylene.

Literature acknowledges that propylene and higher oligomers can be oligomerized over Brønsted acid sites, while ethylene requires the use of metal catalysts, either in homogeneous or heterogeneous form.⁶⁶ Deimund et al. have explored the use of Ni-stannosilicates for propylene

oligomerization.⁶⁷ These materials possessed no aluminum and had weaker acid strengths than aluminosilicates, yet were active for propylene oligomerization. Gan et al. studied copolymerization of ethylene and propylene using a heterogeneous Cr(III) acetate catalyst that was activated by AlEt₂Cl to form a Cr(II) active species.⁶⁸ They observed an interesting effect that the catalyst could not be activated in the presence of propylene. If the catalyst was allowed to react with the cocatalyst beforehand, the polymerization of propylene would proceed. In contrast, this catalyst was able to activate under the presence of ethylene. These results suggest that propylene may bind too strongly to a cationic metal to allow interaction with the cocatalyst. Tanaka et al. explored the support of nickel cations on silica MCM-41.⁶⁹ They found that catalytic activity was inversely related to pore size in the mesoporous silica, and was increased with nickel loading. The authors attributed the catalytic active sites to be three-coordinated Ni²⁺ cations (Figure 1.) based on correlations between catalytic activity and peak intensity from FT-IR experiments where NO was pulsed onto the sample.

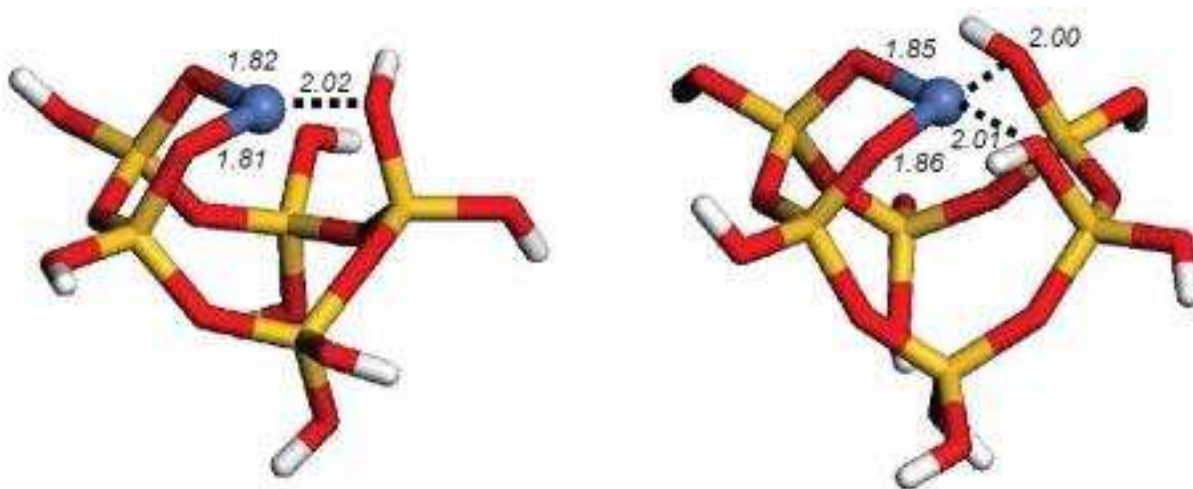


Figure 1.13 Models of three-coordinated (left) and four-coordinated (right) Ni cations in silica MCM-41. The nickel, silicon, oxygen, and hydrogen atoms are depicted in blue, yellow, red, and white, respectively. Reproduced from Tanaka et al.⁶⁹

1.3 Goals and Structure of Thesis

The work described in this thesis focuses on a conversion pathway from bio-derived alcohols to the light olefins ethylene and propylene, followed by oligomerization to oxygen-free hydrocarbon fuels. There were four sets of objectives for the work described in this thesis:

1. Demonstrate the oligomerization of light olefins over a heterogeneous catalyst
2. Select a suitable catalyst system for study based on catalyst performance and price
3. Identify the dominant interactions between the active phase and catalyst support
4. Characterize the nature of oligomerization active sites and other heterogeneous catalysts through appropriate techniques, such as chemisorption.

1.4 Expected Impact

The demonstration of a pathway from biomass to liquid fuels through oligomerization of light olefin intermediates will increase opportunities for the utilization of alternative carbon sources such as biomass and natural gas in the transportation fuels market. An increased fundamental understanding of the active site and relevant support interactions can be used to inform synthetic methods that result in cheaper and more active catalysts. The advancement of appropriate characterization techniques to suitably characterize these active sites will promote further research into these materials.

CHAPTER 2

INTERPRETING NICKEL ACTIVE SITES IN HETEROGENEOUS OLIGOMERIZATION CATALYSTS

2.1 Introduction

The oligomerization of light olefins, namely ethylene and propylene, to oligomers having at least 4 carbons is well known,⁷⁰ and is envisioned for use in the selective conversion of domestic petro-carbon alternatives, such as biomass and natural gas, to produce liquid fuels and chemicals. Although propylene and higher olefins oligomerize readily over Brønsted acid sites, the oligomerization of ethylene requires a metal functionality to proceed efficiently.³⁷ Nickel catalysts excel at this reaction, and have been studied extensively since the discovery of the so-called “nickel effect” by Karl Zielger and co-workers in the 1950s brought them to the world’s attention.^{37, 70-71}

While generally less active and selective than the homogeneous nickel catalysts pioneered by Ziegler, heterogeneous nickel catalysts are more desired for industrial application, especially for those targeting fuels and not specialty chemicals, owing to their lower cost, greater robustness, and relative ease of product separation.

Research into heterogeneous nickel catalysts has discovered many notable features of these catalysts that have warranted attention over the years. In sharp contrast to homogeneous nickel complex analogues, which require the addition of highly reactive co-catalysts, such as trialkyl aluminum, before becoming active for oligomerization,³⁹ the activation of these materials is facile, being often achieved by simple thermal treatment.⁷² Although an intriguingly diverse combination of supports and nickel precursors have been shown to form active materials,³⁸ there appears a direct relationship between nickel activity and support Brønsted acidity.⁵³

The apparent flexibility of nickel oxidation state, both in the formation of active materials being produced from Ni⁰, Ni^I, and Ni^{II} precursors,⁷³ and the simultaneous observation of both Ni^I and Ni^{II} in active, working catalysts⁷⁴ has led to significant discussions regarding the activity of each nickel valence, with many authors ascribing the active species to be the low valent Ni^I species.³⁸ The mobility of nickel ions has been implicated as the cause of an induction period in zeolites, where migration of the divalent nickel cation from 5-membered rings to the zeolite supercage is caused by olefin feed acting as a ligand.⁷⁵ Some experiments have suggested that vacuum treatment alleviates the catalytic induction period observed after oxidative pretreatment, although the mechanism remains unclear.⁷⁶

Authors have argued heavily to the benefit of mesoporous textural properties⁷⁷ for slowing catalyst deactivation caused by the accrual of oligomeric products. More recently, the moderate nature of acid sites⁴⁸ on such mesoporous and amorphous silica-aluminas has been implicated in the greater activity of these materials relative to zeolites. It is consequently of interest to study the nature of the nickel-support interaction, both upon pretreatment under various conditions, and after exposure to olefin feed, to identify the composition of the active nickel site in ASAs.

Heterogeneities in the support surface have so far hampered efforts to fully describe how the support environment results in the above unique behaviors. In this chapter, model nickel compounds and two active heterogeneous nickel catalysts, Ni/ASA and Ni/Al-MCM-41, are characterized by X-ray absorption spectroscopy (XAS), temperature-programmed reduction, diffuse-reflectance infrared Fourier-transform spectroscopy (DRIFTS) in the presence of carbon monoxide (CO) and pyridine (Py), thermogravimetric analysis (TGA), temperature-programmed reduction (TPR), nitrogen physisorption, ammonia temperature-programmed desorption (NH₃-

TPD) and ^{27}Al magic angle spinning nuclear magnetic resonance (^{27}Al MAS NMR), and a resulting picture of the active metal center coordinative environment described. The material properties of Ni/SiO₂ and Ni/Al₂O₃, known to be inactive in the literature,⁷⁸ are also examined for comparison.

2.2 Experimental

The following subsections detail the experimental methodology of this chapter.

2.2.1 *In situ* X-ray Absorption Spectroscopy

XAS studies were conducted at the Advanced Photon Source (APS) at Argonne National Laboratory in Lemont, Illinois, on the beamline 10-BM, which is operated by the Materials Research Collaborative Access Team (MRCAT). All catalysts provided were studied *in situ* using a continuous-flow reactor, which consisted of a quartz tube (1-in. OD, 10-in. length) sealed at each end with Kapton windows using Ultra-Torr fittings. Ball valves were welded to each Ultra-Torr fitting and served as the gas inlet and outlet. An Omega K-type thermocouple was placed against the catalyst sample holder to monitor temperature. Catalyst samples were pressed into a cylindrical sample holder consisting of six wells, forming a self-supporting wafer. The amount of catalyst used was determined by calculating the weight of catalyst needed to give an absorbance (μx) of approximately 1.0 where possible. After loading, samples were treated in flowing He at 200 °C for 3 h then cooled and measured at room temperature.

In some experiments, samples were exposed to flowing ethylene (3%, balance He) for 2 h following pretreatment, and then measured at 120 °C in flowing He. The temperature-dependent Debye-Waller factors were obtained at room temperature and 120 °C for each experiment type, respectively. Spectra were collected in transmission mode using ionization chamber detectors that were optimized for collecting maximum current while maintaining a linear response range

(ca. 10^{10} photons detected s^{-1}). A third detector in series with the two ionization chambers was used to collect a foil reference spectrum simultaneously with each measurement for energy calibration purposes.

The normalized, energy-calibrated X-ray absorption near-edge structure (XANES) spectra were obtained using standard methods with energy steps of 0.5 eV. The edge energy was determined from the maximum of the first peak by taking the first derivative of the XANES spectrum while the energy of pre-edge features was determined by the maximum in the peak intensity. High-resolution measurements of the pre-edge region at 8326-8334 eV were recorded at energy steps of 0.05 eV. Experimental phase shift and backscattering amplitudes were measured using standards consisting of compounds of known structure which are shown in the relevant tables detailing the results of the fits. Standard data reduction techniques were employed to fit the data using the WINXAS 3.1 software program. The extended X-ray absorption fine structure (EXAFS) parameters were obtained by a least square fit in k or R -space (detailed in the table of fits) of the k^2 -weighted Fourier Transform (FT) data.

2.2.2 Model Compound Synthesis

$NiCr_2O_4$ was synthesized according to Suchomel et al.⁷⁹, whereby stoichiometric precursors of $Ni(NO_3)_2 \cdot 6H_2O$ and $Cr(NO_3)_3 \cdot 9H_2O$ were dissolved in deionized water and then heated until dry. The precipitate was ground in a mortar and pestle and calcined at 1000 °C, 10 °C/min, for 24 h to produce a bluish-green powder.

$KNiPO_4 \cdot 6H_2O$ was prepared according to Trobajo et al.,⁸⁰ in which a freshly-prepared aqueous solution of $NiCl_2$ (17 mL, 1 M) was combined with 60 g of K_2HPO_4 , diluted to 70 mL, and stirred at room temperature until the solids were well dispersed. After 24 h, the resulting solids were filtered and dried overnight at 120 °C under vacuum. The supernatant was

centrifuged at 9,000 RPM for 15 min, was with DI water, and centrifuged again. The liquid phase was decanted, and the obtained slurry also dried overnight at 120 °C under vacuum. The apple green- to olive-colored crystals were then calcined in air at 550 °C, 3 °C/min for 5 h to produce the red ochre-colored KNiPO₄ samples.

2.2.3 Nickel Catalyst Synthesis

Nickel on amorphous silica-alumina (ASA) (Davicat 3125, Grace Davidson) was prepared by ion exchange for 4 h under reflux with aqueous Ni(NO₃)₂ (>97%, Alfa-Aesar, 0.2 M, 6 mL per g_{support}). The catalyst was then filtered, washed with DI water, dried under vacuum at 120 °C overnight, and calcined at 550 °C for 5 h at 5 °C/min. This sample is denoted as Ni/D25. A sample of Ni/ASA was then further exchanged and filtered three times with fresh 0.1 M NaNO₃ (100 mL per g_{support}), and then filtered, washed, dried, and calcined as above to obtain the sample denoted as Ni+Na/ASA. Nickel on silica (Sipernat 22, Evonik), alumina (Alu 130, Evonik), and Al-MCM-41 (SAR = 39, Sigma-Aldrich) were prepared by the incipient wetness method, then dried and calcined as above to obtain the samples denoted as Ni/SiO₂, Ni/Al₂O₃, and Ni/Al-MCM-41, respectively.

2.2.4 Thermogravimetric Analysis

The effect of heating the hydrated KNiPO₄ sample was measured with a G500 from TA Instruments. Samples were heated in a platinum boat at a ramp rate of 20 °C/min to a final temperature of 1000 °C. Separate experiments were performed under flowing nitrogen and flowing zero air.

2.2.5 N₂ Physisorption

The textural properties of the catalysts were determined by N₂ physisorption at -196 °C using a Micromeritics ASAP 2020 instrument. Prior to analysis, samples were outgassed at

350 °C for 6 hours under vacuum. Surface areas were determined by Brunauer-Emmett-Teller (BET) analysis over the P/P_0 range of 0.05-0.30. The total pore volume was derived from the amount of N_2 adsorbed at $P/P_0 = 0.99$. The distribution of pore sizes was calculated using the Barrett-Joyner-Halenda (BJH) method on the desorption branch of the isotherm.

2.2.6 NH_3 -TPD and TPR

The density and strength distribution of acidic sites on the Ni-containing catalysts were characterized by the temperature-programmed desorption of ammonia (NH_3 TPD). Samples were pretreated, dosed, and analyzed under flowing conditions (50 mL/min, ambient pressure) in a Micromeritics Autochem II 2920 chemisorption instrument. After being dried at 100 °C for 1 h and pretreated at 500 °C for 2 h, the samples were exposed to a blend of 10% NH_3/He for 1 h at a temperature of 120 °C. The samples were purged with He for 1.5 h, then ramped to 500 °C at 30 °C/min and held for 1 h. In TPR experiments, samples were purged at 120 °C for 1 h in flowing Ar, and then ramped from 40 °C to 900 °C at 10 °C/min in 10% H_2/Ar . Changes in outlet concentrations were monitored by a downstream thermal conductivity detector (TCD).

2.2.7 X-ray Diffraction

The crystalline properties of the catalysts were determined by powder x-ray diffraction using a Rigaku Ultima IV diffractometer equipped with a $Cu K_\alpha$ source operated at 40 kV and 44 mA. Diffractograms were collected using a D/teX Ultra high-speed detector in the 2θ range of 20-80 ° 2θ at a scan rate of 5 ° 2θ /min. Samples were prepared by supporting the powdered catalyst onto a glass slide having a 0.5 mm recession and pressing with a glass slide to create a flat surface. Diffraction patterns were compared to the reference card file for NiO (ICDD 04-002-0665) from the International Center for Diffraction Data.

2.2.8 Solid-state ^{27}Al MAS NMR

Solid state magic angle spinning nuclear magnetic resonance (MAS NMR) was performed using a Bruker Avance III spectrometer equipped with a 14.1T magnet (^{27}Al operating frequency of 156.38MHz.), a 2.5mm MAS probe, and Topspin 3.0 for data acquisition and processing. The powdered samples were packed directly into 2.5mm zirconia rotors with Valspar caps. Samples were collected at room temperature, with MAS=25kHz, and using a one pulse experiment with a 30° tip angle (0.5 sec). Spectra were acquired with a delay time of 0.5sec and 50k scans. Prior to analysis, the powdered samples were dried overnight at 200°C in air.

2.2.9 Pyridine and CO DRIFTS

The relative amounts of Brønsted and Lewis acid sites were determined using pyridine adsorption diffuse-reflectance FT-IR spectroscopy (py DRIFTS). Spectra were recorded at a resolution of 4 cm^{-1} on a Thermo Nicolet iS50 FT-IR spectrometer equipped with a Harrick Praying Mantis high temperature reaction chamber and CaF windows. Samples were loaded into the chamber and pretreated in flowing N_2 (100 mL/min) at 200°C for 3 h. After cooling to 150°C , samples were purged with N_2 for 0.5 h, and pyridine vapor was introduced. After 5 min of pyridine exposure, the samples were heated to 200°C and held for 1 h under flowing N_2 to remove excess and/or physisorbed pyridine. The adsorption bands near 1454 cm^{-1} (Lewis) and 1545 cm^{-1} (Brønsted)⁸¹ and their relative adsorption coefficients ($\epsilon_B/\epsilon_L = 0.76$)⁸² were used to determine the relative Brønsted/Lewis acidic site ratios.

The speciation of cationic nickel was determined by low temperature DRIFTS experiments in the presence of carbon monoxide (CO DRIFTS). The samples were pretreated in a Harrick Praying Mantis low temperature reaction chamber at 200°C under flowing N_2 for 3 h,

and then cooled to approximately $-100\text{ }^{\circ}\text{C}$ by admittance of liquid nitrogen to the sample chamber cold finger, and the chamber evacuated to ~ 4 torr. The samples were then exposed to pulses of 1% CO in N_2 (General Air), and the resulting changes in infrared spectrum absorbance recorded. In other experiments, the samples were reduced at $500\text{ }^{\circ}\text{C}$ with 5% H_2/N_2 for 2 h, then purged with N_2 for 2 h prior to CO dosing at sub-ambient temperature and pressure.

2.2.10 Crystal Structure Models

Model compound crystal structures were modeled using the software VESTA⁸³ with crystal structure information files obtained from the Crystallography Open Database⁸⁴.

2.3 Results

The following subsection contains the results of characterization of the nickel catalysts and model XAS compounds.

2.3.1 TPR

The mass-normalized reduction profiles of the support, ASA, and the nickel and sodium containing forms are shown in Figure 2.. Reduction of the blank support occurred within a broad bimodal event having peaks at temperatures of 650 and $810\text{ }^{\circ}\text{C}$, assigned to reduction of the silica and alumina functionalities, respectively. The reduction of Ni/ASA featured a primary peak at $530\text{ }^{\circ}\text{C}$, and a secondary peak at $650\text{ }^{\circ}\text{C}$. These temperatures are consistent with the reduction of Ni^{II} having a strong interaction with the support and in the range expected for a well-ordered 1:1 phyllosilicate, in which nickel forms a planar, brucitic sheet atop the silica surface.⁸⁵⁻⁸⁶

Reduction temperatures in the range of 600 to $700\text{ }^{\circ}\text{C}$ are also observed for nickel dispersed on porous aluminas,⁸⁷ although reduction onsets as low as $500\text{ }^{\circ}\text{C}$ have been reported for nickel impregnated $\gamma\text{-Al}_2\text{O}_3$.⁸⁸ TPR experiments on a similar system with low loading nickel

(4 wt%) on an ASA containing 28% Al_2O_3 also reported a main reduction event at 530 °C which was assigned to nickel hydrosilicates.⁸⁹⁻⁹⁰ Nickel on mesoporous Al-MCM-41 shows reduction features in the range of 400 to 600 °C, where these materials are known to produce finely dispersed nickel oxide nanoparticles.^{48, 91-92} In this environment, the nickel oxide to silica surface contact is quite intimate, and hence the reducibility approximates those of ordered phyllosilicates. Nickel dispersed on zeolites is typically found to be more reducible than on ASAs or mesoporous supports, with events in the range of 300 to 500 °C resulting from the growth of nickel oxide across the outer surface of the zeolite crystals.⁹³⁻⁹⁴

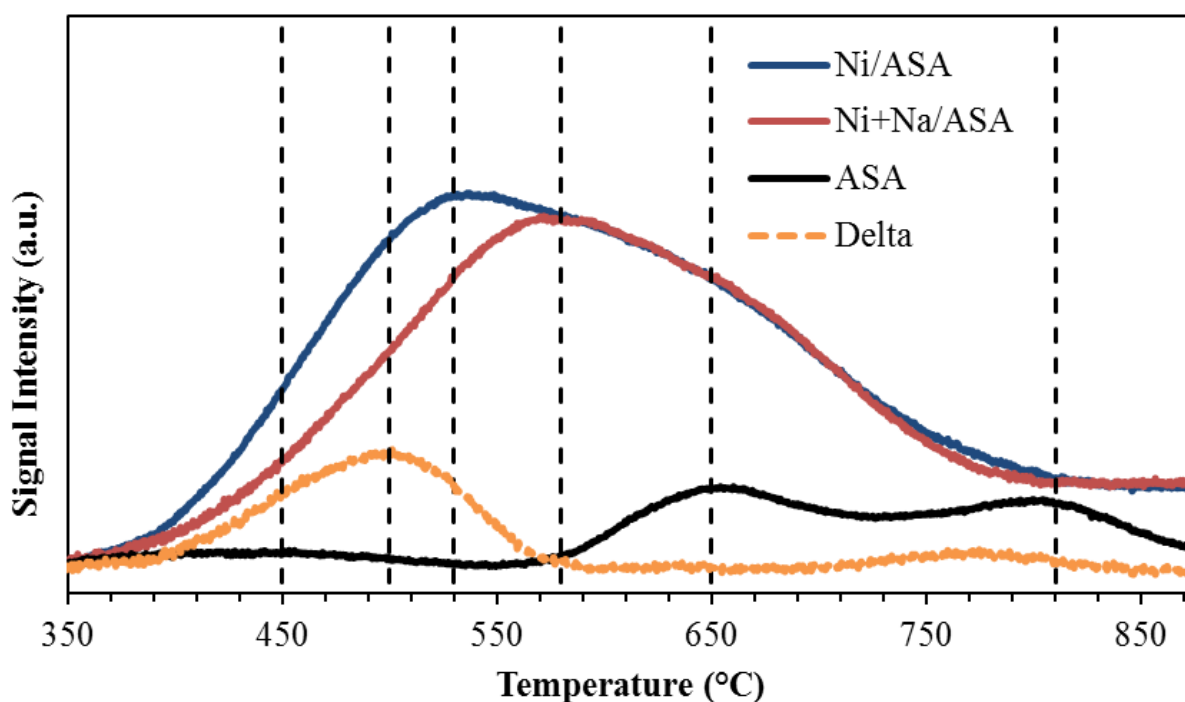


Figure 2.1 Temperature-programmed reduction profiles of the ASA support and Ni catalysts.

Exchange with sodium delayed the onset of the primary reduction event to 580 °C but did not affect the secondary event. This indicated that the nickel species having lower reduction

temperatures were those most susceptible to removal by competitive ion exchange with sodium. The difference profile shows a broad peak with events at 450 and 500 °C. Based on these temperatures, these species appear to be either well-crystallized 1:1 phyllosilicates or poorly-crystalline 2:1 phyllosilicates, or finely dispersed nickel oxide nanoparticles.⁸⁵

2.3.2 Solid State ²⁷Al MAS NMR

The solid state ²⁷Al MAS NMR spectra of ASA before and after incorporation of nickel are shown in Figure 2.2. The parent support showed three broad, overlapping peaks consisting of octahedral aluminum (9 ppm), pentacoordinate aluminum (34 ppm), and tetrahedral aluminum (58 ppm), where the 4- and 6-coordinate Al species predominated. Upon incorporation of nickel, the distribution of observed aluminum reversed. The loss in intensity of the 4- and 6-coordinate species suggests an interaction with nickel that favored conversion to a 5-coordinate geometry. The peaks also less defined and separated, which is indicative of a more heterogeneous and less uniform aluminum environment. The dispersion of 4-coordinate Al species towards 5- and 6-coordination in Al-MCM-41 by incorporation of nickel has been reported.⁹⁵ The authors suggested that the low pH (~4) during nickel exchange was responsible for dissolution of framework Al and redistribution as extra-framework species. A confirmation of the Si/Al ratio of the ASA sample in this work by elemental analysis before and after Ni exchange would address the possibility that Al had been leached from the sample.

Conventionally, tetrahedral and octahedral aluminum are interpreted as the contributors to the Brønsted and Lewis acidity of aluminosilicate materials. Recently, it has been suggested that 5-coordinate aluminum may also contribute Brønsted acidity in ASAs.⁹⁶ Silanols adjacent to coordinatively unsaturated aluminum cations, to which the deprotonated Si-O⁻ can bridge,

have also been implicated in ASA acidity.⁹⁷ Aluminum in zeolites, and especially ASA, has shown to convert between 6- and 4-coordination in the presence of basic adsorbates.⁹⁸⁻⁹⁹

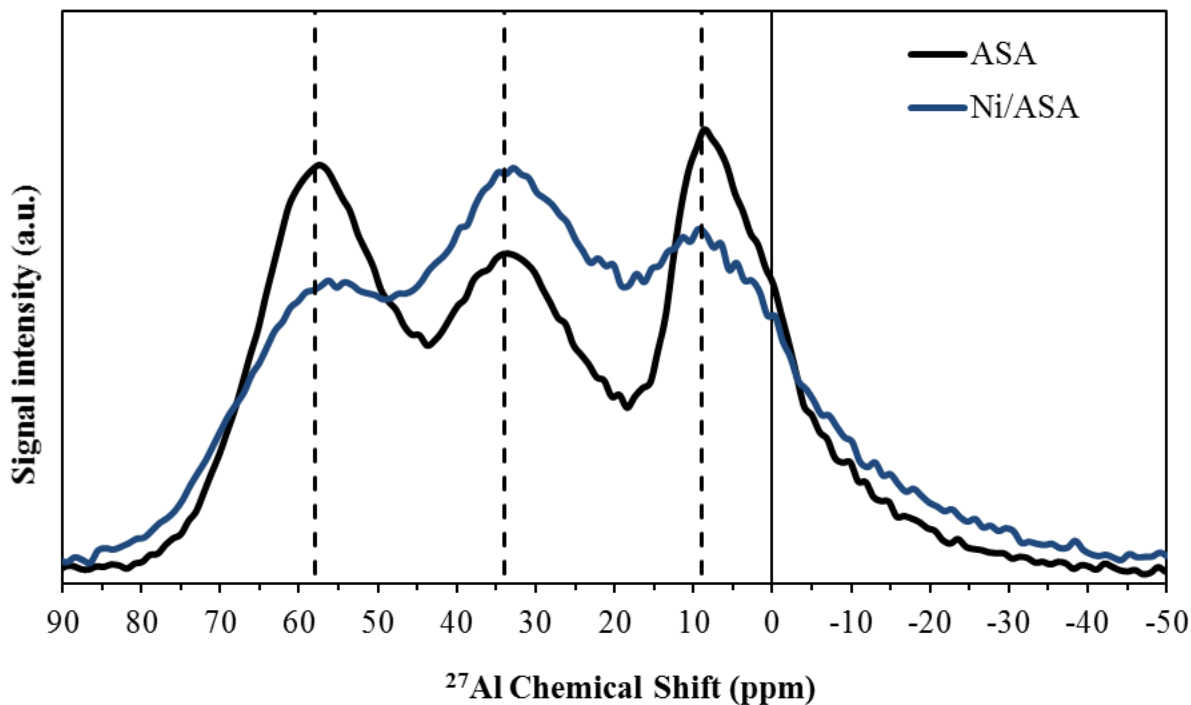


Figure 2.2 ²⁷Al MAS NMR spectra of ASA before and after nickel incorporation.

Hydration of the sample before analysis has been shown to reduce asymmetric quadrupolar interactions about aluminum, and hence reveal more sites through NMR analysis, and should be attempted in future work.¹⁰⁰ Treatment with an ammonia-water solution was shown to aid in redistributing 5- and 6-coordinate Al to tetrahedral sites in ASA.¹⁰¹ Exposure to ammonia can induce the conversion of 6-coordinate Al to become pentacoordinate¹⁰² Five-coordinate aluminum appear to avoid formation along the surface of ASAs, and favor rather the intersections of alumina domains and the mixed silica-alumina phase.¹⁰²⁻¹⁰⁵

The enrichment of penta-coordinate aluminum upon nickel incorporation suggests that these species may arise to adjoin a nickel-rich phase to either the alumina domains or the silica-alumina phase. In accordance with the TPR results, the nickel-rich phase may consist of a phyllosilicate-type layered structure that is abutted by penta-coordinate aluminum sites at the interface of more aluminum-rich domains. The above descriptions of flexible coordination amongst aluminum in zeolites and especially ASAs may play an important role in not only the incorporation of aluminum in non-ion exchange-type positions, but also in the hemilabile stabilization of the working nickel site as it becomes ligated by ethylene during oligomerization.

2.3.3 Synthesis of XAS Model Compounds

The model nickel compounds for XAS analysis were selected based on having 1) discrete coordination numbers of 4, 5, and 6 nearest-neighbors 2) existing literature concerning synthesis and XAS interpretation 3) preferably having inorganic, oxidic structures similar to known active heterogeneous nickel-containing oligomerization catalysts 4) stable and non-toxic properties.

The work by Farges et al.¹⁰⁶ demonstrated that the coordination number of nickel within inorganic oxides could be determined through XAS in a quantitative manner by analysis of the pre-edge feature and Ni-O neighbor distance fitted from EXAFS. Amongst other model compounds, the inorganic compounds NiCr_2O_4 , KNiPO_4 , and NiO were utilized by Farges as 4-, 5-, and 6-coordinate model species, and were thus pursued as model compounds in this work.

Although NiCr_2O_4 possesses uniquely carcinogenic properties, no suitable 4-coordinate replacement was found in literature. Further, the thermal synthesis of stoichiometric nickel and chromium precursors was described in a straightforward manner by Suchomel et al.⁷⁹ and was subsequently used to prepare the sample used in this work.

XRD showed the resulting material to be of high purity and crystallinity (Figure 2.3), although some shifts in peak positions from card file 01-076-2184 were observed, due likely to a temperature-dependence of the crystal structure of nickel chromite. Upon cooling through 310 K, and the crystal transitions from a cubic to a tetragonal symmetry. Further cooling distorts the tetragonal phase by elongation of the c and contraction of the a lattice parameters, followed by a splitting of the a tetragonal parameter at 65 K to form an orthorhombic phase.⁷⁹

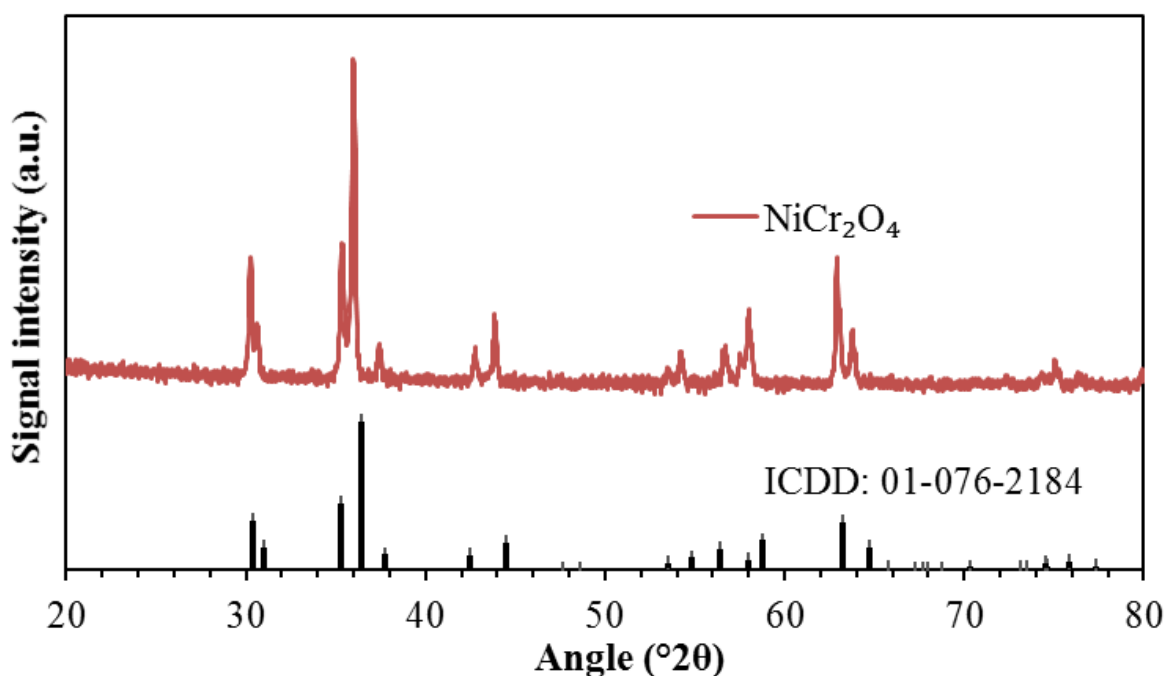


Figure 2.3 XRD pattern of model compound NiCr₂O₄.

The synthesis of 5-coordinate KNiPO₄ was less clear. Farges et al. had referenced the work of Lyutin et al.¹⁰⁷, published in Soviet Physics – Doklady in 1973, in which the authors described their synthesis method as “spontaneous crystallization” from an equimolar NiO and K₂HPO₄. More recently, preparation of the 6-coordinate KNiPO₄•6 H₂O was described by Trobajo et al., in which it was noted that a weight loss of 35.9%, corresponding to complete

dehydration, was achieved at 800 °C during thermogravimetric analysis (TGA) in a nitrogen atmosphere.⁸⁰ A thermal synthesis for the anhydrous 5-coordinate compound was described by Galois et al.¹⁰⁸, in which nickel sulfate and KH_2PO_4 were heated to 900 °C in a platinum crucible for 20 h.

In this work, the hydrated precursor $\text{KNiPO}_4 \cdot 6 \text{H}_2\text{O}$ was synthesized according to Trobajo⁸⁰, which resulted in a suspension of light green particles. The suspension was then separated by filtration, and the supernatant centrifuged. Upon drying, the filtered particles appeared dark olive in color, while the centrifuged slurry retained a bright candy apple green color (Figure 2.4). This was presumably due to differences in water content, although further differences in the stoichiometry of the precursors in each sample could not be ruled out.



Figure 2.4 Filtered (left) and centrifuged (right) KNiPO_4 hydrate prior to calcination.

TGA experiments were then performed to verify a suitable calcination procedure for the hydrated crystals. Upon heating under flowing zero air, a steady mass loss was observed that stabilized at approximately 500 °C. The loss in mass then increased slowly up to 700 °C, whereupon further heating to 1000 °C, the sample unexpectedly began to regain mass.

Consequently, a calcination of the hydrate was performed at 550 °C for 5 h in air in effort to obtain the dehydrated, 5-coordinate KNiPO₄ compound. Following calcination, both the filtered and centrifuged samples obtained a brownish-red ochre color (Figure 2.5), with the filtered crystals appearing lighter in tint.



Figure 2.5 Filtered (left) and centrifuged (right) KNiPO₄ after calcination.

XRD of the centrifuged material indicated the presence of at least two crystalline phases (Figure 2.6). The main phase was identified as KNiPO₄ by comparison with card file 01-086-0573 from the International Centre for Diffraction Data (ICDD). The presence of a dilute secondary phase was evidenced by a mismatch of peak intensities at 30.4, 31.7, and 32.7 °2θ. This phase was identified as a nickel-rich analogue of the desired compound having a stoichiometry of K₂Ni₄(PO₄)₂ by comparison with ICDD 00-041-0335. Quantitative analysis was performed by the relative intensity ratio (RIR) method using the PDXL software. As noted by ICDD, this method can impart significant errors if there are non-crystalline or unidentified phases present in the sample.

A visual inspection of Figure 2.6 shows a satisfactory match with the card file for KNiPO_4 . Absent the presence of large amorphous domains, this approach appears appropriate to estimate the fraction of the desired 5-coordinate KNiPO_4 . The sample was determined to be a 90:10 mixture of the KNiPO_4 and $\text{K}_2\text{Ni}_4(\text{PO}_4)_2$ components, respectively. Interestingly, the dilute nickel-rich phase in the centrifuged sample appeared as the dominant phase in the filtered hydrate crystals (Figure 2.7). Based on these data, the sample of KNiPO_4 obtained by centrifugation and drying of the filtered supernatant was selected to represent 5-coordinate nickel compounds in further analysis by XAS.

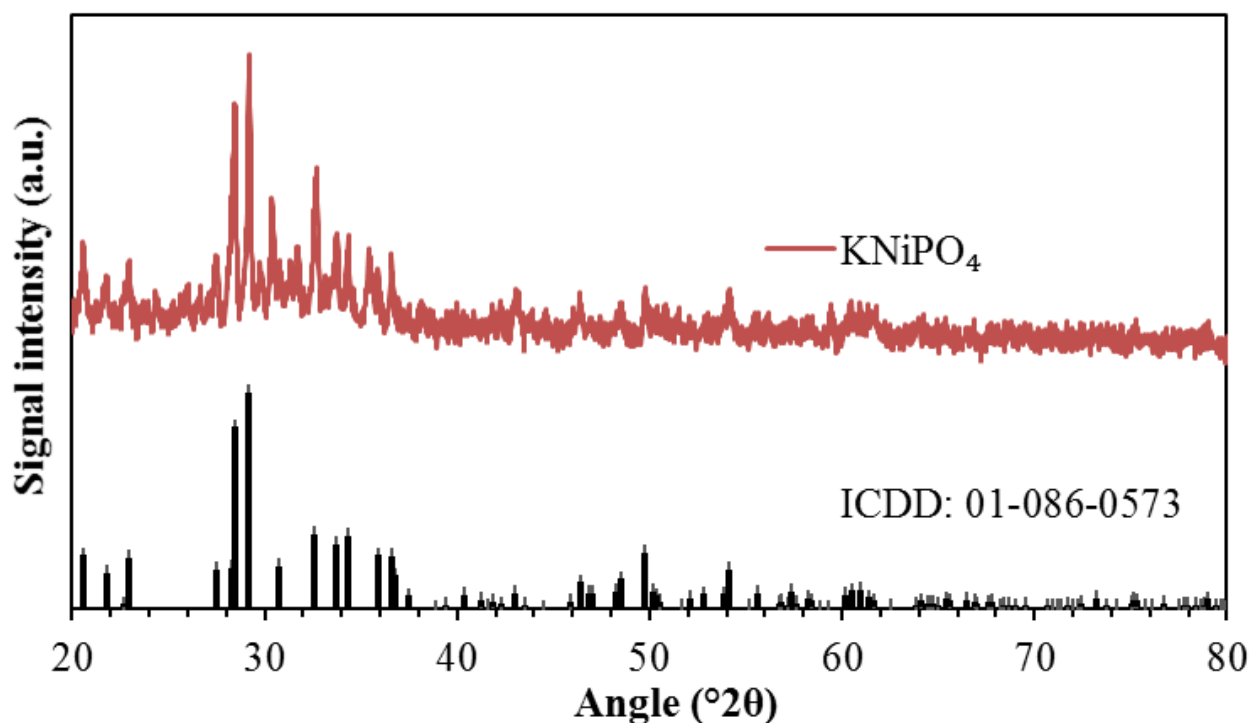


Figure 2.6 XRD pattern of the calcined model compound KNiPO_4 obtained from the centrifuged supernatant.

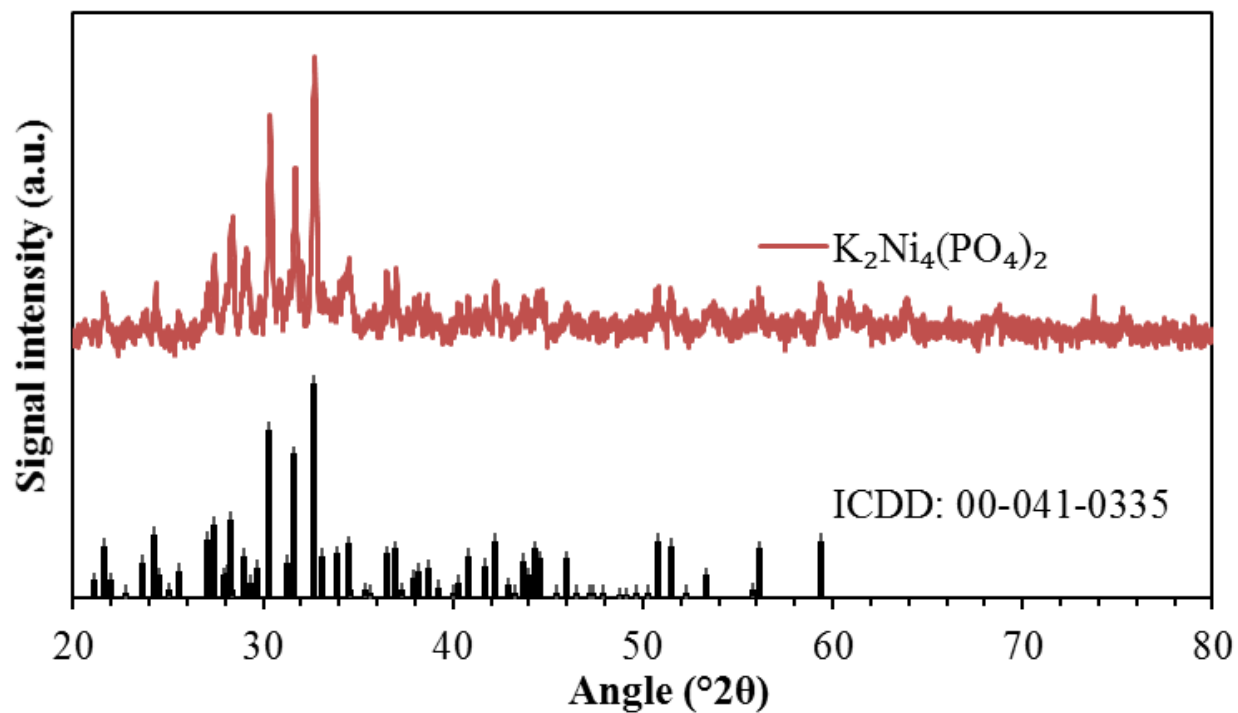


Figure 2.7 XRD pattern of calcined model compound KNiPO_4 obtained from filtered crystals.

The crystal structure of nickel oxide, as modeled in the crystal making software VESTA, is shown in Figure 2.8 having nickel arranged in a 6-coordinate rock salt-type lattice.

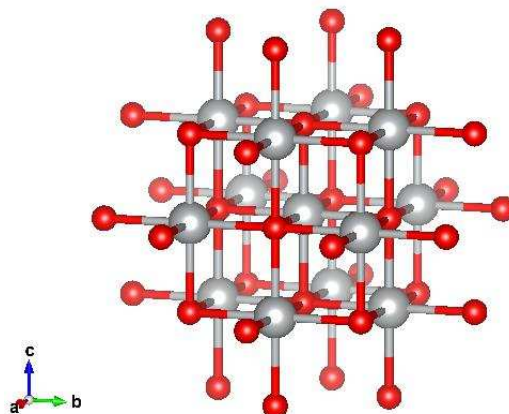


Figure 2.8 Crystal structure of NiO . Nickel is depicted as gray spheres, and oxygen as red spheres.

The crystal structure of KNiPO_4 is shown in Figure 2.9, where nickel has 5 oxygen nearest neighbors in a tetragonal pyramid, or distorted square pyramid-type geometry.

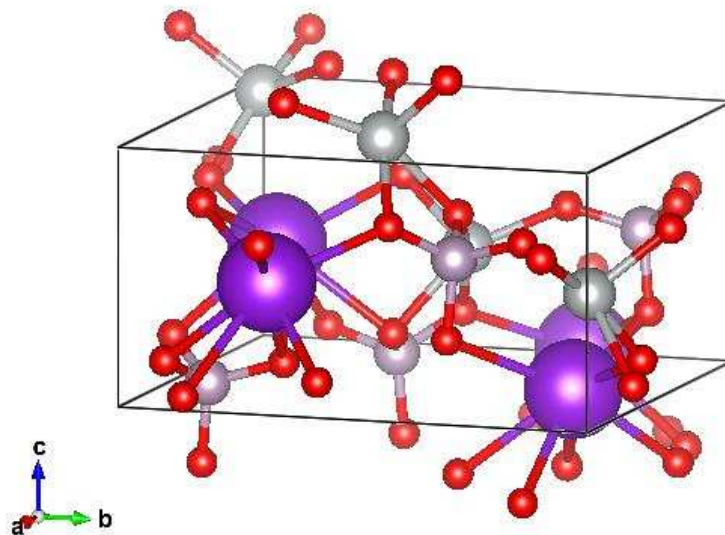


Figure 2.9 Crystal structure of KNiPO_4 . Nickel is depicted as gray spheres, oxygen as red spheres, potassium as dark purple spheres, and phosphorous as light purple spheres.

The crystal structure of NiCr_2O_4 is shown in Figure 2.10, where nickel has four bonds to oxygen in a tetrahedral geometry.

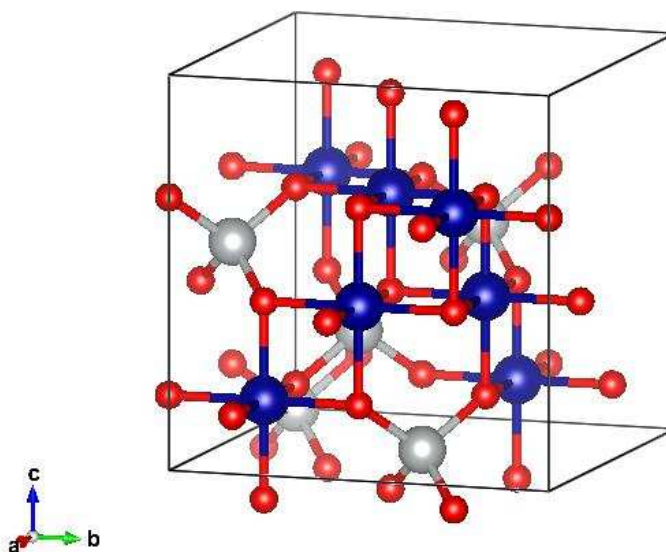


Figure 2.10 Crystal structure of NiCr_2O_4 . Nickel is depicted as gray spheres, oxygen as red spheres, and chromium as blue spheres.

2.3.4 X-ray Absorption Spectroscopy

The X-ray absorption spectra of model compounds NiCr_2O_4 , KNiPO_4 , and NiO , are shown in Figure 2.11. These compounds demonstrate nickel oriented in crystalline 4-, 5-, and 6-coordinate positions, respectively. The edge crest of NiCr_2O_4 was split into three defined peaks at 8349, 8353, and 8357 eV, and had a very slight edge shoulder at 8343 eV that appeared absent in the higher coordinate compounds. The 5- and 6-coordinate compounds appeared closely matching in the XANES region, with edge-crests of similar intensity at 8349 and 8350 eV, respectively, but had substantial differences EXAFS region as well as the edge crest shoulder at 8360 eV that was present in KNiPO_4 though absent for NiO .

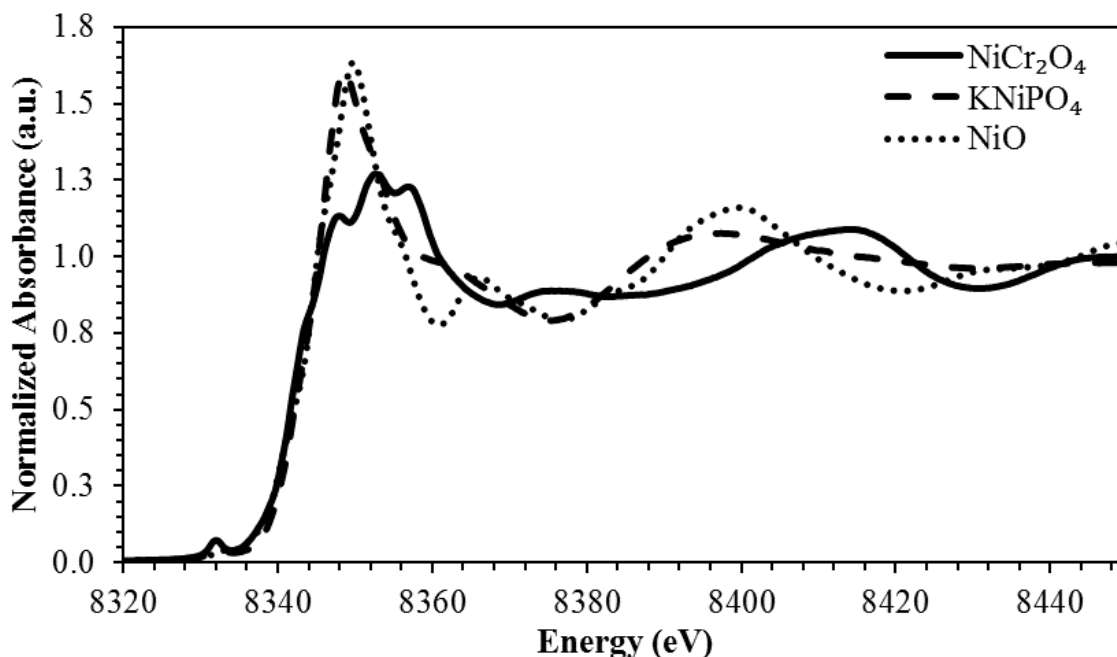


Figure 2.11 Ni K-edge XAS spectra for model compounds NiCr_2O_4 , KNiPO_4 , and NiO .

The XAS spectra of the pretreated catalysts is shown in Figure 2.12. As an aid to the eye, the catalyst spectra were overlaid atop those of the model compounds shown in Figure 2.11. Ni/SiO_2

and Ni/Al₂O₃ were found to have strong similarities to bulk NiO, with Ni/SiO₂ demonstrating the closest overlap in both the XANES and EXAFS regions. The spectrum of Ni/Al₂O₃ showed a slight upward shift of the edge crest to 8352 eV, then diverged from the spectrum of NiO in the multiple scattering region above 8355 eV to then align more closely with the 5-coordinate model compound KNiPO₄.

The spectra of Ni/Al-MCM-41, Ni/ASA, and Ni+Na/ASA were highly alike, and were a close match to KNiPO₄ despite subtle reductions in intensity for the edge crest at 8350 eV and the single-scattering shoulder at 8360 eV. As a fingerprint comparison, these features of the active materials appeared as a surprisingly close match. An absent pre-edge shoulder at 8338 eV, formed from 1s to 4p_z transitions in systems with square planar and square pyramidal geometries¹⁰⁹⁻¹¹⁰, was evidence that the KNiPO₄ indeed possessed a distorted square-pyramid geometry as reported.¹⁰⁷

The pre-edge spectral region for the model compounds is shown in Figure 2.13. The pre-edge peak was shifted to lower energy and increased in intensity in the order of NiO, KNiPO₄, NiCr₂O₄, with decreasing positions of 8331.5, 8331.2, and 8330.8 eV, respectively. The edge onset above 8334.0 eV was delayed for KNiPO₄ relative to NiO and NiCr₂O₄. The pre-edge is governed by a 1s to 3p transition, where the increased p-d hybridization in 4- and 5-coordinate geometries results in an increased pre-edge intensity and lower energy.¹⁰⁶ These results are coherent with this understanding of the behavior.

The pre-edge spectral region of the pretreated catalysts is shown in Figure 2.14, overlaid atop that of the model compounds. The pre-edges for Ni/Al-MCM-41, Ni/ASA, and Ni+Na/ASA were centered about 8332.5 eV and had intensities close to KNiPO₄. Ni/Al-MCM-41 exhibited the highest intensity, although it may be due to differences in baselining as observed at low eV.

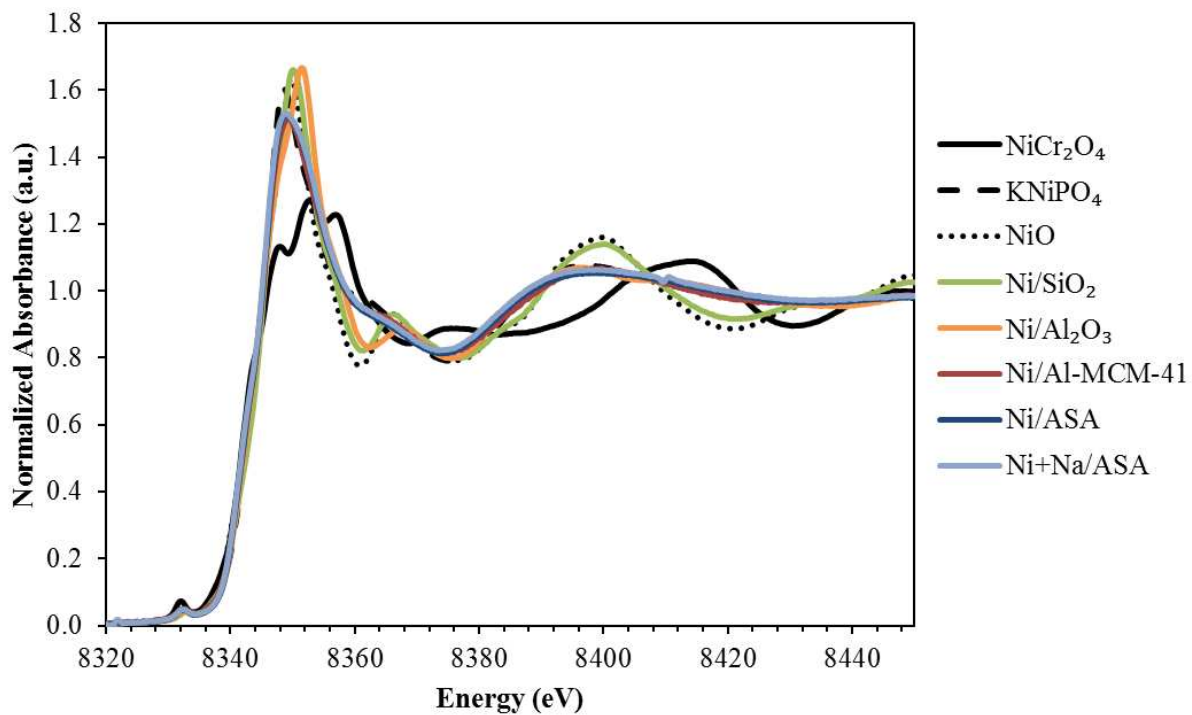


Figure 2.12 Ni K-edge XAS spectra for catalyst samples Ni/SiO₂, Ni/Al₂O₃, Ni/Al-MCM-41, Ni/ASA.

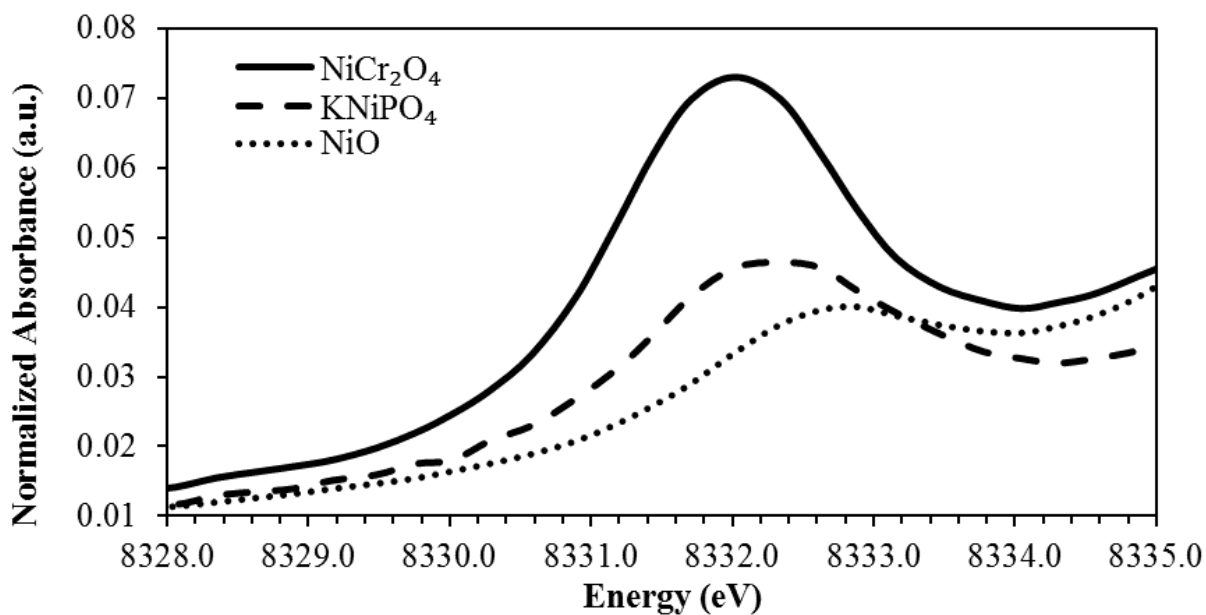


Figure 2.13 High-resolution Ni K-edge pre-edge features for model compounds NiCr₂O₄, KNiPO₄, and NiO.

The pre-edge peaks of Ni/SiO₂ and Ni/Al₂O₃ were centered about 8332.7 eV and had intensities intermediate that of the 5- and 6-coordinate model compounds. In general, the peak shape of the active materials was less defined, appearing even to be bimodal for each. It is uncertain if this was due to actual differences in the nickel environment or the lower signal to noise ratio obtained from lower nickel loadings.

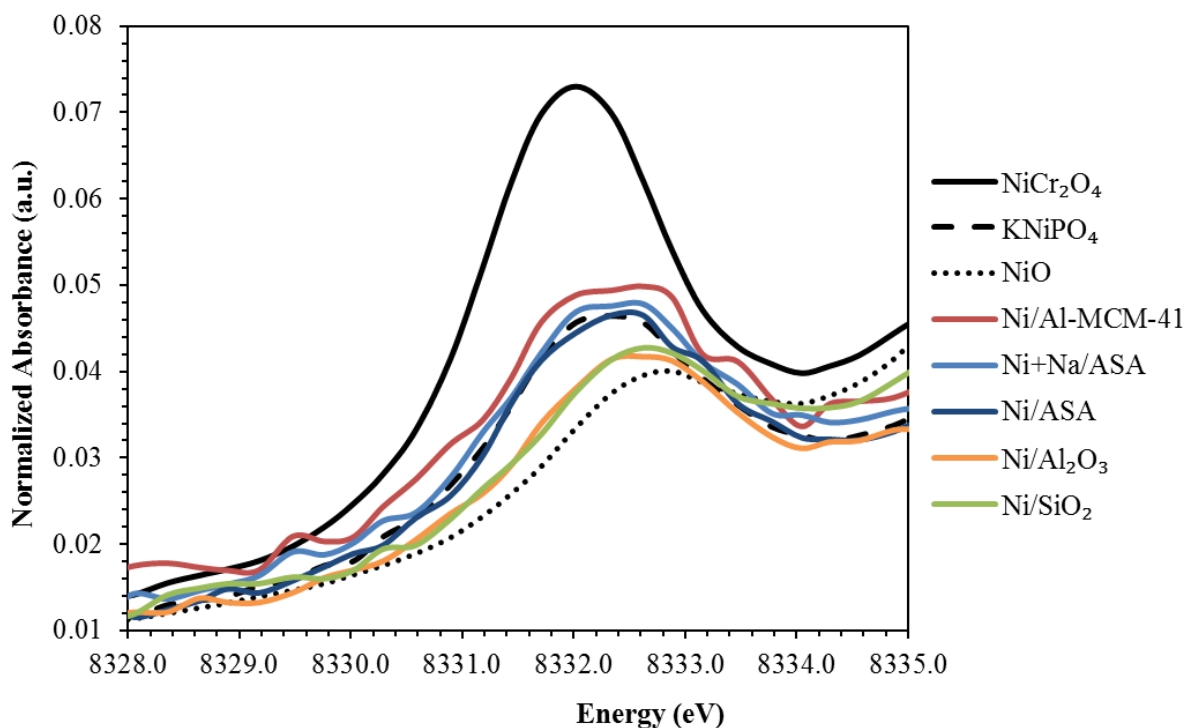


Figure 2.14 High-resolution Ni K-edge pre-edge features for catalysts Ni/SiO₂, Ni/Al₂O₃, Ni/Al-MCM-41, Ni/ASA, and Ni+Na/ASA.

A plot of the pre-edge information from the model compounds and catalysts is shown in Figure 2.15, where the relationship between coordination number and pre-edge position and intensity appears clearly. In line with the work of Farges et al.¹⁰⁶, the 4-coordinate NiCr₂O₄ exhibited both the most intense pre-edge as well as the lowest pre-edge energy, while 6-coordinate NiO had the lowest pre-edge intensity and highest pre-edge energy. The less active

catalysts, Ni/SiO₂ and Ni/Al₂O₃, exhibited a character intermediate that of NiO and KNiPO₄, and tended toward the properties of bulk NiO.

The more active materials, Ni/Al-MCM-41 and Ni/ASA were both very similar to the 5-coordinate KNiPO₄ model compound. These results clearly demonstrate a performance-property relationship that is based on the coordination number of nickel, where a lower coordination results in a more active catalyst. As these results are derived from a bulk analysis, it is important to note that mixtures of 4- and 6-coordinate nickel compounds can produce results that appear intermediate of one another.¹⁰⁶

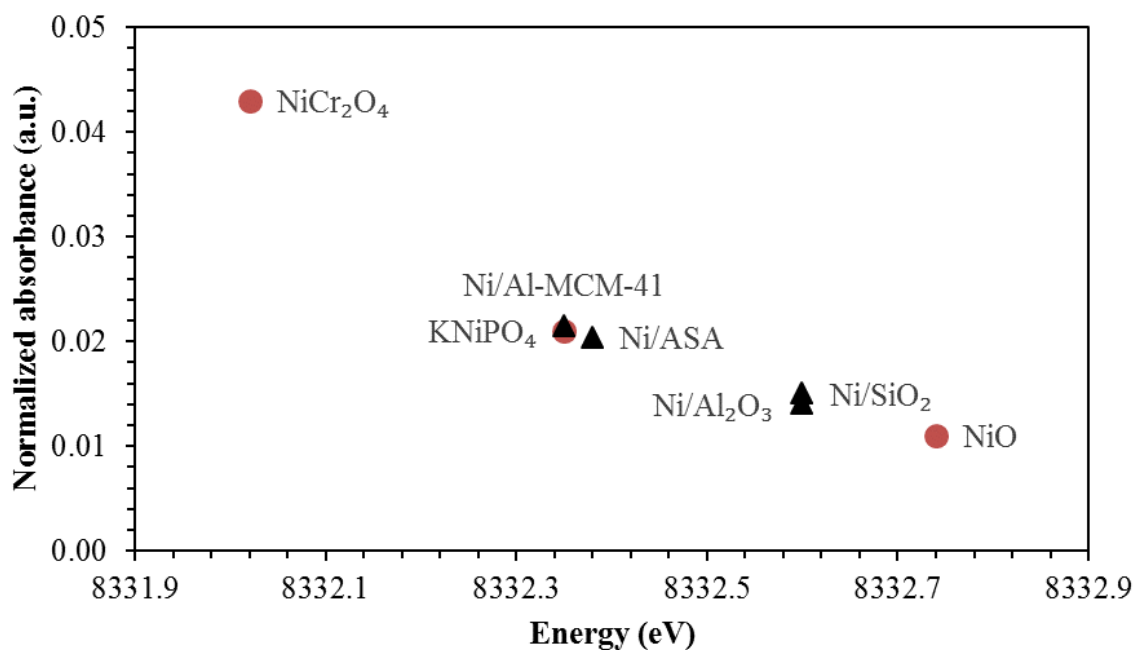


Figure 2.15 Plot of pre-edge information for the model compounds (red circles) and catalysts (black triangles) showing relation between coordination number and pre-edge properties.

As demonstrated by Farges et al.¹⁰⁶, a trend also appears between the fitted EXAFS nearest-neighbor distance and the pre-edge intensity. This relation describes a contraction of the

nearest-neighbor distances as the coordination number of nickel goes down. The 6-coordinate NiO featured a Ni-O bond distances of 2.08 Å, whereas 5-coordinate KNiPO₄ was 2.03 Å, and 4-coordinate NiCr₂O₄ was 1.96 Å. Ni/SiO₂ bore strong similarity to the bulk NiO sample based on average Ni-O distance. The most active materials, Ni/ASA and Ni/Al-MCM-41, were fitted to average Ni-O distances smaller than the 5-coordinate KNiPO₄, whereas Ni/Al₂O₃ was very similar. It is not unreasonable to expect differences between samples where Ni was introduced selectively onto the surface and the bulk model compounds, in which Ni inhabits a well-ordered, three-dimensional environment that constitutes a specific coordination. For supported nickel, ligand interactions would be expected to be highly anisotropic and oriented towards the direction of the support surface. Consequently, the resulting fitted geometry and average Ni-O distance may be quite different from bulk, crystalline structures.

The trend between the pre-edge peak intensity and average Ni-O distance appeared less clean (Figure 2.16) than with that of pre-edge energy. This difference may be due to the relative uncertainty of each analysis, where the EXAFS fitting involved greater interpretation than a simple measurement of the pre-edge information. The materials themselves may also exhibit variation due to unique bond environments as described above.

To understand the influence of ethylene exposure on nickel coordination, the pre-edge region was monitored with high resolution energy steps of 0.05 eV before and after exposure to ethylene, as shown in Figure 2.17. There appeared no discernible changes in the peak position and intensity for any of the materials, except for the peak of Ni+Na/ASA, which, although noisy, appeared to shift to higher energy from 8332.3 eV to 8332.6 eV, suggesting an increase in coordination number. This shift in peak position did not correspond with a change in peak intensity, however, in conflict with this interpretation. Thus, the change is interpreted as noise.

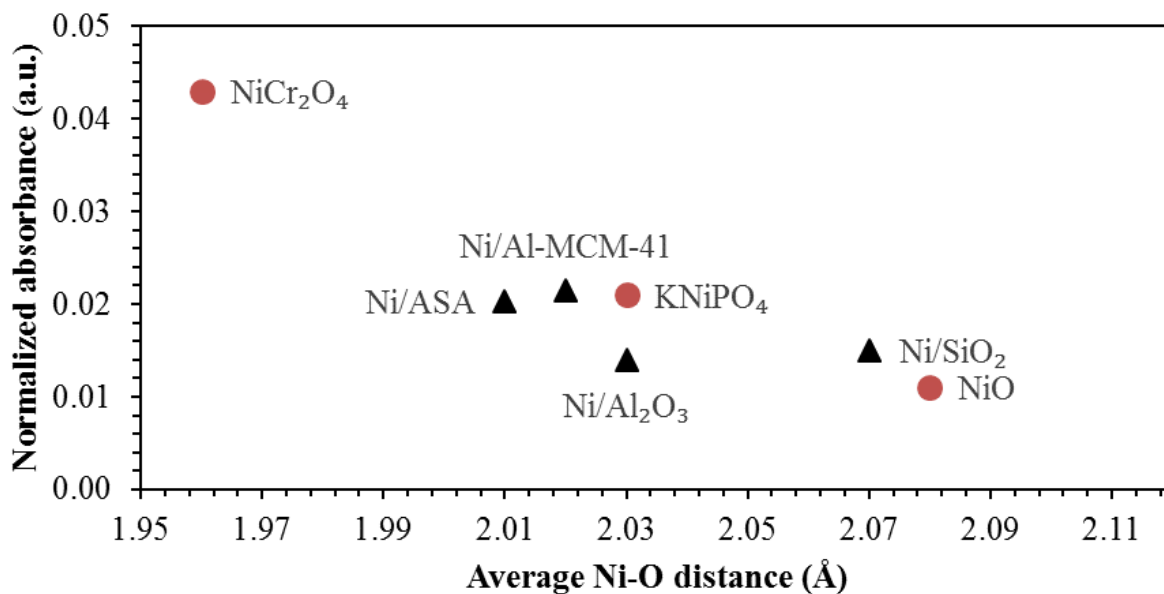


Figure 2.16 Fitted EXAFS nearest-neighbor distance and pre-edge intensity of the model compounds (red circles) and catalysts (black triangles).

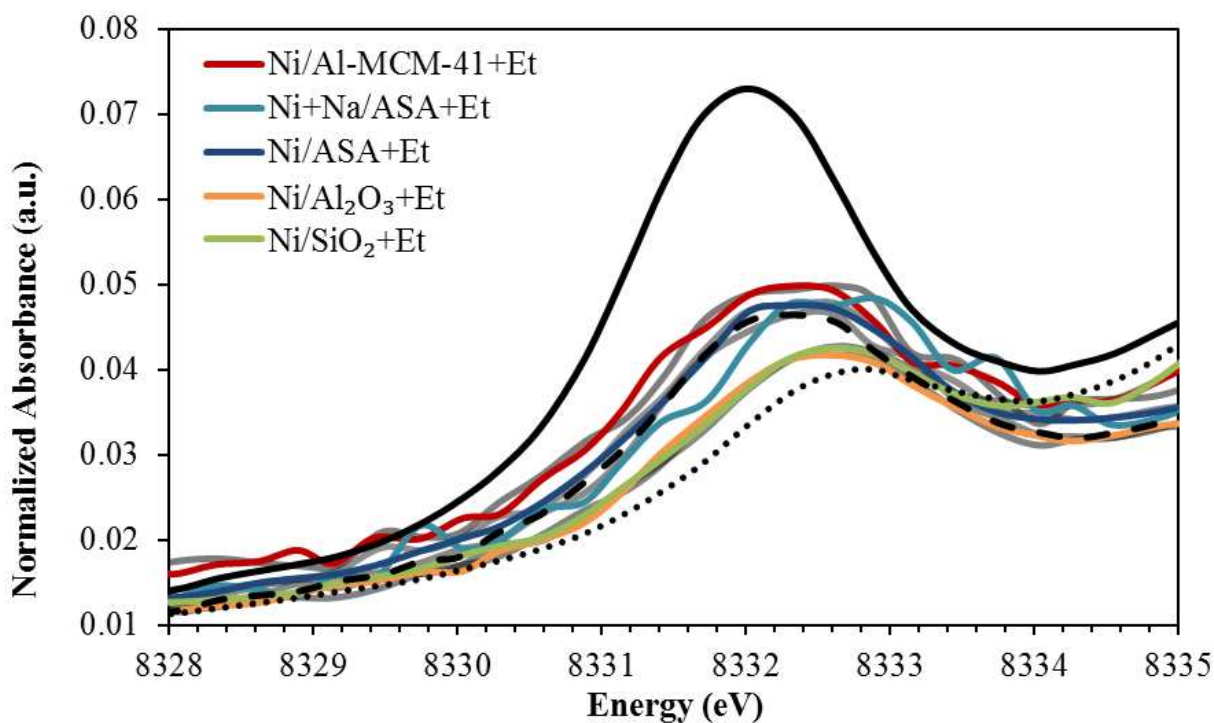


Figure 2.17 High-resolution Ni K pre-edge features for catalysts after exposure to ethylene. Spectra of the pretreated catalysts before exposure to ethylene are shown in gray.

The EXAFS spectra of the model compounds are shown in Figure 2.18. These spectra are not intended to be interpreted as radial distribution functions. However, the results will be described qualitatively for comparative purposes. The intensity of the first shell nearest oxygen neighbors between 0.5 and 2.0 Å was similar for the three model compounds, although slightly lower for KNiPO₄. NiO exhibited a strong second shell peak between 2.0 and 3.0 Å that was assigned to a Ni-O-Ni next nearest neighbor. KNiPO₄ did not have a strong second nearest neighbor, but rather two weak peaks were observed. The fit of NiCr₂O₄ showed an intense peak between 3.5 and 4.5 Å and was assigned to a Ni-O-Cr next nearest neighbor.

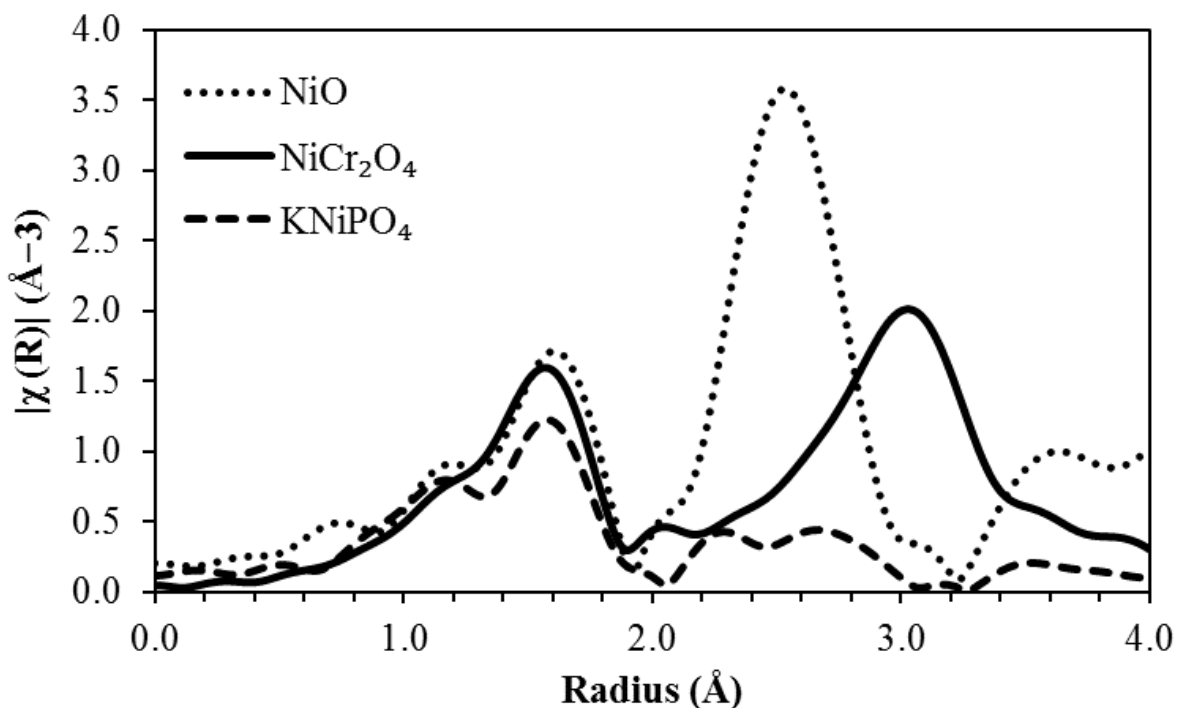


Figure 2.18 Magnitude of the Fourier-transform of the Ni K-edge EXAFS spectra of the model compounds.

The EXAFS spectra of the pretreated catalysts are shown in Figure 2.19. The first and second coordination shells of Ni/SiO₂ were higher in intensity than all other catalysts. This

suggested a larger cluster size for NiO present on this support than all other materials. Although the first coordination shell of Ni/Al₂O₃ was very similar to that of Ni/SiO₂, the second coordination shell was substantially less intense.

Subtle differences in the first coordination shell of Ni/ASA appeared upon incorporation of sodium that were observed as a shift and increase in intensity of the first observed peak at approximately 0.9 Å for Ni/ASA to 1.1 Å for Ni+Na/ASA. This restructuring of the inner shell coordination environment of nickel upon inclusion of sodium is consistent their co-location in the support. This is expected due to their cationic nature and their predisposition to orient in positions adjacent strong anionic charge (ion exchange-type positions) within the support.

The second shell intensities of the Ni/ASA and Ni+Na/ASA materials were very similar and were the lowest of all samples tested. This was evidence for a high dispersion of nickel on these supports, and the absence of large nickel oxide nanoclusters. Ni/Al-MCM-41 had a first coordination shell with a unique set of close peaks, evident at *ca.* 0.6, 1.0, and 1.5 Å, and a second coordination shell having similarity to Ni/Al₂O₃.

The EXAFS zones of the pretreated catalysts before and after exposure to ethylene are shown in the following figures. The difference spectra of before and after exposure is plotted as a red dotted black line to highlight changes in the fits.

Nickel on silica showed virtually no change upon exposure to ethylene amongst the studied materials (Figure 2.20). This result at least confirmed the consistency of this technique under these conditions.

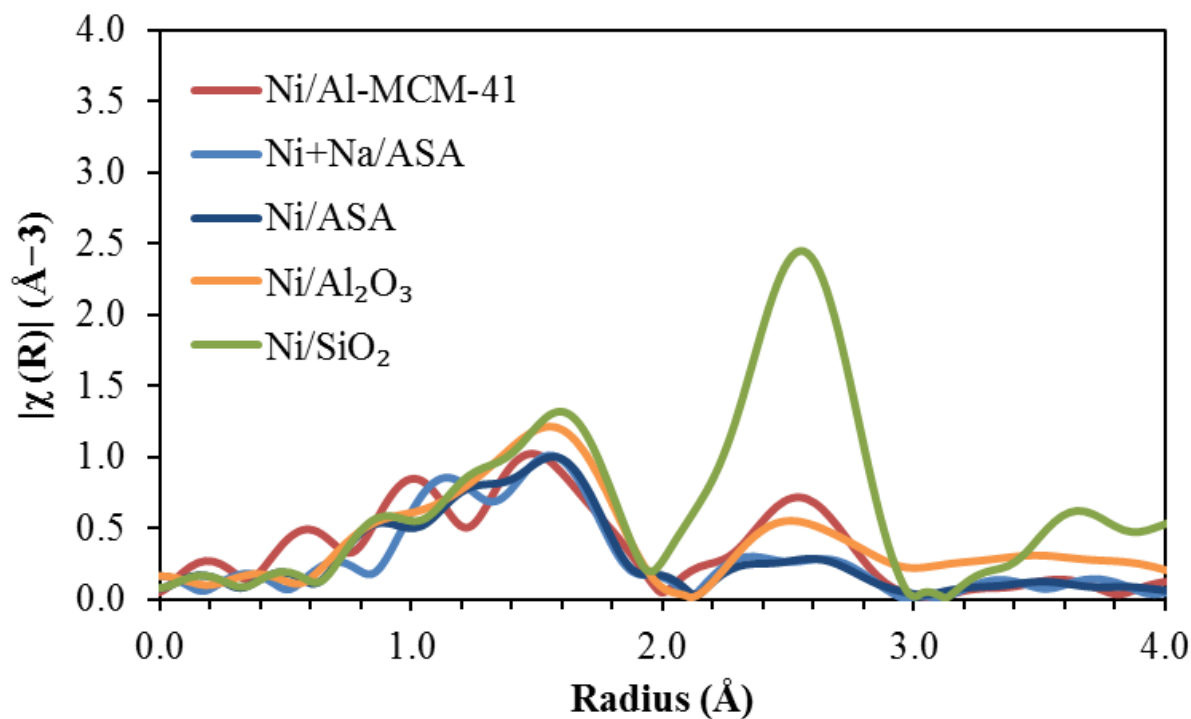


Figure 2.19 Magnitude of the Fourier-transform of the Ni K-edge EXAFS spectra of the pretreated catalysts.

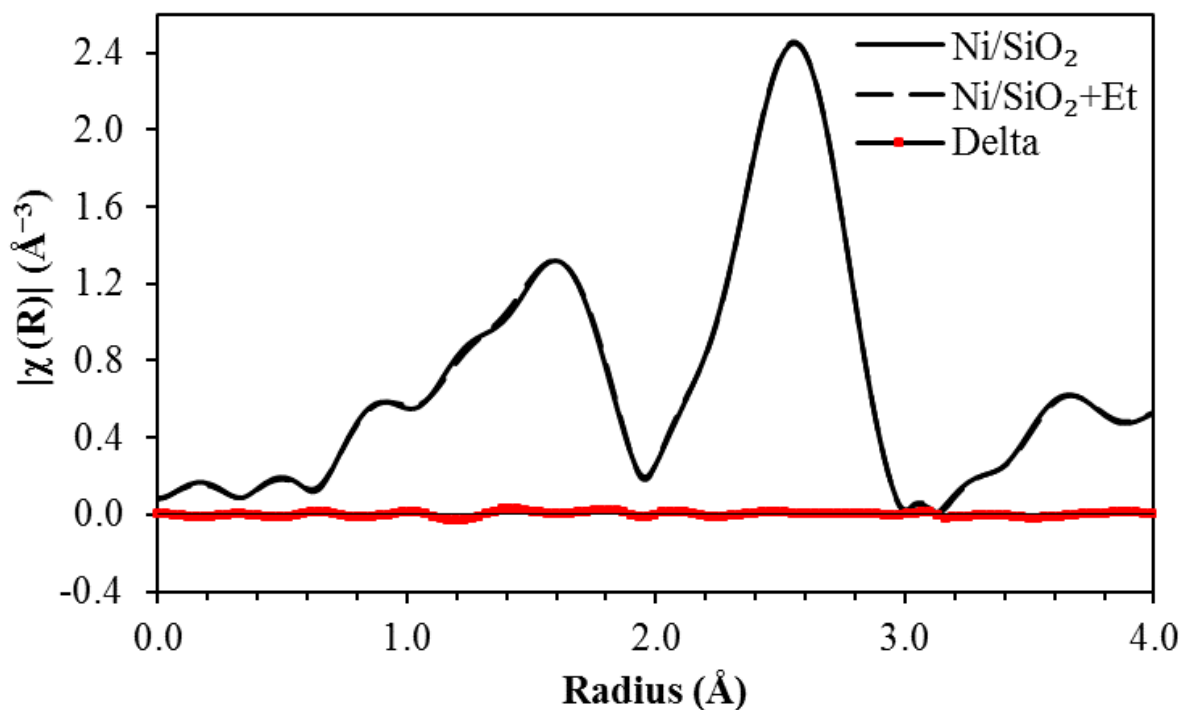


Figure 2.20 Magnitude of the EXAFS Fourier-transform of Ni/SiO₂ before and after exposure to ethylene.

Nickel on alumina showed some restructuring of the coordination environment when exposed to ethylene (Figure 2.21), observed as a decrease in scattering intensity at 0.8 Å and small increases at approximately 0.6 and 1.0 Å. No substantial changes were observed in the most intense part of the spectrum at 1.5 Å, although the region bridging the first and second shells between 2.0 and 3.0 Å showed small increases.

Changes in the scattering features of Ni/ASA exhibited similar behavior as nickel on alumina, with the exception that the main loss in intensity at 0.8 Å was accompanied by stronger increases in the region between 1.0 and 3.0 Å, and especially between 1.0 and 2.0 Å (Figure 2.22). More fluctuations were also observed below 0.8 Å, all suggestive of a greater degree of site restructuring around nickel on this catalyst in the presence of ethylene than on the less active materials.

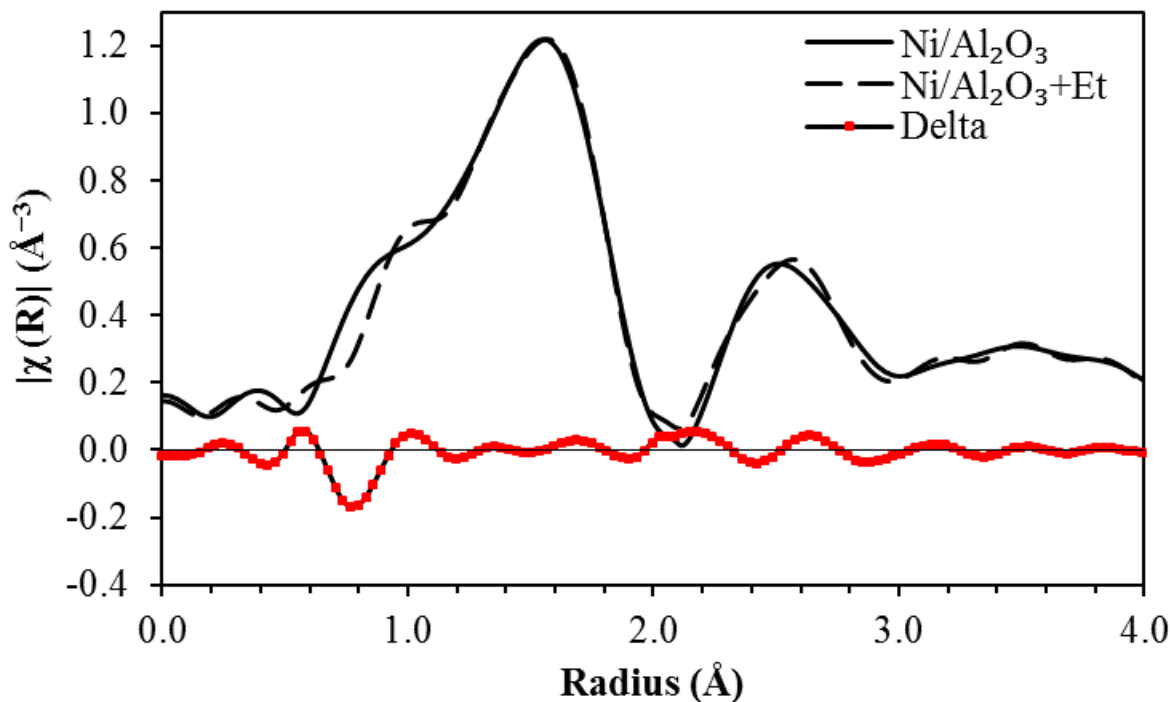


Figure 2.21 Magnitude of the EXAFS Fourier-transform of $\text{Ni/Al}_2\text{O}_3$ before and after exposure to ethylene.

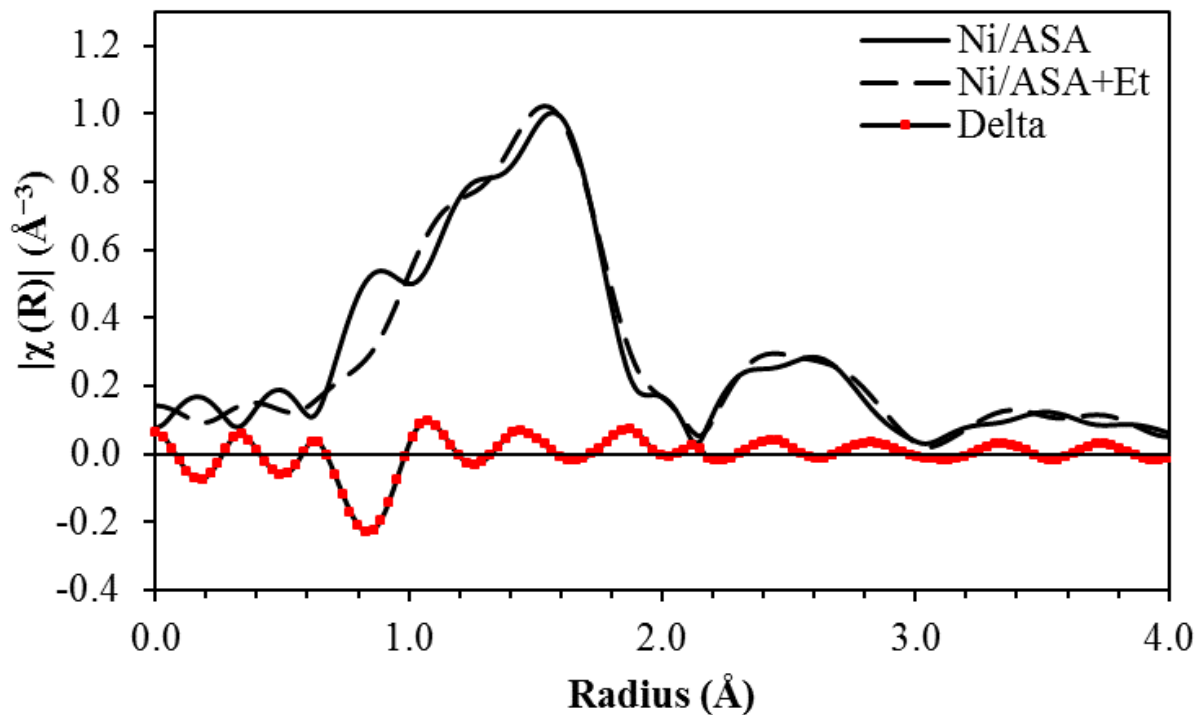


Figure 2.22 Magnitude of the EXAFS Fourier-transform of Ni/ASA before and after exposure to ethylene.

The Ni+Na/ASA sample exhibited strong fluctuations in the EXAFS, primarily in the first coordination shell (Figure 2.23). This suggested the highest degree of restructuring for all samples tested. The position of the main decrease shifted upward to 1.1 Å and was accompanied by an additional secondary decrease at 1.6 Å. These loss peaks were closely matched in intensity by gains at 0.9, 1.3, and 1.9 Å. The fluctuations in scattering intensity below 0.9 Å were similar to the sodium-free nickel on amorphous silica alumina sample. These results cast some doubt on interpretation for this sample of the pre-edge changes as merely fluctuations due to noise. However, a repetition of this experiment may be in order to address these results. For Ni/Al-MCM-4, the scattering intensity mainly decreased within the first shell, with three loss peaks at 0.4, 0.7, 1.1, and 1.8 Å and a single positive feature at 1.3 Å (Figure 2.25). Little changes were observed in the second shell.

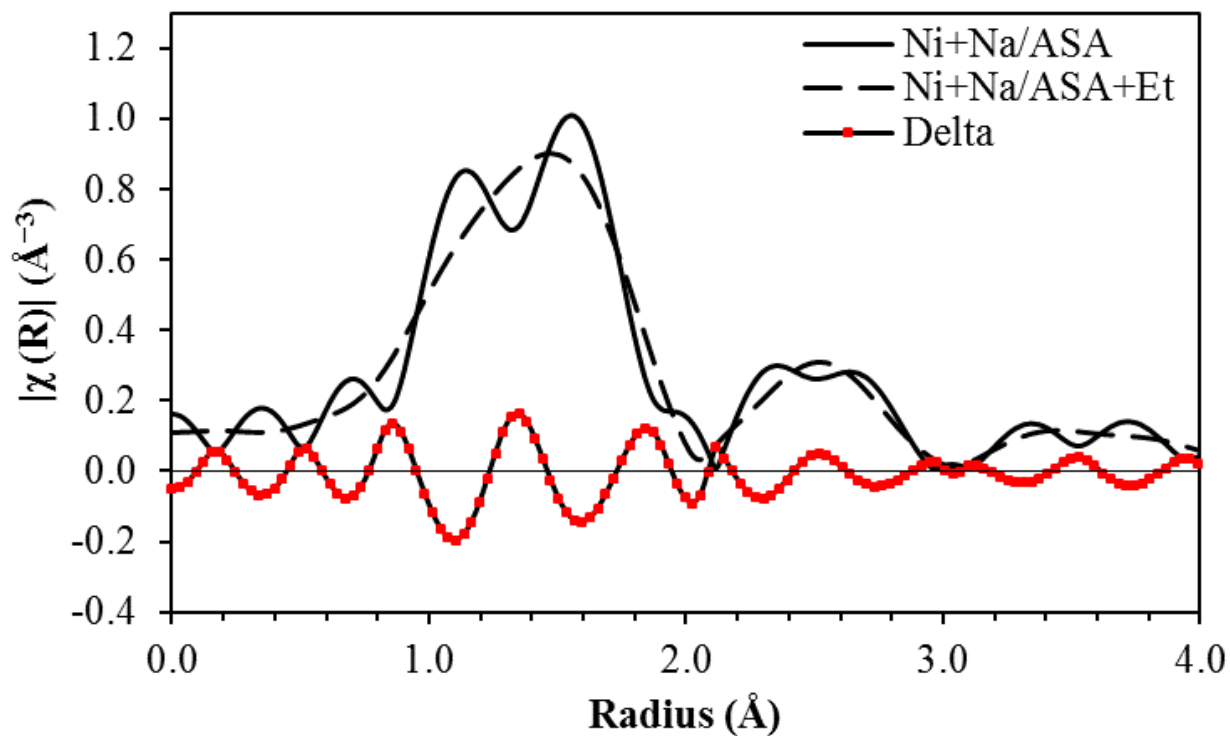


Figure 2.23 Magnitude of the EXAFS Fourier-transform of Ni+Na/ASA before and after exposure to ethylene.

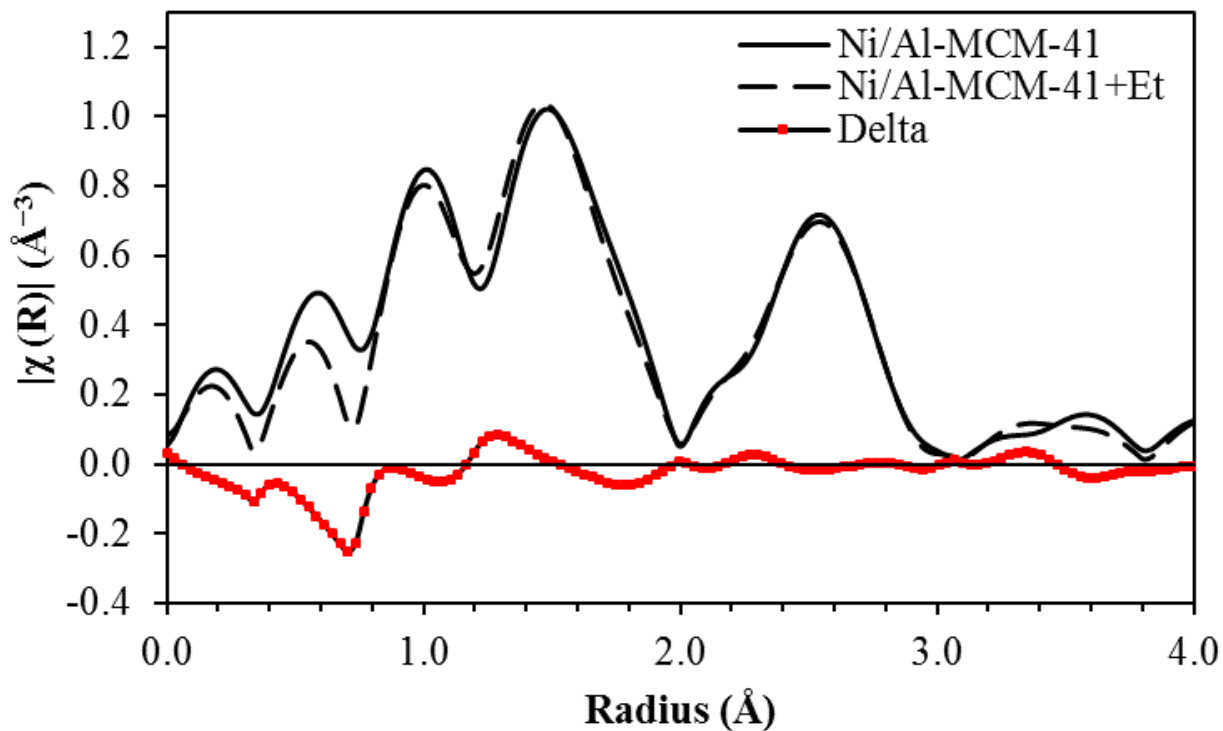


Figure 2.24 Magnitude of the EXAFS Fourier-transform of Ni/Al-MCM-41 before and after exposure to ethylene.

2.3.5 DRIFTS Experiments

A DRIFTS study of the interaction of CO with a Ni/ASA sample was performed to qualitatively determine the effect of sample pretreatment on the character of nickel speciation, and to further correlate support interactions. Two pretreatments were studied. The first was representative of a suitable pretreatment to activate the catalyst prior to oligomerization reactions, and constituted heating to 200 °C under a flow of inert (nitrogen) for 3 h. The second was a harsh reduction by exposure to 5% H₂ at 500 °C for 2 h. Reductive pretreatments have been used to activate nickel on silica, presumed to be by the formation of Ni^I, and to promote the formation of trimers over dimers.¹¹¹

The distribution of nickel site environments is of key interest in this work, and of particular importance to interacting with and oligomerizing ethylene, their relative electrophilicities and coordinative capacities. Carbon monoxide is a uniquely suitable probe for this application, due both to the potential for formation of polycarbonyls with transition metal ions¹¹² and to the sensitivity of the C-O infrared stretching frequency to electron donor-acceptor properties of the interacting species. Upon interaction with an electrophilic, or Lewis acidic, support site, the C-O bond is strengthened by donation of anti-bonding electron density to the surface. This results in a blue-shift from that of physisorbed species at 2143 cm⁻¹, with the calculated stretch of a monocationic CO⁺ being 2184.¹¹³

On highly Lewis acidic supports, the stretch may be observed as high as 2235 cm⁻¹ on low-coordinate, Lewis acidic Al³⁺ found in aluminas and alumino-silicates. The observed range for divalent metal cations is typically between 2220 and 2200 cm⁻¹.¹¹⁴ In contrast to the above Lewis acidic supports, surfaces that back-donate electron density to CO result in stretching

frequencies below that of physisorbed CO by increase of the anti-bonding electron density in the C-O bond. In this case, stretches in the range of 2140 to 2000 cm^{-1} are observed.

Carbon monoxide also interacts with Brønsted acid site centers and weakly acidic hydroxyls.¹¹⁵ However, it must be noted that this interaction depends only on the electrostatic potential of the support surface, and is thus not directly related to the proton-transfer potential of the sites.¹¹⁶ DFT modeling interpreted the interaction between a surface OH group in ASA and CO as a participation of not only the OH site, but the neighboring OH groups and adjacent framework oxygens. The authors expounded on the importance of the electrostatic potential of the entire support surface in this interaction, and further proposed that pseudo-bridging silanol groups adjacent to undercoordinated aluminum in ASAs were capable of greater charge transfer than even the strong Brønsted sites present in MOR zeolites due to these effects. An “exchange” process involving transition metal cations with these supports may thus likely find more favorable interactions with non-traditional acid sites (i.e. Brønsted exchange sites) solely due to more favorable electrostatic stabilization of the charged metal cation. This may be the reason for the retained Brønsted acidity observed in these materials after exchange saturation.^{48, 117} Additionally, DFT calculations have proposed that the Brønsted acidity of silyl oxoniums is enhanced by adjacent Lewis-acidic metal ions.¹¹⁸

Owing to the potential for reduction of cationic nickel species by CO at temperatures above 0 °C⁴⁸, CO-DRIFTS experiments were performed at sub-ambient conditions. Temperature control was achieved *via* a liquid nitrogen-containing cold finger near the sample cell. Fluctuations were observed on the order of approximately 50 °C above and below the average sample temperature of -100 °C, depending on the gas flow rate and cell pressure. However,

repeat measurements did not find the signal to be substantially affected by these temperature fluctuations.

The infrared stretching region of surface-bound CO₂ (2360 to 2320 cm⁻¹) of the activated (plotted in black) and reduced (plotted in red) Ni/ASA samples is shown in Figure 2.25 for varying levels of CO exposure. The formation of surface-bound CO₂ is explained by reaction between labile surface oxygens and the admitted CO. Physisorbed CO₂ was found only to form on the reduced Ni/ASA sample, with a peak at 2345 cm⁻¹, shoulder at 2350 cm⁻¹, and secondary peak at 2330 cm⁻¹. These peaks increased with CO coverage, and no peaks between 1500 and 1700 cm⁻¹ corresponding to bidentate CO₂ were observed.

A work by Peri on amorphous silica alumina reported physisorbed CO₂ to be accompanied by a primary peak at 2375 cm⁻¹, and suggested this peak to be linear bound CO₂ interacting with a strained, reactive oxide ion bridge.¹¹⁹ The proposed example of this bridge was Al⁺O²⁻Al⁺, termed an “ α -site.” The site demonstrated competitive adsorption between CO₂ and a range of titrants such as HCl, NH₃, butene, and H₂O. HCl and butene competed the most strongly and suggested that such sites were better described as being “reactive” than acidic. The absence of this peak here is unexpected. However, a competitive binding of nickel with these reactive “ α -sites” during the exchange process is a feasible explanation for the absence of any observed CO₂ interaction. This hypothesis could be tested by analysis of the nickel-free support under equivalent conditions.

No strong evidence for surface-bound CO₂ was observed on the pretreated Ni/ASA sample beyond subtle disturbances in the baseline. This result describes the pretreated surface as having oxygens with higher stability than that of the reduced surface. This may be due to either the lower temperature or absence of a reducing environment experienced during pretreatment. In

the first case, strongly bound water, or that released only above 200 °C, may have protected the surface oxygens from removal by CO. In the second case, disruption of the support and nickel oxide clusters by hydrogenolysis may have formed bare oxygen functionalities that were susceptible to scavenging by CO. Analysis of a sample pretreated in inert at 500 °C would be suitable to resolve this question.

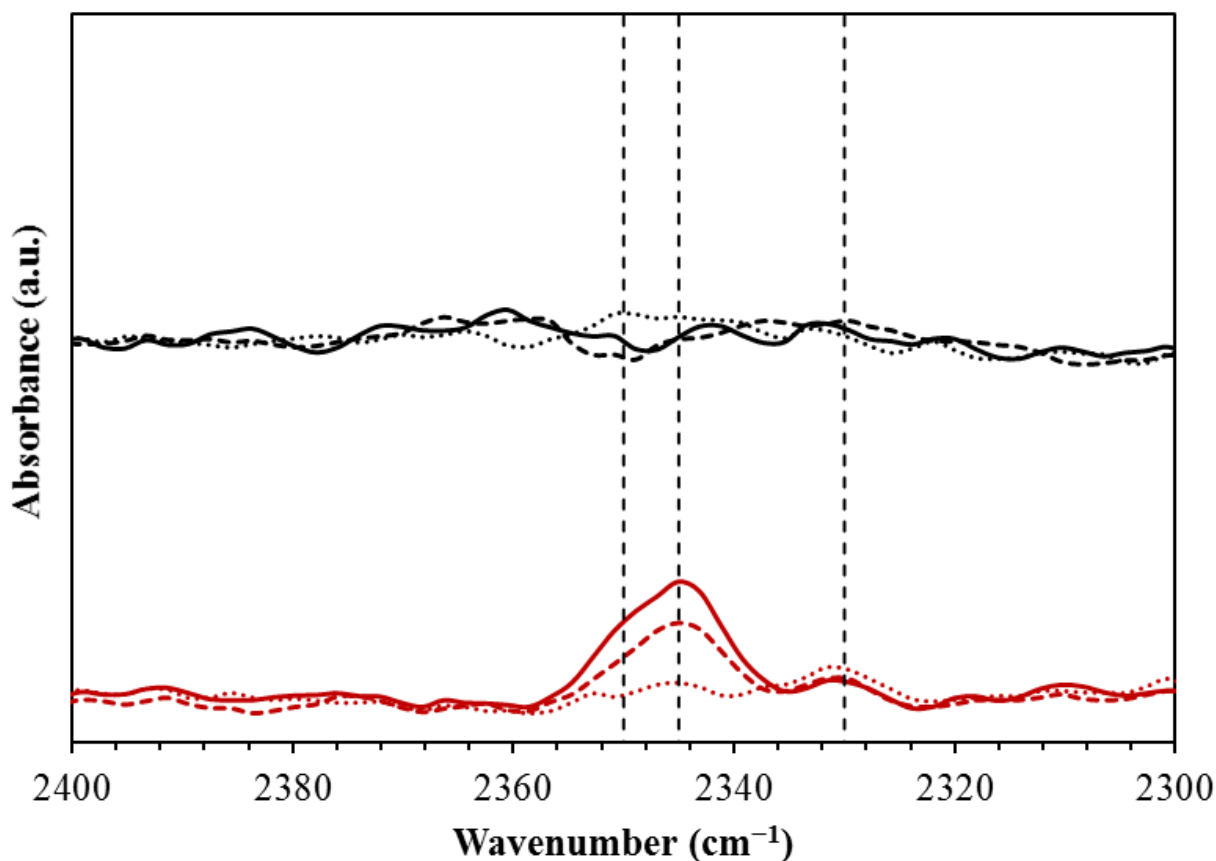


Figure 2.25 Difference spectra of the CO₂ infrared stretching region on activated (black) and reduced (red) Ni/ASA catalyst samples at low (dotted), medium (dashed), and high (solid) degrees of CO saturation at *ca.* -100 °C and low (<100 mbar) total pressure.

CO DRIFTS experiments reveal an abundance of interactions between CO and support functionalities such as aluminum, nickel, silicon, hydroxyl, and oxygen on the catalyst surface.

To complicate interpretation, these features are pressure-dependent, frequently overlapping, and sample specific. Within zeolitic systems, nickel cations are typically identified by CO stretches in the region of 2220 to 2200 cm^{-1} .¹²⁰ These species are further differentiated by mono- and dicarbonyl species, which constitute stretches at 2220 and 2212 cm^{-1} , and 2206 and 2204 cm^{-1} , respectively.⁵⁴⁻⁵⁵ The higher stretching site has been assigned to CO interacting with extraframework Al^{3+} on NiNaY,¹²¹ although this is in contest with the more common assignment of this stretch to 2230 cm^{-1} . In any case, these are likely formed from Ni^{II} in coordination with strong Brønsted acid sites of the zeolite, and resultingly are thought to have low coordination numbers on the order of 3 to 4.¹²²⁻¹²⁵

The coordination of these nickel sites to either one or two CO molecules has been shown to be pressure-dependent, in what have been termed “site-specific” dicarbonyls, or geminal complexes.¹¹² This coordinative flexibility of nickel cations was evidenced as slight decreases in the assigned monocarbonyl peaks while the dicarbonyl peaks grew in at higher CO pressures, and by co-adsorption experiments with NO and carbon 13-labeled CO.⁵⁴⁻⁵⁵ A site-specific geminal complex was described in NiNaY at 2195 and 2187 cm^{-1} , with the lower stretching frequency explained as a lower electrophilicity of nickel due to the incorporation of sodium.¹²¹ Within Na-free Ni-ZSM-5, the conversion of monocarbonyls to dicarbonyls was much more pronounced, due to the greater electrophilicity and coordinative capacity of the sites.¹²⁶ Evidence for the analogous site-specific dicarbonyl in amorphous silica aluminas has not been reported, although there appears no reason for why they could not exist.

Within aluminum-containing BEA samples, intense stretches above 2200 cm^{-1} form at low pressures and are resistant to removal by vacuum, indicating strong interaction.⁵⁴ At higher pressures, these peaks are accompanied by a peak at 2177 cm^{-1} , assigned to aluminols, in

addition to those observed on silica at 2157, 2140, and 2133 cm^{-1} . Nickel-oxide nanoflowers have been reported to interact with CO as high as 2175 cm^{-1} , although background subtraction was not performed to aid visual confirmation of this result.¹²⁷ Bare Siralox 5 (5% SiO_2 , 95% Al_2O_3) showed trace absorbances at 2211 and 2202 cm^{-1} at low pressures, and at higher pressures the 2202 cm^{-1} peak grew in intensity and shifted downward to 2188 cm^{-1} and was accompanied by an additional peak at 2162 cm^{-1} .¹²⁸ Upon incorporation of 5 wt% nickel by impregnation of nickel nitrate, the 2211 cm^{-1} peak was lost, and a peak at 2199 cm^{-1} was found to gain in intensity roughly three-fold relative to the peak at 2202 cm^{-1} on the bare support due to incorporation of cationic nickel.

Bands as high as 2194 cm^{-1} have been reported for nickel well-dispersed on silica, likely as a nickel phyllosilicate layered (2-D) phase. The peak position was observed to shift down to 2184 cm^{-1} at higher CO pressure.¹²⁹ On a nickel-impregnated, aluminum-free BEA zeolite, CO bands absorbed lightly at 2194 cm^{-1} at low CO pressure, followed by growth of an intense peak at 2157 cm^{-1} at high CO pressure assigned to CO hydrogen bonded to surface silanols, and additionally by peaks at 2140 and 2134 cm^{-1} at even higher pressure assigned to CO interacting with surface oxygens.⁵⁴ Nickel oxide nanoparticles (2-5 nm in size) on MCM-41 showed a band at low CO pressure at 2184 with a shoulder at 2176 cm^{-1} . These were assigned to low coordinate, octahedral Ni^{II} cations on the surface of nickel oxide nanoparticles. At high uptake, these bands were accompanied by 2157 cm^{-1} , assigned to silanols. Mihaylov et al. proposed an alternative interpretation of the 2156 cm^{-1} peak observed with nickel on a silica support, wherein a high peak stability and absence of silanol stretch disturbances led to the assignment of undercoordinated nickel ions in nickel oxide.⁵⁵

The downward wander of peak positions as CO pressure increases is an important detail in interpreting peak assignments. Commonly, peak shifts on the order of 10 to 20 cm^{-1} are presented in the literature over the dosing range. It is unclear if these shifts are due to “solvent-effect” interactions between adsorbed CO molecules, changes in the electrostatic potential of the support surface due to charge transfer from CO, or from heterogeneity in the unique support sites. These shifts are not obvious in the present work, nor are they in work on BEA^{54, 48} and ZSM.⁵⁵ They were observed for Ni/SiO₂,¹²⁹ for NiO on pure-silica MCM-41, Ni/Siralox 30, and Ni/Al-MCM-41.⁴⁸ By far, results for zeolitic supports are the most consistent in peak position, and at times show even a slight blue shift upon increasing CO pressure.⁵⁵ Solvent effects may thus differ depending on the support textural properties. For example, CO interacting within a zeolite pore may behave differently than on the less-hindered mesoporous silica surface.

CO interacting with the exchange sites of nickel-free zeolites has shown a strong dependence on the framework, with a peak positions ranging from 2178 cm^{-1} on Na-ZSM-5 to as low as 2163 cm^{-1} on Na-A.¹³⁰ These results were interpreted as differences in the polarizing power of the extraframework cation and the influence of the surrounding negatively charged framework oxygens. In some cases, the presence of multiple binding sites within each zeolite was observed. Mordenite exhibited two main peaks at 2177 and 2160 cm^{-1} that were explained by the presence of exchange sites within the two different channel types present.

Zeolites with high amounts of extraframework aluminum (EFAI) such as USY were shown to exhibit a weak, broad feature at lower CO coverage around 2200 cm^{-1} , attributed to moderately Lewis-acidic Al³⁺, and a shoulder at 2195 cm^{-1} at higher pressures attributed to weakly Lewis-acidic extraframework aluminums.¹¹⁵ The molar absorption coefficients of the

Ni²⁺-CO stretches for nickel-containing zeolites ZSM-5 and Y were found to be nearly equivalent,¹³¹ thus enabling quantification by integration of the relative peak areas.

The band position of adsorbed CO was shown to correlate linearly with the calculated electric strength of alkaline earth metals exchanged on BEA zeolite.¹³² On HBEA, two stretches were observed assigned to Al³⁺ and bridging hydroxyls at 2228 and 2188 cm⁻¹, respectively. Upon incorporation of divalent alkaline earth metals by ion exchange, a strong band was observed that shifted downward from 2210 cm⁻¹ for Mg to 2184 cm⁻¹ for Ba, in line with the expansion in atomic radius.

Table 2.1 constitutes a summary of literature values for CO infrared band assignments.

Table 2.1 Literature values for surface-bound CO infrared peak positions.

Sample	Low coverage bands (cm ⁻¹)	High coverage bands (cm ⁻¹)	Reference
NiSiBEA activated	2194 Ni ²⁺ -CO	2156 SiOH-CO 2140 O _{Surface} -CO 2134 O _{Surface} -CO	Penkova ⁵⁴
NiAlBEA reduced	2234 Al ³⁺ -CO 2214 Ni ²⁺ -CO 2113 Ni ⁺ -CO	2138 Ni ⁺ -(CO) ₂ 2095 Ni ⁺ -(CO) ₂	Penkova ⁵⁴
NiAlBEA activated	2230 Al ³⁺ -CO 2220 Ni ²⁺ -CO 2214 Ni ²⁺ -CO 2177 AlOH-CO	2206 Ni ²⁺ -(CO) ₂ 2174 AlOH-CO 2156 SiOH-CO 2142 O _{Surface} -CO 2133 O _{Surface} -CO	Penkova ⁵⁴
Ni-SiO ₂	2194 Ni ²⁺ -CO	2184 Ni ²⁺ -CO 2157 SiOH-CO	Hadjiivanov ¹²⁹
Ni-ZSM-5	2220 Ni ²⁺ -CO 2212 Ni ²⁺ -CO	2204 Ni ²⁺ -CO 2191 Ni ²⁺ -(CO) ₂ 2174 SiAlO ⁻ H ⁺ -CO 2140 CO _{physisorbed}	Hadjiivanov ⁵⁵
Ni-ZSM-5 reduced	2212 Ni ²⁺ -CO	2136 Ni ⁺ -(CO) ₂	Hadjiivanov ⁵⁵

Table 2.1 Continued

Sample	Low coverage bands (cm^{-1})	High coverage bands (cm^{-1})	Reference
	2109 Ni^+ -CO	2092 Ni^+ -(CO) ₂	
NiNaY	2216 Al^{3+} -CO 2195 Ni^{2+} -CO 2176 Na^+ -CO	2193 Ni^{2+} -(CO) ₂ 2166 Na^+ -(CO) ₂	Mihaylov ¹²¹
Ni-ZSM-5	2220 Ni^{2+} -CO 2212 Ni^{2+} -CO	2170 SiAlO^-H^+ -CO 2155 NiO -CO	Mihaylov ¹²⁶
Ni-ZSM-5	2220 Ni^{2+} _{exchange} -CO 2212 Ni^{2+} _{exchange} -CO 2200 Ni^{2+} _{oxo} -CO 2190 Ni^{2+} _{oxo} -CO		Gora-Marek ¹³¹
γ - Al_2O_3	2235 Al^{3+} _{Td} -CO 2210 Al^{3+} _{Td} -CO	2180 Al^{3+} _{Oh} -CO	Busca ¹³³
NiAl_2O_4	2210 Al^{3+} _{Td} -CO	2190 Al^{3+} _{Oh} -CO 2160 Ni^{2+} -CO	Busca ¹³³
NiO		2160 NiO -CO	Busca ¹³³
Siralox 5 (5% SiO_2 , 95% Al_2O_3)	2211 Al^{3+} -CO 2202 Al^{3+} -CO	2188 Al^{3+} -CO 2162 SiOH -CO	Garbarino ¹²⁸
Ni-Siralox 5 (5% SiO_2 , 95% Al_2O_3)	2199 Ni^{2+} -CO	2185 $\text{Al}^{3+}/\text{Ni}^{2+}$ -CO 2158 SiOH -CO	Garbarino ¹²⁸
Na-ZSM-5		2178 SiAlO^-H^+ -CO	Bordiga ¹³⁰
Silica alumina (25 wt% Al_2O_3)	2231 Al^{3+} -CO 2200 Al^{3+} -CO 2175 SiAlOH -CO	2195 Al^{3+} _{EFAI} -CO 2170 SiAlO^-H^+ -CO 2157 SiOH -CO	Cairon ¹¹⁵
SiO_2		2158 SiOH -CO 2140 $\text{CO}_{\text{solvent-like}}$	Beebe ¹³⁴
NiO-MCM-41	2184 NiO_{nano} -CO 2176 NiO_{nano} -CO	2157 SiOH -CO	Moussa ⁴⁸
Mg-, Ca-, Sr-, Ba-BEA	2228 Al^{3+} -CO	2188 SiAlO^-H^+ -CO 2210 Mg^{2+} -CO 2195 Ca^{2+} -CO 2190 Sr^{2+} -CO 2184 Ba^{2+} -CO	Li ¹³²

The infrared stretching region of surface-bound CO (2240 to 2050 cm^{-1}) of the activated (plotted in black) and reduced (plotted in red) Ni/ASA samples are shown in Figure 2.26 for varying levels of CO exposure. Three trace peaks were observed on the pretreated sample at high stretching frequencies of 2240, 2230, and 2222 cm^{-1} . These features have been assigned to undercoordinated tetrahedral Al^{3+} , based on experiments with nickel-doped $\gamma\text{-Al}_2\text{O}_3$.¹³³ Two main features developed at low CO pressure at 2206 and 2196 cm^{-1} . These were assigned to Ni^{II} cations associated with moderate and weak Lewis acid sites, respectively. Namely, these represent low coordinate aluminums, potentially as 5- and 6-coordinate species.

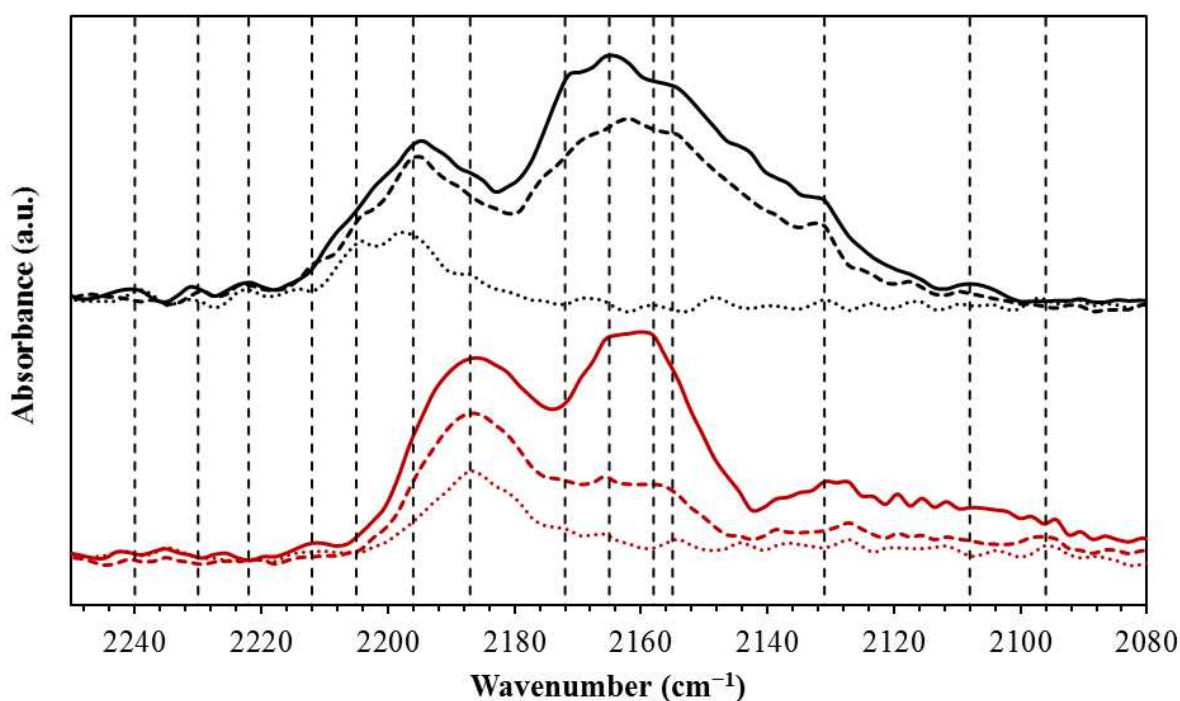


Figure 2.26 Difference spectra of CO infrared stretching region on activated (black) and reduced (red) Ni/ASA catalyst samples at low (dotted), medium (dashed), and high (solid) degrees of CO saturation at *ca.* $-100\text{ }^{\circ}\text{C}$ and low ($<100\text{ mbar}$) total pressure.

At higher pressures, the peak at 2196 cm^{-1} intensified and was accompanied by trace peaks at 2212 and 2187 cm^{-1} that were assigned to tetrahedral and octahedral aluminum, respectively.¹³³ Several strong overlapping peaks also developed at 2172 , 2165 , and 2155 cm^{-1} that were assigned to bridging hydroxyls (Brønsted sites), octahedral nickel in coordination with alumina, and silanols, respectively. Fine features at 2131 and 2108 cm^{-1} were from surface oxygens, and potentially trace Ni^I. Following saturation, the sample was exposed to vacuum, after which the peaks at 2206 , 2196 , and 2187 cm^{-1} remained in relative intensities similar to the initial dosing (not shown). This result confirmed the high stability of these species demonstrated in work by Moussa et al. on Ni/ASA.⁴⁸

Owing to the resemblance of these strongly-interacting peaks to those observed in zeolitic systems, the peaks at 2206 and 2196 cm^{-1} are potentially a complex-specified, geminal pair. No direct evidence of interconversion was observed here, although subtle fluctuations in stretches between 2215 and 2190 cm^{-1} as the CO coverage increased may allude to this possibility. A modification of the experimental procedure to first saturate the sample with CO at ambient pressure and then record the observed changes under dynamic vacuum may enable sufficiently small steps to enable these observations, although co-adsorption experiments with NO or carbon ¹³-labeled CO appear to offer more concrete determination of geminal ligand adsorption in the literature.

Upon reduction, a substantial restructuring of the band intensities occurred. The peaks at 2205 and 2196 cm^{-1} were diminished strongly, the peak at 2172 cm^{-1} diminished moderately, and the peak at 2187 cm^{-1} grew. This suggests a selective loss of the most strongly Lewis acid nickel sites, and a relative increase in the contribution by octahedral aluminum (2187 cm^{-1}) and octahedral nickel coordinated with alumina (2165 cm^{-1}). The peaks at 2212 , 2158 , and 2131

cm⁻¹ were unaffected. A broad tailing in the region from 2140 to 2090 cm⁻¹ also appeared, indicative of trace Ni^I.⁵⁵

Adsorption of CO on silica and aluminosilicates can be expected to perturb terminal silanols (3750 cm⁻¹) and strongly and weakly acidic hydroxyls (3600 and 3525 cm⁻¹) by loss of these peaks and the appearance of associated peaks at red-shifted values between 3500 and 3200 cm⁻¹.^{115, 134} These interactions are accompanied by the corresponding CO stretch in the region of 2200 to 2150 cm⁻¹.

Literature values for surface hydroxyl infrared peak positions are shown in Table 3.3.

Table 2.2 Literature values for surface hydroxyl infrared peak positions.

Sample	Pretreatment temperature (°C)	Band position (cm ⁻¹)	Reference
γ -Al ₂ O ₃ , NiAl ₂ O ₄	200	3790 IVAl-OH 3770 IVAl-OH 3730 VIAl-OH 3680 (Al) ₂ -OH	Busca ¹³³
	400	3580 (Al) ₃ -OH	
NiO	400	3680 Ni-OH	Busca ¹³³
	200	3690 Ni-OH 3600 (Ni) ₂ -OH	
NiO	500, vacuum	3735 NiOH 3690 (Ni) ₃ -OH 3630 (Ni) ₄ -OH	Tsyganenko ¹³⁵
H-ZSM-5	500, vacuum	3740 SiOH 3610 SiAlO ⁻ H ⁺	Mihaylov ¹²⁶
Ni(OH) ₂		3641 3577	Kermarec ¹³⁶
ZSM-5		3745 Si-OH _{isolated} 3735 Si-OH _{internal, perturbed} 3726 Si-OH _{internal, perturbed} 3700 Si-OH _{internal, perturbed}	Svelle ¹³⁷

The difference spectra of the hydroxyl region of the activated and reduced Ni/ASA are shown in Figure 2.27. A decrease in the terminal hydroxyl stretch at 3748 cm^{-1} was observed immediately at low dosing pressures on the activated sample. Without a strong SiOH-CO stretch to coincide with the loss of SiOH intensity, it is interpreted that interactions between CO and the Ni^{II} cations had involved participation of adjacent silanols. At this pressure, the peak corresponding to terminal silanols at 2158 cm^{-1} was trace, and further experiments to determine quantitatively the relative interaction of silanol stretch to CO stretch should be performed.

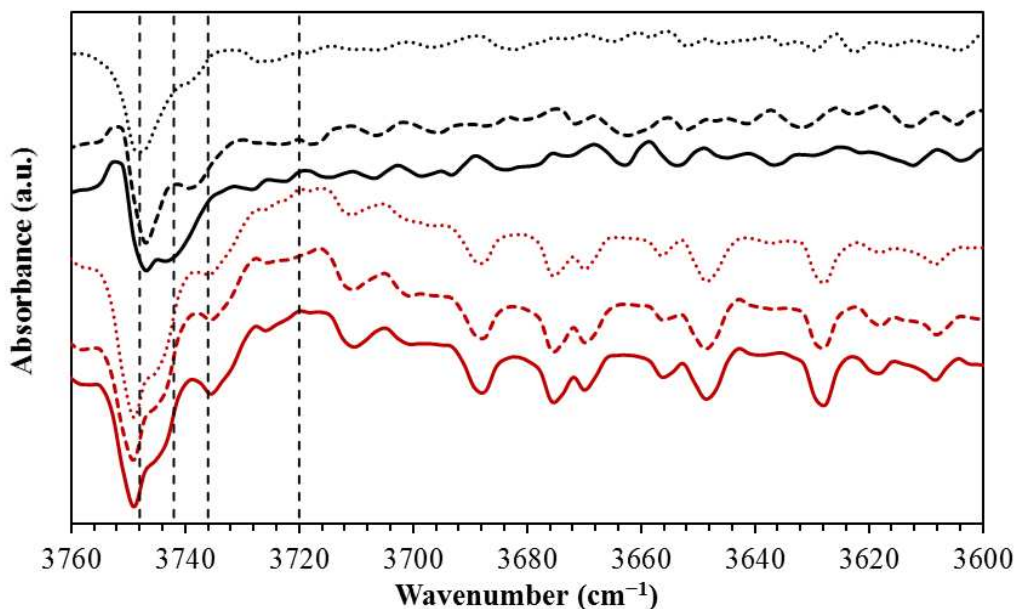


Figure 2.27 Difference spectra of hydroxyl infrared stretching region on activated (black) and reduced (red) Ni/ASA catalyst samples at low (dotted), medium (dashed), and high (solid) degrees of CO saturation at *ca.* $-100\text{ }^{\circ}\text{C}$ and low ($<100\text{ mbar}$) total pressure.

At higher pressures, a shoulder appeared at 3742 cm^{-1} that corresponded with increases in the CO stretching region of bridging hydroxyls, silanols, and bulk nickel oxide. This stretch is hypothesized to consist of a terminal silanol that experiences weak hydrogen bonding to an adjacent hydroxyl. In chains of terminal silanols, stretches are reported to 3720 and 3715 cm^{-1}

for inner chain and terminal hydroxyl species, respectively.¹⁰³ The stretch of 3740 cm^{-1} is intermediate of the isolated and chained silanol stretches, which suggests that the non-silanol hydroxyl is less polar. Such a species may be a hydroxyl or water on a 6-coordinate Al, or a Ni-OH-type species.

On ZSM-5, isolated surface hydroxyls appear at 3745 cm^{-1} , while weakly perturbed, internal silanols (or silanol defects) are assigned at 3735 , 3726 , and 3700 cm^{-1} .¹³⁷⁻¹³⁸ The disappearance of these stretches upon CO exposure was shown to coincide with the formation of CO stretches at 2175 , 2170 , and 2157 cm^{-1} corresponding to CO interacting with bridging hydroxyls and surface silanols.¹³⁸ The appearance of a high-frequency shoulder at 3753 cm^{-1} is a result of cooling of the sample due to CO improving the thermal contact of the sample with the chamber.¹⁰³

On the reduced sample, the diminished terminal silanol stretch appeared at a slightly higher frequency of 3750 cm^{-1} with a shoulder at 3736 cm^{-1} . Unlike the activated sample, further increases in the CO coverage did not result in changes to the peak shape. A positive band at 3720 to 3715 cm^{-1} is assigned to silanols that are hydrogen-bonded in a chain fashion.¹⁰³ For both the activated and reduced samples, no perturbations to the hydroxyl region beyond 3680 cm^{-1} were observed that would correspond to interactions with acidic hydroxyls, nor was the associated peak for perturbed hydroxyls observed between 3700 and 3500 cm^{-1} . Repeat experiments may be performed to conclude the validity of these results.

2.4 Discussion

Moussa et al. presented strong evidence that nickel cations having moderate electrophilicity present on ASAs are as active, and potentially even more active for ethylene oligomerization than those having higher electrophilicity on supports such as Al-MCM-41 and

zeolite BEA.⁴⁸ The rationale for this performance was a moderation of the interaction strength between the catalyst and the reactants and products. The deactivation of oligomerization catalysts by the accrual of heavy oligomer products is well known, and the desorption of oligomeric alkoxides is thought to be the rate-limiting step in achieving high turn-over frequencies.¹³⁹⁻¹⁴⁰ These results are conflicted by the understanding that increased acid strength will in general result in a more active catalyst.⁷⁸ However, an increased acidity in supports is correlated with an enhanced dispersion of the active nickel phase,¹³¹ and may subsequently be necessary to avoid the agglomeration of nickel in bulk oxide-type phases.

The oligomerization of olefins by nickel is thought to proceed by the Cossee-Arlman mechanism¹⁴¹⁻¹⁴⁴ in both homogenous and heterogenous forms,^{43, 51} in which the ability for nickel to form at least two vacancies is a prerequisite for catalytic activity. Stepwise, initiation begins with coordination to the first ethylene (one site), then transition to an agostic ethyl species (two sites), followed by addition of a second ethylene (two sites), and finally migratory insertion of ethylene to form an agostic butyl species (two sites). This butyl species can then be displaced by β -hydride transfer to monomer (ethylene) to desorb butene and form the agostic ethyl species, thought to be the resting state of the catalysts.⁴³ This vacancy requirement rules out statically 6- and 5-coordinate nickel sites, but allows for 5-coordinate sites where one ligand is hemilabile (pseudo 4-coordinate, in a sense), 4-coordinate sites, 4-coordinate sites where one or more ligands are hemilabile, and 3- and 2-coordinate sites. The proposed 5-coordinate active site is shown in Figure 2.28.

Nickel upon zeolitic exchange sites has been thought to produce coordination numbers below five, owing to the strong electrostatic stabilization offered by the framework oxygens.¹⁴⁵ Within supports having weaker acidity, this coordination is less defined, but the lower

electrophilicity for nickel on ASA determined by CO-DRIFTS suggests a coordination intermediate that of zeolites and bulk nickel oxide. These sites have been described in the literature as nickel coordinated with weaker acid sites such as aluminols and silanols,⁴⁸ and so-called “oxo-type” species that form on aluminum-poor zeolites.¹³¹ It should be noted, that “oxo-type” nickel species is a descriptor used by the authors for the oxide-type structure of nickel on these supports having low acidity. In other words, these species are not atomically dispersed as ions and contain some Ni-O-Ni bonds.

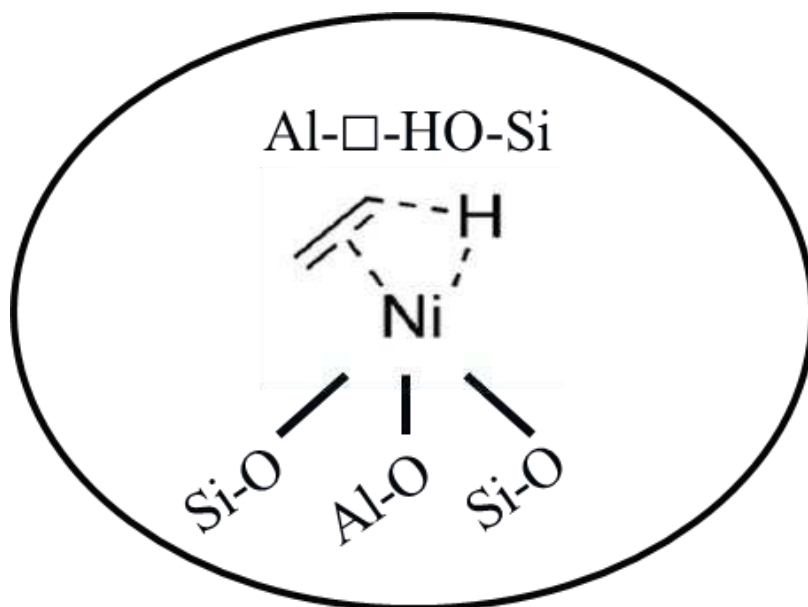


Figure 2.28 Proposed active site structure for nickel catalysts involving hemilabile function of adjacent aluminum and terminal silanols.

The synthesis of active catalysts is thus a balance of competing factors, where strong acid sites aid in the formation of well-dispersed, low coordinate nickel species, while the desorption of oligomeric products bound as alkoxides to these acid sites becomes rate limiting during reaction. To further complicate interpretation, acid sites enable the coupling of C₃₊ olefins through hetero-oligomerization, and consequently improve the yield of heavy products. Efforts

to mitigate the accrual of products have led to the application of mesoporous and non-microporous materials such as mesoporous silica-aluminas and ASAs to produce the most active, supported heterogeneous nickel catalysts known to date,³⁸ perhaps excluding supported nickel complexes and nickel-containing metalo-organo framework-type (MOF) structures. In contrast to zeolites, these supports possess moderate acid strengths and more diverse coordinative environments. This implores the exploration of hierarchical mesoporous and nanosheet structured zeolites as carriers for nickel, and to investigate the highly electrophilic nickel sites in a less diffusion-limited environment.

It seems fitting to consider these intermediately electrophilic nickel sites as potentially 5-coordinate. By matching the pre-edge features of active catalysts to model nickel compounds in XAS, it was shown that the more active materials displayed lower coordination numbers of at least five, while the less active materials were closer to 6-coordinate. The absence of a second pre-edge peak suggested these materials did not possess square planar or square pyramidal geometries and were thus distorted square pyramidal or trigonal bipyramidal in geometry. The average Ni-O distance fitted from EXAFS was 2.02 to 2.04 Å, below that of 5-coordinate KNiPO₄. Data has been reported in literature where Ni(Cp)₂ deposited on ASA exhibited a pre-edge peak at 8333.7 eV and an average Ni-O distance of 2.06 Å before and after exposure to ethylene, which would suggest a coordination between 5 and 6.⁷⁴

A 5-coordinate nickel would not have the coordinative vacancy to form an additional two bonds with olefins during oligomerization. It is hypothesized that the bonding environment of the support plays a hemilabile role and releases the nickel to coordinate with gas phase olefin ligands under reaction conditions. The flexible coordination observed in aluminum in ASAs, also suspected to be the origin of their acidity through pseudo-bridging silanols, may be involved in

the stabilization of this hemilabile, 5-coordinate nickel species. The silyl oxonium structure described by Jystad et al. for zirconium in ASA¹¹⁸ is remarkably similar to this proposed structure, in that Lewis-acidic metal centers were weakly coordinated by an adjacent silanol which became acidified by the interaction. However, it was found in large cluster calculations that Zr preferred a framework tetrahedral coordination, e.g. a Zr-(OSi)₄-type structure. The other examined metals, W and Nb, are on the other side of the “oxo wall”¹⁴⁶ from Zr and Ni, and consequently behaved differently due to the formation of M=O oxo species. Upon coordination with ammonia, a strong base, the silyl oxonium hydroxyl was deprotonated and the resulting charged ammonium species became stabilized by the surrounding support. In some cases, condensation between the metal and the silyl oxonium occurred, whereby a metal hydroxyl was protonated and removed as water and a M-O-Si bond was formed.

Within zeolites, the stabilization of the protonated intermediates and colliding olefins by the surrounding anionic framework oxygens through van der Waals interactions plays a very important role in promoting the purely acid-catalyzed oligomerization pathway.¹⁴⁷ The coordinative chemistry achieved by nickel on heterogeneous supports may also be stabilized in this manner. Analogously, co-catalysts in homogeneous olefin oligomerization are thought to stabilize the working homogeneous nickel complex.³⁹

The disappearance of silanol stretches in CO-DRIFTS experiments prior to the direct observation of CO interacting strongly with silanols is explained as evidence that as the CO-ligated nickel releases slightly from the support pocket, adjacent silanols become drawn to the coordinative vacancy of the support or are involved in the stabilization of the mobilized nickel cation. CO and ethylene are known to bind competitively with nickel,^{48, 117} and may thus play a similar role in mobilizing the cation, extending the implications of this observation to olefin

oligomerization. The ligand-enabled mobilization of nickel from small pore pockets to more open environments has been reported in zeolites for ligands such as propylene and water.^{75, 148} However, the resulting effect on the neighboring support structure is not well understood, especially for ASAs.

2.5 Conclusions

Ni/ASA catalysts are highly active for the oligomerization of ethylene. However, understanding about the nature of their active sites is impeded by the heterogeneity of the support structure and of the resulting nickel environment. Upon incorporation by ion exchange, nickel interacted strongly with the aluminum of the support as evidenced by redistribution of aluminum to increase the concentration of 5-coordinate sites and the formation of nickel species having reduction events at temperatures above that of bulk nickel oxide and being comparable to nickel phyllosilicates and nickel on alumina. The electrophilicity of nickel cations, as probed by interaction with CO, appears intermediate to those formed in zeolites and bulk nickel oxide. Based on pre-edge information and average Ni-O distances obtained from XAS experiments, these nickel species were proposed to be 5-coordinate in nature, in accord with their intermediate electrophilicity. The coordination number of the activated nickel catalysts is unchanged by ethylene exposure, as observed by *in situ* XAS experiments. However, pronounced fluctuations in the EXAFS fits upon ethylene exposure as well as interactions between terminal silanols and cationic nickel species upon CO exposure suggest a local restructuring of the nickel environment in response to binding ligands. The above observations are concluded as evidence of a hemilabile interaction between the nickel cations and the support, whereby weak to moderate nickel-support bonds become displaced by strongly-coordinating reactants.

These results further our understanding of the nature of ASAs and their interactions with transition metal cations under working environments and expand upon the description of their pliable coordinative nature. Further work in this area is needed to better define active sites in terms of single site catalysis through *in situ* and *operando* methods that characterize catalysts as they respond to and are modified by the surrounding reaction conditions.

2.6 Acknowledgements

This work was supported by the Department of Energy's Bioenergy Technology Office under Contract no. DE-AC36-08-GO28308. Dr. Singfoong Cheah, Dr. Guanghui Zhang, and Dr. Jeff Miller are thanked for XAS experiments.

CHAPTER 3

THE OLIGOMERIZATION OF LIGHT OLEFINS

3.1 Introduction

The oligomerization of light olefins is a potential route to gasoline and distillate range hydrocarbons from biomass utilizing existing syngas (CO and H₂) to olefin technologies. Well-known examples of processes offering access to these compounds from gasified biomass are the methanol-to-olefins process (MTO) and Fischer-Tropsch. An alternate route has been explored by NREL with the conversion of syngas to a mixture of alcohols, being primarily ethanol.³⁰ More recently, NREL has investigated catalytic dehydration of these alcohols to light olefins, namely ethylene and propylene, in order to access subsequent oligomerization to gasoline and distillate range (C₄-C₁₄) molecules.³³ The performance of Zr-KIT-6 was compared to three commercially available catalysts for alcohol dehydration in collaboration with the University of Kansas. From this comparison, SAPO-34 was identified as the most promising material based on the metrics of selectivity, activity, and commercial availability. The dehydration products consisted mainly of a mixture of ethylene and propylene in a 2.8 to 1 ratio. The oligomerization and hydrogenation of these light olefins could provide drop-in substitutes for gasoline and diesel fuels from biomass.

The research goal was (1) to oligomerize a mixture of light olefins that was representative of a dehydrated mixed alcohol stream using one commercial catalyst and at least one novel catalyst and (2) to study catalyst support effects in the oligomerization of a pure ethylene feed. Nickel supported on acidic solids are the best known heterogeneous catalysts for ethylene

oligomerization.^{38, 149} The mechanism of dimerization and isomerization of ethylene over a nickel complex is shown in Figure 3.1, reproduced from de Souza et al.¹⁵⁰ In this mechanism, a supported nickel cation acts catalytically through interaction with ethylene's π -electrons to coordinate a π -bonded ethylene species. Subsequent coordination and insertion of an additional ethylene results in the formation of butene and higher olefins. Termination occurs by desorption of the formed oligomer.

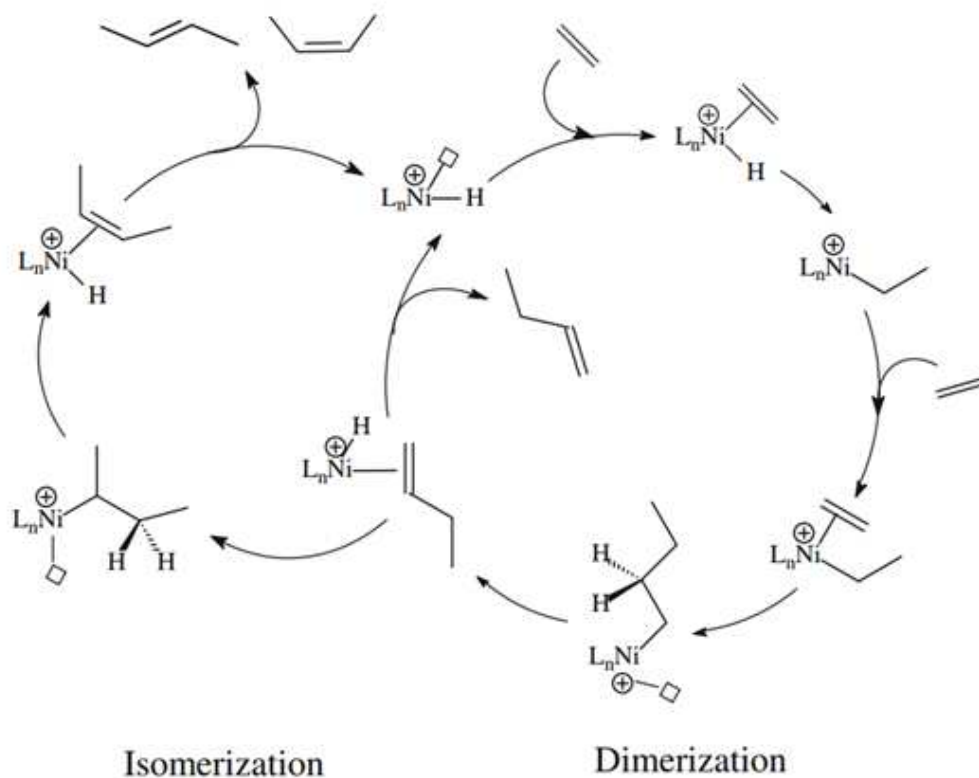


Figure 3.1 Schematic catalytic cycle of ethylene dimerization and 1-butene isomerization. Reproduced from de Souza et al.¹⁵⁰

Owing to the nature of the nickel-ethylene interaction, the electron density of nickel plays a key factor in the relative rates of coordination, insertion, and termination. The choice of support is expected to thus modify the electron affinity of nickel and consequently influence

catalytic properties. The importance of support Brønsted acidity in the formation of active nickel catalysts has been understood for some time.^{37, 53, 76} More recently, supports with moderately strong Brønsted and Lewis acid sites such as amorphous silica-alumina and mesoporous silica-alumina have been shown to produce more active nickel sites than those formed on strongly Brønsted acidic zeolite BEA.⁴⁸ The exact mechanism by which these moderated and mixed acid functionalites promoted nickel was not determined, although it was argued that nickel found interaction with the weakly acidic silanols and aluminols of the silica-aluminas. These results motivated this work to study nickel activity as a function of support electron donor/acceptor properties, to explore supports outside the bounds of solely Brønsted acid functionality, and to focus efforts on silica-alumina-type materials over zeolites.

A survey of the catalytic properties of two dozen commercially-available support materials comprising carbons, oxides, and zeolites in previous NREL work¹⁵¹ guided support down-selection to anatase TiO₂ and MgO as Lewis acidic and solid basic supports, respectively. To represent silica-alumina, a review of recent oligomerization patent literature led to the selection of a commercial silica-alumina, Davicat-3125, where 25 denotes the composition of alumina content of 25 wt.%, from a patent by Synfuels.¹⁵² An additional silica-alumina, Davicat 3115 (15 wt.% Al₂O₃) was tested to study the effect of aluminum content and speciation. The Davicat materials will be referred to as ASA₂₅ and ASA₁₅ in the following text.

To consider the industrial relevance of these catalysts through economic arguments, a cursory estimate of finished catalyst cost by support type was made using an internal NREL Excel-based catalyst cost estimation tool.

3.2 Methods and Materials

The materials and methods used in this work are given in the following subsections.

3.2.1 Catalyst Synthesis

Ni/ASA₂₅ was prepared by adding the powdered support (Davicat 3125, Grace Davidson) to an aqueous solution of 0.22 M Ni(NO₃)₂•6H₂O at a ratio of 3 mL per gram support, followed by heating under reflux for 4 h. After cooling to room temperature, the catalyst was filtered, rinsed with 100 mL of water per gram catalyst, and dried overnight under vacuum at 100 °C. The nominal nickel content of the finished catalyst was 2 wt% based on literature procedures.¹⁵² For MgO (Sigma Aldrich) and TiO₂ (P90, Sigma Aldrich), the volume of water per gram of support required to reach the incipient wetness point was determined. A predetermined volume of an aqueous solution of Ni(NO₃)₂•6H₂O was then delivered onto the dry supports (Sigma-Aldrich) to deliver a nominal nickel loading of 2 wt.%. The samples were then dried overnight under ambient conditions. The nickel-containing catalyst precursors were calcined in air at 550 °C for 5 h with a ramp rate of 3 °C/min prior to further characterization.

3.2.2 Catalyst Characterization

Nitrogen physisorption was performed on a Micromeritics ASAP 2020 at -196 °C. Surface area was determined by Brunauer-Emmett-Teller (BET) analysis over the P/P₀ range of 0.05-0.30. Pore size was calculated using the desorption branch of the isotherm. The pore volume was determined by the volume of N₂ uptake at P/P₀ = 0.99.

Powder X-ray diffraction (XRD) was performed on a Rigaku Ultima IV X-ray diffractometer using Cu-K α radiation at 40 kV and 44 mA. Samples were scanned at 2° 2 θ /min with a resolution of 0.02° over a range of 10° to 80° 2 θ . Spectra were compared to the reference card file for NiO (ICDD 04-002-0665) from the International Center for Diffraction Data.

Solid state Magic Angle Spinning (MAS) NMR was performed using a Bruker Avance III spectrometer equipped with a 14.1T magnet (²⁷Al operating frequency of 156.38MHz.), a

2.5mm MAS probe, and Topspin 3.0 for data acquisition and processing. The powdered samples were packed directly into 2.5mm zirconia rotors with Valspar caps. Samples were collected at room temperature, with MAS=25kHz, and using a one pulse experiment with a 30° tip angle (0.5 sec). Spectra were acquired with a delay time of 0.5sec and 50k scans. Prior to analysis, the powdered samples were dried overnight at 200 °C in air.

Samples were prepared for X-ray photoelectron spectroscopy (XPS) analysis by pressing the catalyst powders onto nonconductive double-sided tape and arranging them on a multisample plate, which was subsequently loaded into a Kratos Nova XPS instrument. X-rays were supplied by a monochromatic Al K source operated at 300 W. High-resolution spectra were collected for carbon (C 1s), oxygen (O 1s), and nickel (Ni 2p_{3/2}) at an analyzer pass energy of 20 eV, while providing charge neutralization. Data analysis was performed using CasaXPS software. A linear background was applied to C 1s and O 1s spectra, and a Shirley background was applied to Ni 2p_{3/2} spectra. The spectra were calibrated by setting the O 1s peak maximum to 284.8 eV for adventitious carbon.

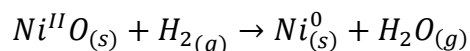
The relative amounts of Brønsted and Lewis acid sites were determined using pyridine adsorption diffuse-reflectance FT-IR spectroscopy (Py-DRIFTS). Spectra were recorded at a resolution of 4 cm⁻¹ on a Thermo Nicolet iS50 FT-IR spectrometer equipped with a Harrick Praying Mantis high temperature reaction chamber and CaF windows. Samples were loaded into the chamber and pretreated in flowing N₂ (100 mL/min) at 200 °C for 3 h. After cooling to 150 °C, samples were purged with N₂ for 0.5 h, and pyridine vapor was introduced. After 5 min of pyridine exposure, the samples were heated to 200 °C and held for 1 h under flowing N₂ to remove excess and/or physisorbed pyridine. The adsorption bands near 1454 cm⁻¹ (Lewis) and

1545 cm⁻¹ (Brønsted)⁸¹ and their relative adsorption coefficients ($\epsilon_B/\epsilon_L = 0.76$)⁸² were used to determine the relative Brønsted/Lewis acidic site ratios.

The density and strength distribution of acidic sites on the Ni-containing catalysts were characterized by the temperature-programmed desorption of ammonia (NH₃ TPD). Samples were pretreated, dosed, and analyzed under flowing conditions (50 mL/min, ambient pressure) in a Micromeritics Autochem II 2920 chemisorption instrument. After being dried at 100 °C for 1 h and pretreated at 500 °C for 2 h, the samples were exposed to a blend of 10% NH₃/He for 1 h at a temperature of 120 °C. The samples were purged with He for 1.5 h, then ramped to 500 °C at 30 °C/min and held for 1 h. Changes in outlet concentrations were monitored by a downstream thermal conductivity detector (TCD).

Scanning electron microscopy (SEM) was performed on an Evex Mini-SEM SX-3000 at an accelerating voltage of 20 keV. Powdered samples were affixed to the sample post by a piece of double-sided tape and then sputtered with gold to reduce charging.

The total nickel content of the finished catalyst was determined by elemental analysis (EA) performed by Galbraith Laboratories (Knoxville, TN). Temperature-programmed reduction (TPR) performed in a Micromeritics Autochem II 2920 chemisorption instrument was used to determine the amount of nickel oxide present. Samples were purged at 120 °C for 1 h in flowing Ar, and then ramped from 40 °C to 900 °C at 10 °C/min in 10% H₂/Ar. The quantity of hydrogen uptake was determined by integration of the main reduction event peak between 350 and 750 °C. The quantity of nickel oxide was related to hydrogen uptake with the following stoichiometry:



3.2.3 Reaction Testing

Continuous flow reactions were performed in a 20 cm³ packed bed reactor which supported an isothermal catalyst bed zone of 4.9 cm³. The catalyst bed was suspended within the isothermal zone of the reactor by a layer of coarse (40-50 mesh) and fine (60-100 mesh) quartz chips and contained at the reactor tube inlet and outlet by quartz wool frits. Prior to loading, a thermocouple probe was inserted directly into the center of the catalyst bed for temperature measurements. The catalysts were pretreated at 200 °C for 3 h under carbon-filtered house nitrogen at 50 g/h prior to olefin exposure.

Two feeds were utilized to study separately the activity of catalysts for ethylene conversion and to determine the impact of a mixed olefin feed representative of those obtained by the dehydration of mixed alcohols. These feeds consisted of 95% ethylene/Ar and a mixture of 70% ethylene and 25% propylene, balance Ar, respectively, and were supplied by General Air. The reactants were fed to the reactor *via* a thermal mass flow controller, and a back-pressure regulator at the outlet of the reactor was used to control reactor pressure. Ethylene experiments were performed at total pressures in the range of 200 to 500 psig, while the ethylene/propylene mixed feed experiments were performed at lower total pressures (~200 psig) due to the lower vapor pressure of propylene (9 bars for propylene at 15 °C versus 41 bars for ethylene) and consequently lower tank pressure.¹⁵³

The rate of oligomerization is known to increase with olefin pressure,³⁷⁻³⁸ and consequently the highest pressure that could be obtained given the delivered tank pressure (~500 psig for ethylene, ~250 psig for ethylene/propylene mixture) was used. A reactor temperature of 120 °C was employed for all experiments, as this temperature is used widely in the literature due to it being recognized as the optimum for many heterogeneous nickel catalyst systems.³⁸ The

outlet path from the reactor was heated by insulated heat trace lines to 200 °C to prevent condensation of products while en-route to an on-line gas chromatograph (GC) for analysis.

The conversion of olefins and production of oligomers were analyzed on-stream with an Agilent 7890A gas chromatograph (GC). The system utilized separate columns for the analysis of C₂-C₇ light hydrocarbons (Wasson ECE KC5 column, 50 m, 530 μm diameter) and C₈₊ heavy compounds (Wasson ECE KC1 column, 60 m, 320 μm diameter). Ethylene and Ar concentrations were measured by a thermal conductivity detector. The concentration of propylene and higher weight products were measured by a flame ionization detector (FID). The identity of products was determined by a combination of mass spectrometry to identify likely species present in the reactor effluent and by the manual injection of standard compounds to confirm residence times. The FID response factor (RF) for each analyte was determined by the manual injection of known concentrations of standard compounds.

Due to the large numbers of product isomers in the reactor effluent stream and the lack of individual standard compounds for each unique isomer, the RF values for isomers having the same carbon number were approximated to be equal. Ar concentration was used as an internal standard to determine the flow rate of reactor effluent. Heavy reaction products were condensed downstream of the on-line GC sampling port in a knockout pot kept at ~0 °C by an external glycol chiller loop and quantified separately by GC analysis (Agilent DB-5 column). Typically, liquid products in the C₅-C₁₄ range were collected in this manner, although sample yields were highly variable through combination of product retention in the catalyst bed, operating conditions, and differences in catalytic activity.

The conversion of olefins (X), carbon number selectivity of products (S), and catalytic productivity were calculated as follows:

$$\text{Conversion (X)} = \frac{\text{Moles ethylene or propylene consumed}}{\text{Moles olefin fed}}$$

$$\text{Selectivity (S)} = \frac{\text{Moles oligomers per carbon number formed}}{\text{Total oligomers formed}}$$

$$\text{Productivity} = \frac{\text{Moles oligomers formed}}{\text{catalyst mass * hour}}$$

For productivity values, the rate of oligomer product yield was estimated as the sum of the outlet flow rate of C₄-C₇ products as measured by on-line GC analysis and the time-averaged liquid sample yield. The on-line conversion and productivity of catalysts were compared at 5 h time-on-stream (TOS). The time-averaged liquid sample yield was the mass of liquid sample obtained at the end of the experiment divided by the duration of olefin exposure (typically 6-8 hours).

3.2.4 Catalyst Cost Estimates

The finished catalyst costs of several Ni-containing catalysts were estimated using an NREL-developed Excel toolbox. Material estimates were based on power-law extrapolation of prices from chemical vendors (e.g. Sigma Aldrich) to a bulk purchase scale of 5,000 pounds and processing cost estimates based on a 1,000,000 pound per year production scale. Prices were calculated in 2015 dollars. Al-MCM-41 is regarded as an effective support for oligomerization³⁸ and was included in the cost analysis to compare to the Davicat and metal oxide supports.

3.3 Results

The results of this chapter are shown in the following subsections.

3.3.1 Support Study Characterization

The BET surface and acid site densities for the catalyst supports are given in Table 3.1.

Table 3.1 Surface area and acidic properties of ASA₂₅, TiO₂, and MgO supports.

Support	BET surface area (m ² g ⁻¹)	Brønsted sites ^a (μmol g ⁻¹)	Lewis sites ^a (μmol g ⁻¹)
ASA ₂₅	541	249	445
TiO ₂	151	0	250
MgO	78	N/A	N/A

^aDetermined by NH₃ TPD and pyridine DRIFTS.

The three supported-Ni materials were investigated for the presence of Ni-oxides and metallic Ni using XRD (Figure 3.2).

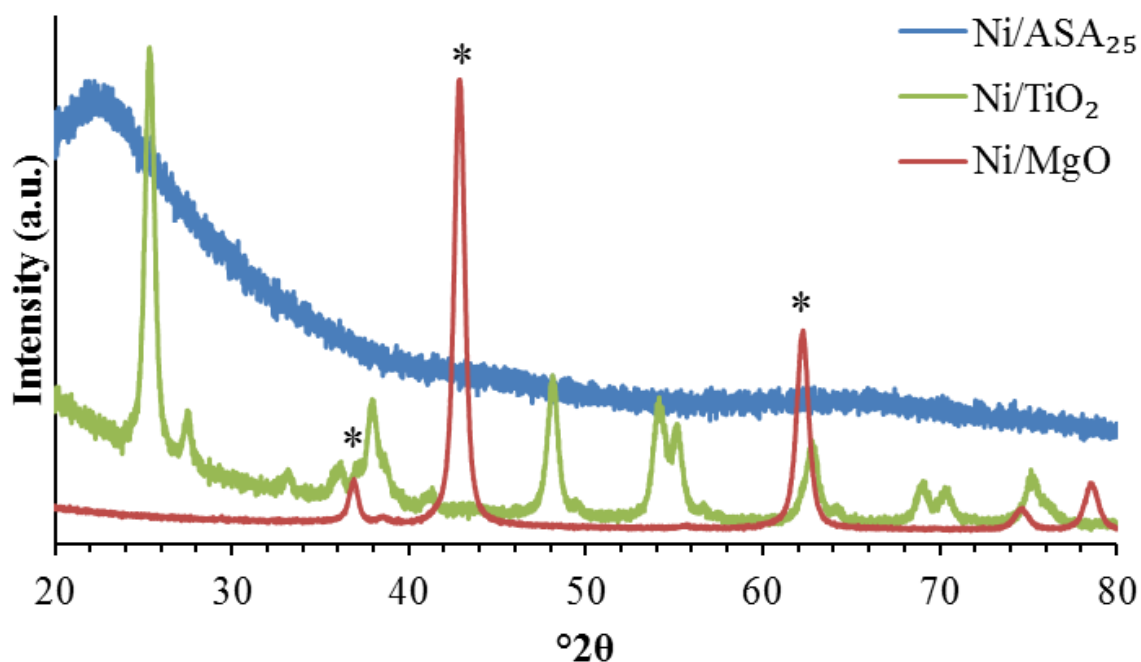


Figure 3.2 X-ray diffraction patterns of nickel supported on ASA₂₅, MgO, and TiO₂ supports. The peak position of the NiO and MgO (111), (200), and (220) facets are marked by asterisks.

For Ni/TiO₂ and Ni/Davicat, there was no evidence for NiO particles with dimensions above the detectable limit of XRD (3-4 nm). NiO and MgO share similar crystal lattice characteristics, and consequently have nearly congruent diffraction patterns with peaks at 37, 43, and 63 °2θ (ICDD card files 47-1049 and 78-0430). Consequently, the technique could not conclusively determine the presence of NiO phases on the MgO support. No metallic nickel was observed on any of the materials. The lack of diffraction peaks for Ni/Davicat confirmed the amorphous nature of the silica-alumina support.

3.3.2 Support Study Catalytic Performance

The catalytic results and conditions for the ethylene and mixed olefin oligomerization reactions studied are presented in Table 3.2. The Brønsted acid-free TiO₂ and MgO supports were quickly ruled out as potential candidates for future studies. Only a trace presence of butenes was detected for the Ni/TiO₂ catalyst, while Ni/MgO was completely inactive. Though not unexpected based on literature precedent, these results confirmed the need for Bronsted acidity in forming an active catalyst and further called into question the presence of a direct relationship between the Lewis acid centers in silica-aluminas and their unique activity. This conclusion does rule out the possibility of a conjunctive interaction the two acid types and nickel. For example, nickel on Lewis-acidic gamma alumina is not known to be particularly active for ethylene dimerization, but when promoted by sulfate anions becomes a useful catalyst.⁷⁶

The Ni/ASA₂₅ catalyst produced 205 g_{olefins} kg_{catalyst}⁻¹ h⁻¹ at WHSV = 0.5 and pressure of 450 psig. The collected liquid products were colorless and slightly hazy. The mass yield of liquid products compounds was 75% in the C₄-C₈ range and 25% for C₁₀ and above (C₁₀₊). MS analysis found the products to be highly isomerized both in C-C double bond position and in methyl group branching. The degree of branching was generally limited to one or two methyl

substitutions along the carbon backbone. The isomerization activity is attributed mainly to the presence of unexchanged Brønsted acid sites.

Table 3.2 Reactor temperature (T) and pressure (P), conversion (X), selectivity of liquid products (S), and productivity values based on combined gas and liquid sample yields.

Catalyst	Feed type	T (°C)	P (psig)	WHSV (h ⁻¹)	X _{C2} (%)	X _{C3} (%)	S _{C4-} C ₈ (%)	S _{C10+} (%)	Productivity (g _{olefins} kg _{cat} ⁻¹ h ⁻¹)
Ni/ ASA ₂₅	95% C ₂ ⁼ , 5% argon	120	450	0.5	47	n.a.	75	25	205
Ni/ASA ₂₅	95% C ₂ ⁼ , 5% argon	120	290	1.0	2	n.a.	100	0	22
Ni/TiO ₂	95% C ₂ ⁼ , 5% argon	120	500	1.0	0.3	n.a.	100	0	1
Ni/MgO	95% C ₂ ⁼ , 5% argon	120	500	1.0	0	n.a.	n.a.	n.a.	0
Ni/ ASA ₂₅	70% C ₂ ⁼ , 25% C ₃ ⁼ 5% argon	120	200	0.75	8	20	38	62	95

The Ni/ASA₂₅ catalyst was then further studied for the oligomerization of a mixed olefin feed. The obtained productivity was 95 g_{olefins} kg_{catalyst}⁻¹ h⁻¹ with conversion values for ethylene and propylene of 8% and 20%, respectively, at conditions of 120 °C, pressure of 200 psig, and

WHSV = 0.75. The pronounced conversion of propylene in this experiment emphasized the challenge of ethylene activation when designing future catalysts for mixed olefin feeds.

The liquid products appeared lightly straw colored and clear, and the product distribution was shifted towards heavier products than for pure ethylene feed. The liquid yield of C₁₀₊ products was 62%. The increased yield of heavy products was perhaps due to the incorporation of the larger propylene olefin and by Brønsted-catalyzed reactions between propylene and higher olefins that occur through a carbocation-catalyzed pathway.

The conversion of ethylene was notably higher for the mixed feed at 200 psig total pressure (8% conversion, 140 psig ethylene pressure) than for pure ethylene at 290 psig total pressure (2% conversion, 275 psig ethylene pressure) at similar WHSV values. An explanation may be the co-monomer effect, in which the greater nucleophilicity of larger carbon chains serves to increase electron density about the metal center and thus modify activity.^{64, 154} Another explanation may be the activation of ethylene by coupling with carbocationic propylene formed on Brønsted sites. Although neither of these phenomena appear readily in the oligomerization literature, further review may enlighten if this effect is known elsewhere.

Figure 3.3 compares the liquid product distribution for ethylene and mixed olefin feeds over Ni/ ASA₂₅. For the ethylene feed, compounds with even carbon numbers were the dominant products, while small amounts of undecene (6%) and trace heptene (0.8%) were formed. Transalkylation and cracking over unexchanged Brønsted sites are the likely mechanisms for the formation of these odd-numbered compounds. The major product range was C₄-C₈ with a distinct tailing above C₁₀ products. The increasing concentration with carbon numbers between 4 and 8 may be due to a fractional condensation of the reactor effluent in the chilled knockout vessel owing to differences in boiling points.

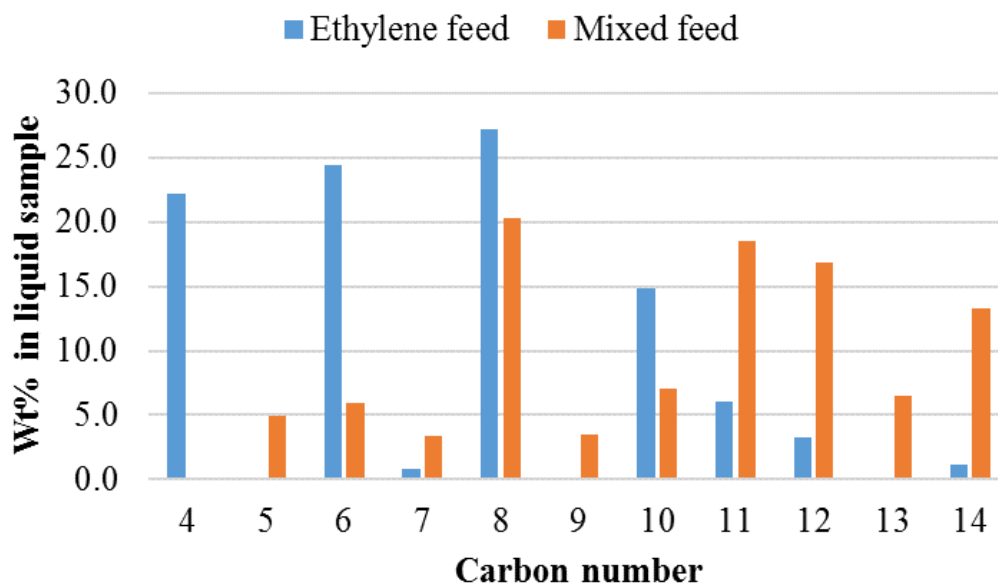


Figure 3.3 Condensed liquid product composition for mixed olefin and pure ethylene feed streams over Ni/ASA₂₅. Mixed feed conditions: 120 °C, 200 psig, 0.75 WHSV. Ethylene feed conditions: 120 °C, 450 psig, 0.5 WHSV.

No butene was present in the liquid sample produced from mixed olefins. Rather, the first oligomer formed was pentene, the coupling product of ethylene and propylene. Additionally, the high concentrations of octene, undecene, and tetradecene may suggest that propylene was more reactive than ethylene for adding to the initial pentene oligomer. This conclusion is supported by the minor concentration of C₇ relative to C₈ and C₉. The product distribution was not dominated by purely C₃ coupling products (C₆, C₉, C₁₂, etc.), as would be expected if propylene had undergone oligomerization more selectively with itself than with oligomers that had included ethylene.

3.3.3 Techno-Economic Analysis of Supported Nickel Catalysts

A techno-economic analysis of catalyst cost was performed on the basis of support type in order to assess the industrial impact of the studied materials. The price breakdown for each catalyst synthesis is shown in Table 3.3.

Table 3.3 Synthesis cost in 2015 dollars of nickel cation-type catalysts used for oligomerization based on an annual production scale of 1,000,000 lbs.

Support	Synthesis	Ni content (wt %)	Materials (\$/lb)	Processing (\$/lb)	Total (\$/lb)
Al-MCM-41	Ion exchange	0.6	854.14	12.03	866.17
ASA ₂₅	Ion exchange	2.06	1.66	12.03	13.68
ASA ₂₅	Impregnation	2.06	0.82	7.01	7.83
MgO	Impregnation	2.35	0.71	7.01	7.72
TiO ₂	Impregnation	2.27	1.81	7.01	8.82

The cost estimate for the silica-alumina and metal oxide supported catalysts were in the range of \$7-14/lb. A comparison between the price for Al-MCM-41 was prohibitively high (\$854/lb) due to the price of the blank support. A small scale of commercial production appears to be the dominant cost factor for this material at this time, as inferred from the limited options of only 5 or 25 g units of Al-MCM-41 presently offered for sale by Sigma Aldrich, and no other vendor was found to supply this material. These results conservatively imply that at least one order of magnitude price difference may be expected between catalysts prepared from Al-MCM-41 and more common supports such as amorphous silica-aluminas and metal oxides.

3.3.4 Influence of Synthesis Conditions on Ni/ASA Material Properties

The impact of synthesis conditions during the ion exchange of ASA₂₅ was studied to assess if reflux duration and nickel nitrate concentration would affect catalytic performance. Details of the reflux conditions and resulting textural properties are shown in Table 3.4. For two calcined Ni/Davicat samples, an additional ion exchange was performed with sodium nitrate in

effort to neutralize remaining Brønsted sites, denoted 2h+Na and 4h+Na. Elemental analysis was used to determine total Ni content, and TPR was used to determine the quantity of reducible Ni.

Table 3.4 Reflux conditions, element content, and textural properties of the catalysts used for the synthesis conditions study.

Sample	Reflux time (h)	Ni(NO ₃) ₂ •6H ₂ O (M)	Ni ^a (wt%)	NiO ^a (wt%)	Na ^a (wt%)	S _{BET} (m ² /g)	V _{pore} (cm ³ /g)
ASA ₂₅	--	--	--	--	0.04	484	0.72
2h	2	0.33	2.23	1.81	--	459	0.78
2h+Na	2	0.33	1.36	0.56	0.68	384	0.69
4h	4	0.33	2.23	1.57	--	477	0.65
4h+Na	4	0.33	1.63	0.87	0.46	425	0.65
8h	8	0.66	2.72	1.60	--	507	0.67

^a Determined by elemental analysis; ^b Determined by TPR.

The duration of reflux did not appear to have a strong effect on nickel incorporation, as the materials refluxed for 2 h and 4 h both resulted in a nickel content of 2.23 wt%. The loading increased to 2.72 wt% when the sample was refluxed for 8 h with a doubled nickel precursor concentration. The 2h and 4h materials responded differently to sodium exchange, with the 2h sample showing a greater loss of nickel and increased incorporation of sodium during the process than the 4h material. This may suggest that the longer duration of reflux in the 4h sample had resulted in the formation of more stable nickel species that were recalcitrant to further exchange.

A summary of the impact of reflux conditions on acidity of the resulting catalysts is shown in Table 3.5.

Table 3.5 Effect of nickel incorporation on acid properties of the ASA₂₅-supported catalysts used for the synthesis conditions study.

Sample	Total acid sites ^a ($\mu\text{mol/g}$)	Brønsted acid sites ^b ($\mu\text{mol/g}$)	Lewis acid sites ^b ($\mu\text{mol/g}$)	Site change upon IE (B/L)	Ni/Brønsted site lost (mol/mol)
ASA ₂₅	694	249	445	--	--
2h	628	121	506	-128/+61 (-51%/+14%)	3.0
2h+Na	455	130	325	-119/-120 (-48%/-27%)	1.9
4h	429	107	323	-143/-122 (-57%/-27%)	2.7
4h+Na	458	129	330	-119/-120 (-48%/-27%)	2.3
8h	565	127	438	-122/-7 (-49%/-2%)	3.8

^a Determined by NH₃ TPD; ^b Determined by NH₃ TPD and pyridine DRIFTS.

3.3.5 Relation of Material Properties to Catalytic Performance

In order to relate catalytic performance and material properties, the following section compares the conversion values of a mixed olefin feed to the nickel content and acidity of the finished catalysts. Due to hardware-related challenges with obtaining consistent liquid samples, the productivities are reported as yields of only the C₄-C₇ products measured by on-line analysis of the gas phase reactor effluent. The conversion values, productivities, and mass balances are given in Table 3.6.

Table 3.6 Conversion values of ethylene (X_{C2}) and propylene (X_{C3}), productivity to C₄-C₇ products, and mass balances (MB) for Ni/ASA₂₅ catalysts at TOS = 5 h, WHSV = 1, T = 120 °C, and P_{total} = 200 psig.

Sample	X _{C2} (%)	X _{C3} (%)	Productivity to C ₄ -C ₇ (g _{olefins} kg _{cat} ⁻¹ h ⁻¹)	MB (%)
ASA ₂₅	0	26.9	38	92
2h	11.9	34.0	125	83
2h+Na	3.3	16.8	71	95
4h	7.2	31.2	110	88
4h+Na	6.3	30.2	86	92
8h	10.7	29.8	119	86

Ethylene conversion showed no dependence on the Brønsted acidity of the catalysts, which remained approximately consistent across the range of samples (Figure 3.4). Rather, a dependence was found with the Lewis acidity of the catalyst. As the Ni-free support was inactive

for ethylene conversion despite having considerable Lewis acidity, it is inferred that the correlation resulted from the concentration of Lewis acidic, cationic nickel species. Interestingly, sodium exchange resulted in a diminished ethylene activity of the nickel-containing catalysts but had little effect on the amount of Lewis acidity.

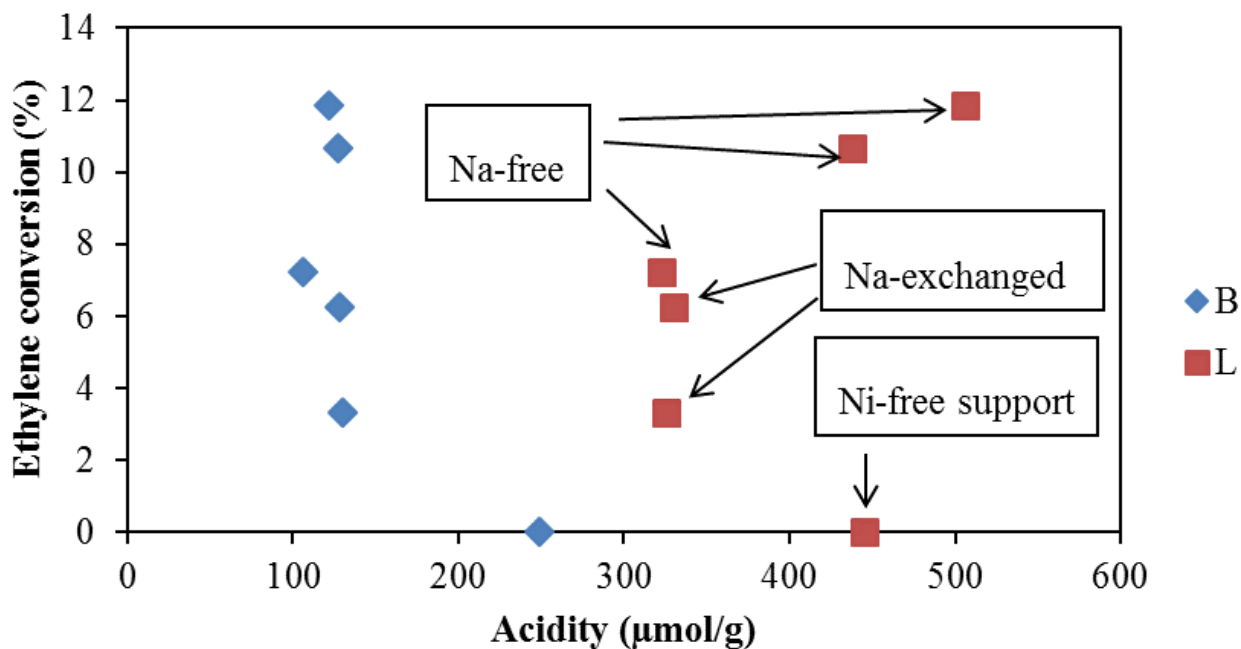


Figure 3.4 Impact of acidity types and sodium exchange on ethylene conversion.

A comparison of measured nickel content with respect to ethylene conversion resulted in a moderately linear correlation. A comparison between total nickel and nickel oxide content estimated by EA and TPR, respectively, found similar slopes but different y-intercept offsets for the line of best fit, as shown in Figure 3.5.

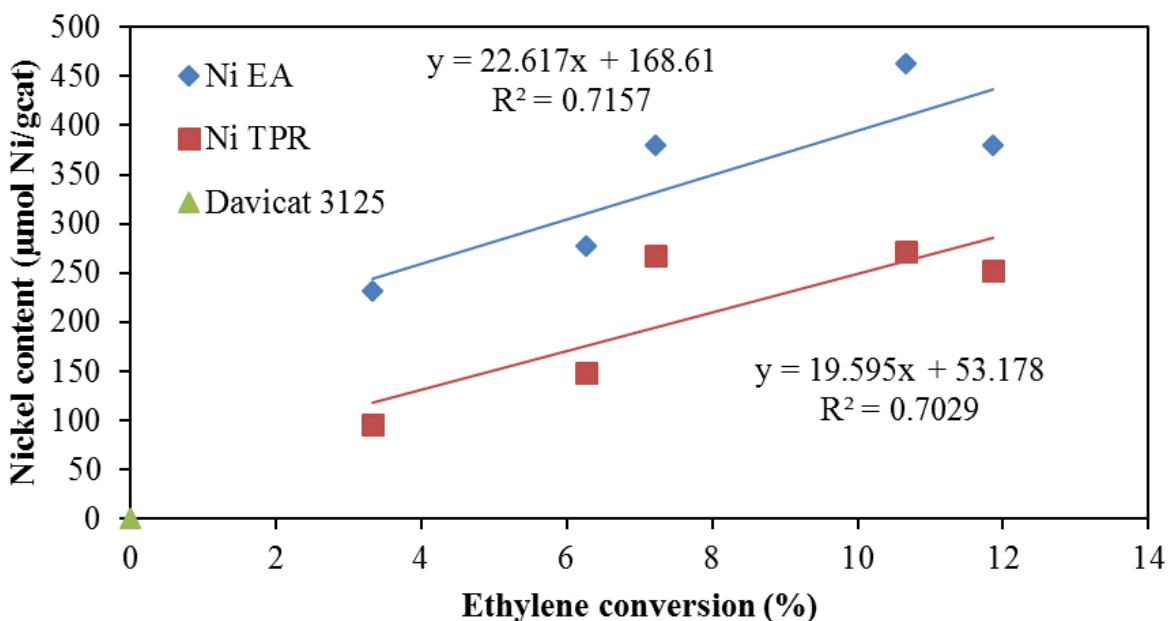


Figure 3.5 Conversion of ethylene with respect to estimated nickel content.

The greater y-intercept of 169 $\mu\text{mol Ni/g}_{\text{cat}}$ for the EA method suggests an overestimate of the number of active nickel species relative to TPR, with a y-intercept of 53 $\mu\text{mol Ni/g}_{\text{cat}}$. It can be ruled out that the y-offset was affected by support activity, as the Ni-free Davicat was completely inactive for ethylene conversion. To explain this result, it is put forth that oxidic, or reducible, nickel species are indeed active for ethylene conversion. This conclusion is supported in recent literature.⁴⁸ However, it remains unclear why both methods overestimated the number of active species. The stoichiometry used to assess NiO content by TPR experiments assumes the presence of only Ni^{II} . Literature widely reports these catalysts as containing almost exclusively Ni^{II} , with some reports of trace Ni^{I} being present.³⁸ To further assess the impact of nickel oxide on catalytic activity, the catalytic contributions of nickel oxide species having different reduction temperatures could be probed by the application of reductive pretreatments at varying temperatures prior to catalytic testing.

Propylene converted readily over the Ni-free support, although there appeared no correlation between conversion and Brønsted acidity in the nickel-containing catalysts (Figure 3.6). In general, the Ni-containing catalysts with higher Lewis acidity were more active. There was one outlier to this trend, in which the propylene conversion over the 4h sample was higher than expected. This result remains unexplained. It is notable that the 4h sample had fewer Lewis sites and was less active towards ethylene conversion than the 2h sample, despite containing the same amount of total nickel.

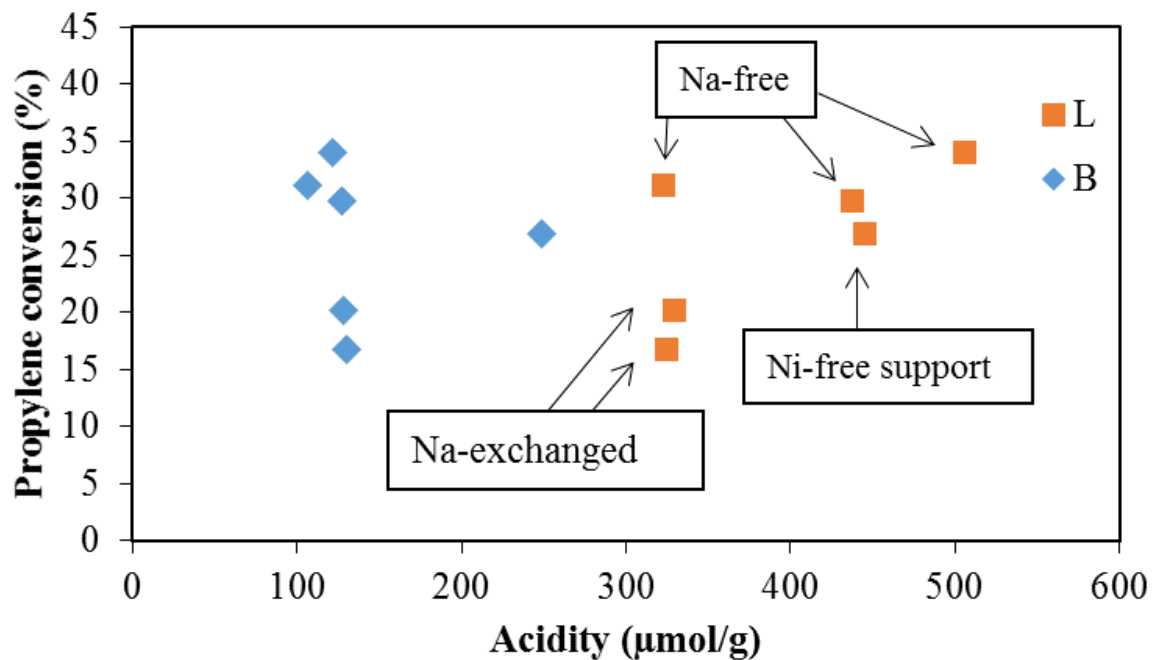


Figure 3.6 Impact of acidity types and sodium exchange on propylene conversion.

As shown in Figure 3.7, the propylene activity of nickel-containing catalysts depended more strongly on whether the samples had been sodium-exchanged than on nickel content. In this comparison, it becomes more complicated to interpret best fit lines for the number of active species due to the activity of the support. The EA method in this case again overestimates the

number of active species based on nickel content, although by a smaller y-intercept here of 69.6 $\mu\text{mol Ni/g}_{\text{cat}}$. Conversely, the TPR method underestimates active sites, with a negative y-intercept of 63.8 $\mu\text{mol/g}$.

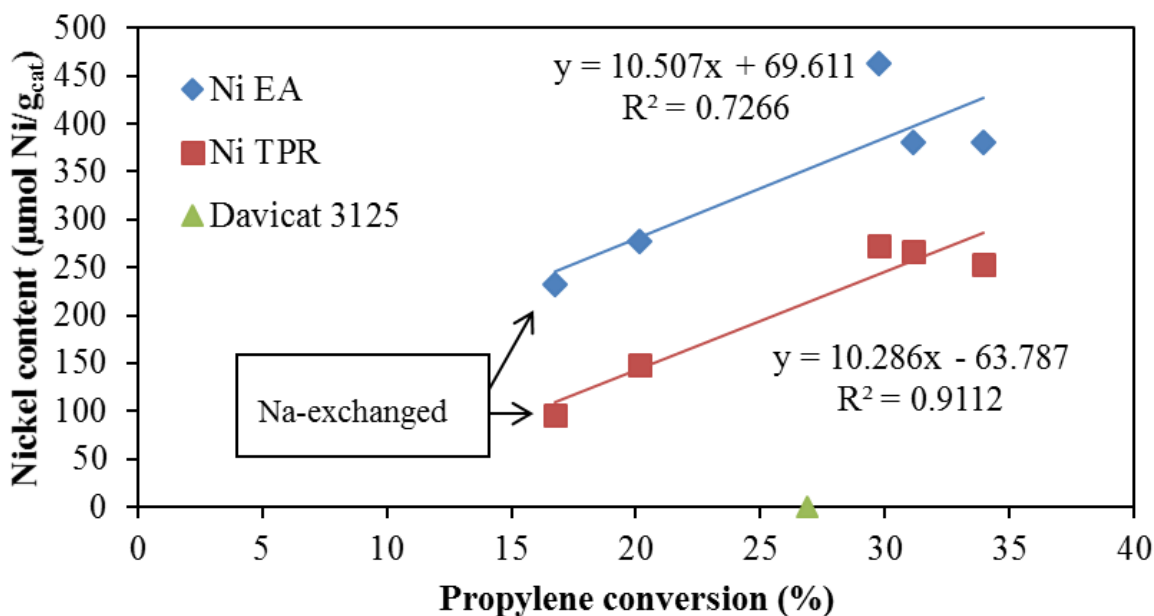


Figure 3.7 Conversion of propylene as a function of nickel content for ASA.

It would explain the decrease in offset for each method if, following nickel incorporation, the support retained Brønsted sites that were active for propylene oligomerization. This conclusion of catalyst bifunctionality was expected given the literature,⁷² and also explains the underestimation of total active sites with regard to nickel and nickel oxide content.

Despite the invariance in Brønsted acidity of the catalyst synthesized, there appeared a clear inverse correlation between nickel content and the ratio of Brønsted to Lewis acidity, as shown in Figure 3.8. Thus, it is possible to envision nickel incorporation and subsequent removal by Na ion exchange as a “give and take” of Lewis acidity.

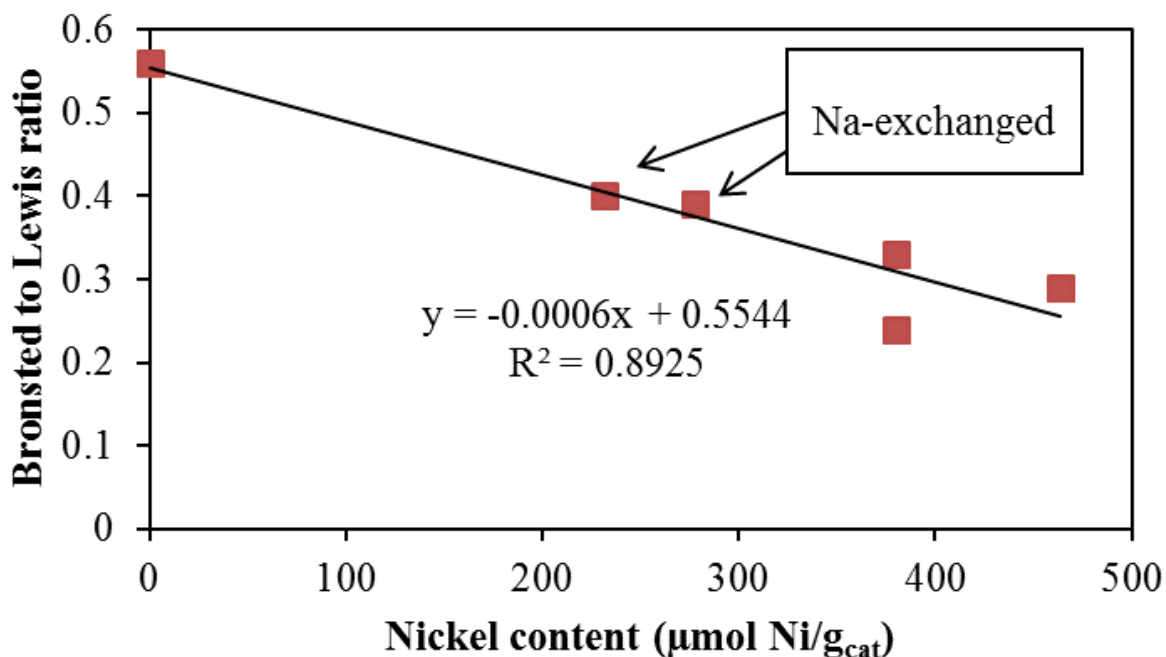


Figure 3.8 Effect of nickel content on Brønsted to Lewis acid site ratio of Davicat catalyst as determined by pyridine-DRIFTS experiments.

3.3.6 Effect of Aluminum Content in Amorphous Silica Alumina Supports

To study the effect of aluminum content and speciation in ASAs on nickel speciation, two Davicat materials were compared that contained 15 and 25 wt% aluminum, denoted ASA₁₅ and ASA₂₅, respectively. A low nominal loading of 1 wt% Ni was targeted to remain below the ion exchange capacity of both materials, as estimated by previous experiments with the ASA₂₅ support that found nickel uptake in the range of 2.2-2.7 wt% at saturation. The synthesis conditions are given in Table 3.7.

SEM micrographs of the two supports are shown below in Figure 3.9. The particle sizes and shapes of the silica-alumina supports were very similar for Ni/ASA₁₅ and Ni/ASA₂₅, with most particles being spherical or slightly ovoid in shape and having a diameter of about 70 µm.

Table 3.7 Reflux conditions, element content, and textural properties of the ASAs.

Sample	Reflux time (h)	Ni ^a (wt%)	S _{BET} (m ² /g)	V _{pore} (cm ³ /g)
ASA ₂₅	--	--	484	0.72
Ni/ASA ₂₅ 0.964%	4	0.96	421	0.73
ASA ₁₅	--	--	414	1.18
Ni/ASA ₁₅ 0.904%	4	0.90	336	1.02

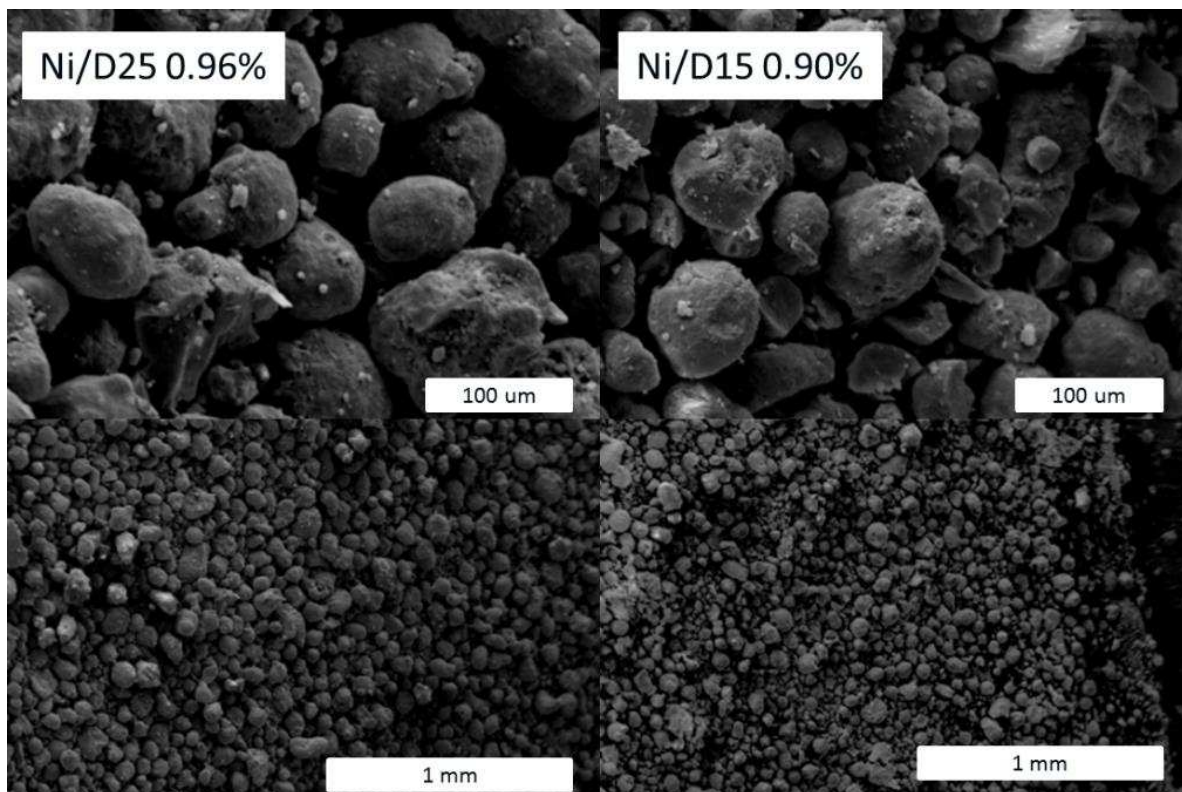


Figure 3.9 SEM of nickel supported on ASA₁₅ and ASA₂₅ silica-aluminas.

Analysis by ^{27}Al MAS NMR was used to differentiate the local environments of aluminum present in the silica-alumina supports (Figure 3.10). The NMR spectra of zeolite BEA and mesoporous Al-MCM-41 are also shown for comparison. In zeolite BEA, aluminum is located nearly entirely within tetrahedral environments and is distinguished by two separate framework species at 55 ppm and 59 ppm.¹⁵⁵ These peaks correspond to the T1/T2 and T3-T9 aluminum sites of the BEA zeolite, respectively.

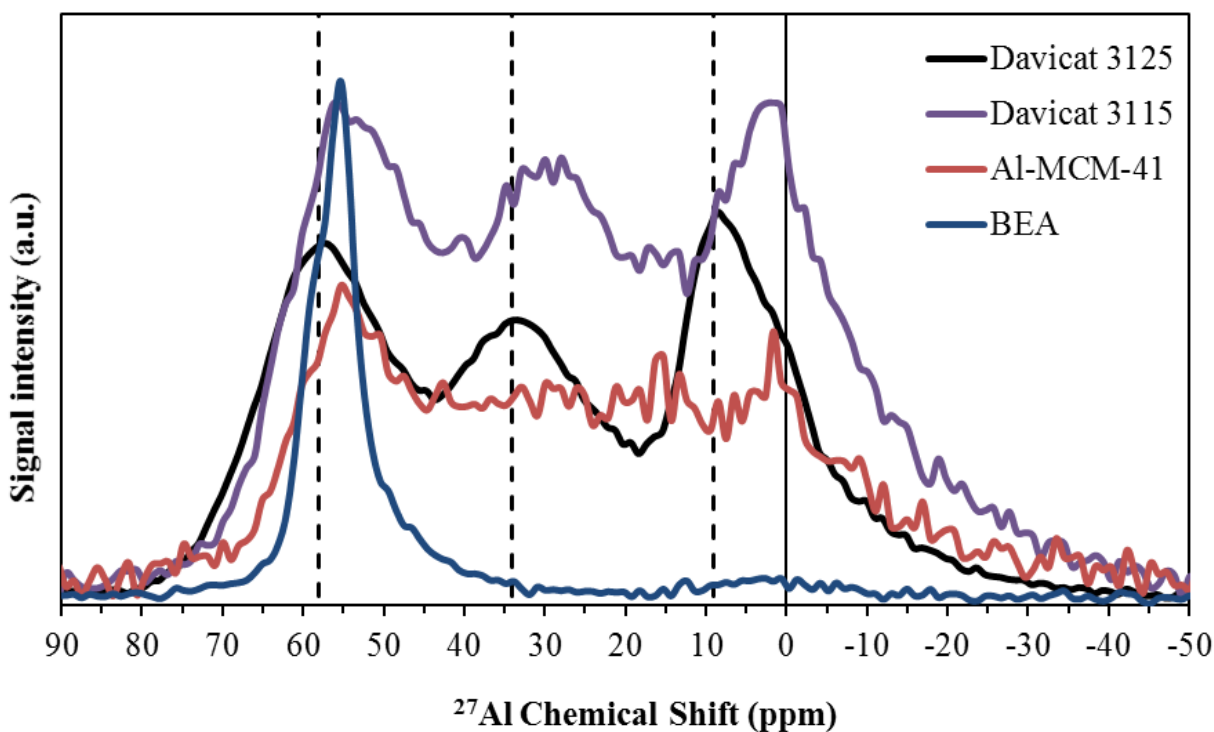


Figure 3.10 ^{27}Al MAS NMR spectra of ASA supports, BEA zeolite, and Al-MCM-41.

ASA₂₅ and ASA₁₅ were found to contain aluminum having 4-, 5-, and 6-coordinate environments centered near peak shifts of 55, 33, and 0 ppm, respectively. As a trend, the peaks for the more aluminum-rich ASA₂₅ were broader and shifted further downfield compared to ASA₁₅. This is consistent with a broader distribution of aluminum environments and greater

distortion from the nominal tetrahedral, trigonal bipyramidal, and octahedral geometries.

Furthermore, the higher intensity of octahedral species relative to tetrahedral species in ASA₂₅ indicated that a lower percentage of aluminum was present as framework-type sites.

The hydration of the samples can play a large role in the coordination of aluminum. Lower degrees of hydration tend to push aluminum into lower coordination environments,⁹⁸ and heighten the impact of second order quadrupolar interactions by aluminum.¹⁵⁶ A lessening of the degree of 6-coordinate aluminum and upon dehydration was observed for the ASA₂₅ sample after drying at 200 °C overnight (Figure 3.11). This comparison gives an indication of the effect of thermal pretreatment on the support. The 6-coordinate Al species are those most impacted by drying and suggests that it is these species which possess the greatest coordinative flexibility in the material. The effect of these flexible Al species on the environment of Ni is not known, although their responsiveness to the catalyst pretreatment suggests they may play a role in catalyst activation.

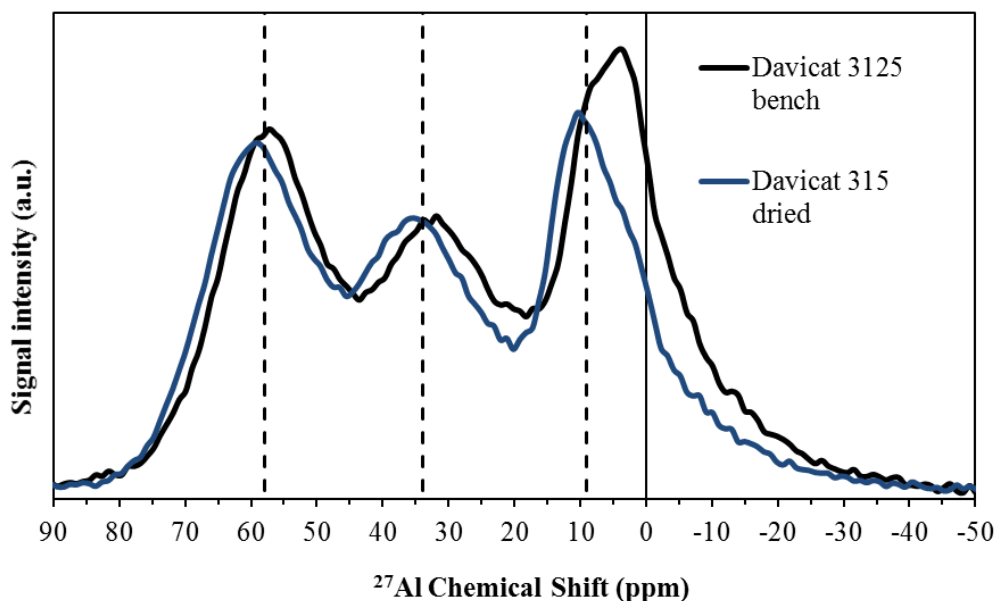


Figure 3.11 ²⁷Al MAS NMR spectra of Ni/ASA₂₅ before and after drying.

The relative strength, density, and type of acid sites on each of the silica-alumina supports was compared by NH₃ TPD and pyridine DRIFTS (Table 3.8). The total number of acid sites determined by NH₃ TPD was slightly lower for ASA₂₅ at 656 μmol/g compared to 712 μmol/g for ASA₁₅. The distribution of sites in the more aluminum-rich ASA₂₅ tended towards weaker species than ASA₁₅, as evidenced by a more intense main desorption peak at *ca.* 200 °C and less pronounced tailing at higher temperatures. The Brønsted sites on ASA₁₅ were more greatly impacted by the incorporation of nickel than that of ASA₂₅, with a 69% loss for ASA₁₅ compared to 51% for ASA₂₅. The stoichiometry of nickel atoms per Brønsted site lost was 1.3 for ASA₂₅ and 0.8 for ASA₁₅.

Table 3.8 Acid properties of the ASA₁₅- and ASA₂₅-supported catalysts.

Sample	Total acid sites ^a (μmol/g)	Brønsted acid sites ^b (μmol/g)	Lewis acid sites ^b (μmol/g)	Site change upon IE (B/L)	Ni/Brønsted site lost (mol/mol)
ASA ₂₅	694	249	445	--	--
Ni/ASA ₂₅ 0.96%	469	122	347	-127/-98 (-51%/-22%)	1.3
ASA ₁₅	475	275	200	--	--
Ni/ ASA ₁₅ 0.90%	211	85	126	-189/-75 (-69%/-37%)	0.8

The skewing of acidities to higher strengths in the silica-alumina having lower aluminum content coincided with pyridine DRIFTS experiments that found the ratio of Brønsted to Lewis sites to be higher in ASA₁₅ than in ASA₂₅. Taken together with the ²⁷Al MAS NMR experiments, these results suggest that the higher relative concentration of octahedral aluminum species present in ASA₂₅ contributes to its increased Lewis acidity with most sites having a weaker binding affinity for the basic probe molecule ammonia. The surprisingly low amount of acid sites measured by NH₃ TPD for ASA₂₅ may indicate that octahedral, extra-framework Lewis acid species have coordinated with tetrahedral, framework-type Brønsted sites to act as charge-balancing cations and to potentially “hide” some of the total acidity of this material, as has been observed in other aluminosilicate systems.^{155, 157-159}

Temperature-programmed reduction with hydrogen (H₂ TPR) experiments were performed to differentiate the impact of support on nickel speciation Figure 3.12. The primary events observed were reduction of oxidic nickel having weak interaction with the support ($T_{\text{red.}} < 400$ °C), oxidic nickel having strong support interactions from ($400 < T_{\text{red.}} < 650$ °C), and ionic nickel in strong association with the alumina phase, perhaps as a nickel aluminate or spinel-type structure ($650 < T_{\text{red.}} < 900$ °C).

Ni/ASA₂₅ showed primarily oxidic character having strong support interactions and a minor contribution of nickel strongly associated with the alumina phase. In contrast, Ni/ASA₁₅ was almost exclusively in strong coordination with alumina, and less reducible overall in comparison with Ni/ASA₂₅.

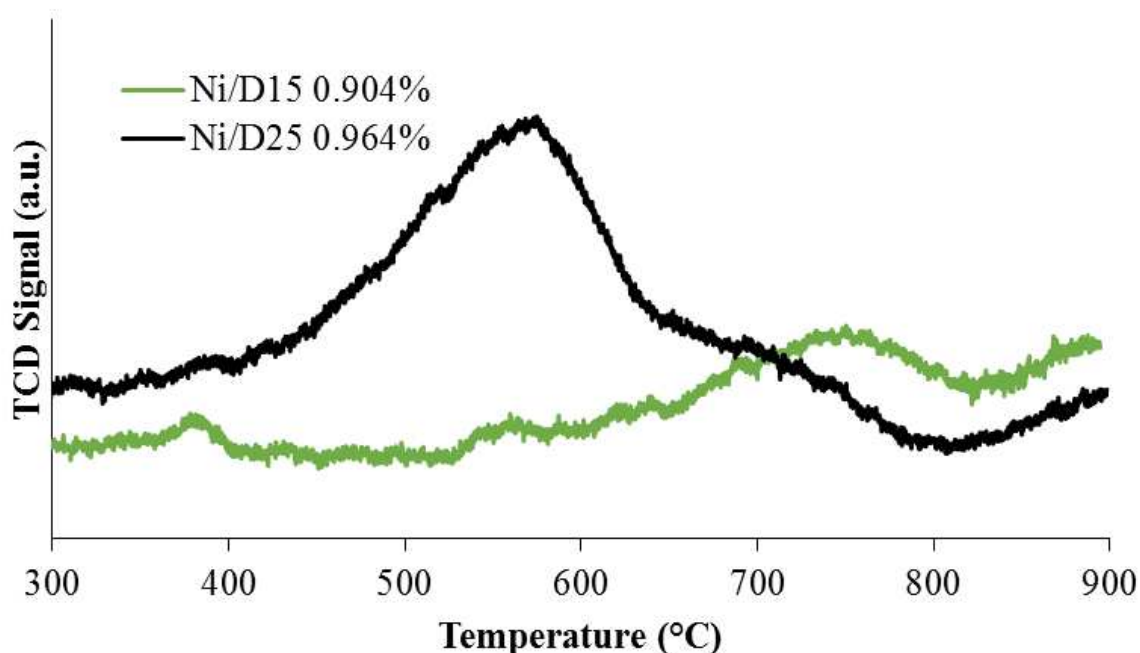


Figure 3.12 TPR profiles comparing low-loading Ni after background subtraction of each support, respectively.

XPS was used to probe the binding energies of Ni $2p_{3/2}$ and $2p_{1/2}$ core-shell electrons of nickel present within the surface of the support (<10 nm). The binding energy for the Ni $2p_{3/2}$ peak for both supports closely matched the reported binding energy position for nickel hydroxide ($\text{Ni}(\text{OH})_2$) at 856.0 eV (Figure 3.13).¹⁶⁰ These results do not support the conclusion of a nickel hydroxide phase *per se*, but rather the presence of nickel having a very similar electronic environment and resulting binding energy.

A higher energy shoulder at 857.1 eV was observed on the ASA_{15} support at higher loading (0.9%), and on the $\text{Ni}/\text{ASA}_{25}$ support at lower loading (0.25%). This shoulder was not

observed on the 0.96% Ni/ Ni/ASA₂₅ sample, suggesting a different interaction or coordination with aluminum on this support.

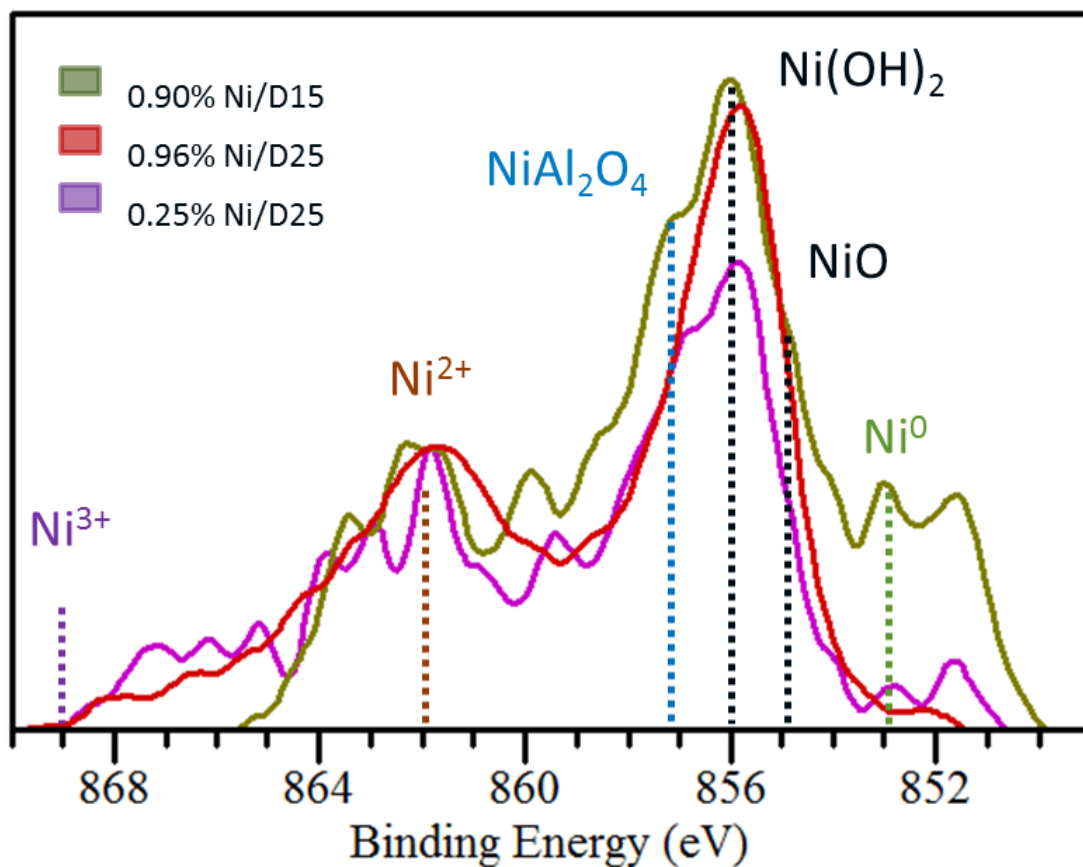


Figure 3.13 X-ray photoelectron spectra of nickel-containing samples normalized to the Ni 2p_{1/2} peak intensity with binding energy positions of Ni(OH)₂, NiO, and Ni⁰ as reported in Biesinger et al.¹⁶⁰ and of NiAl₂O₄ as reported in Li et al.¹⁶¹

In comparing the raw spectra, 0.96% Ni/ASA₂₅ showed significantly higher nickel intensity than 0.9% Ni/ASA₁₅ (Figure 3.14). This suggests differences in the radial distribution of nickel within these two supports, where ASA₁₅ had incorporated nickel further within the bulk of the support particle.

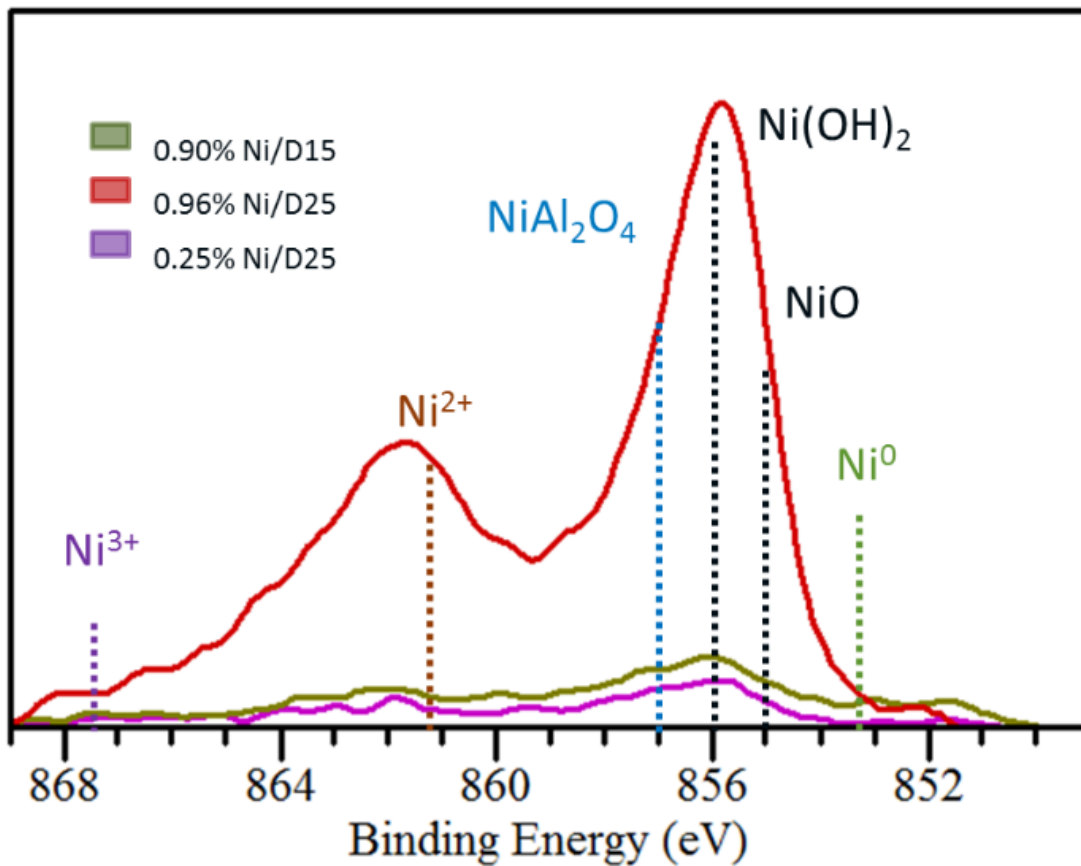


Figure 3.14 Raw X-ray photoelectron spectra of nickel-containing samples.

The trend of nickel signal intensity correlated with aluminum signal for both supports, and thus suggested that nickel preferred association with the aluminum-rich phase. Further analysis by transmission electron microscopy (TEM) is warranted to further define the nanostructure of these catalysts and identify the presence and distribution of nickel oxide- and nickel hydroxide-type domains.

3.3.7 Catalytic Properties of the ASA Supports

The experimental conditions for the comparison of Ni/ASA₁₅ and Ni/ASA₂₅ were to be evaluated with an ethylene feed at high WHSV (~25) and low pressure (<100 psig) in effort to limit diffusion limitations. An initial comparison of conversion and product isomer selectivity suggested substantial differences between the two materials. However, it was discovered that

during these experiments a failure of the MFC for delivering ethylene had begun to occur over the course of several days. This resulted in a gradual loss of control over both the WHSV and reactor pressure. The obtained results could thus not be considered as steady state, and as a result no comparison can yet be made between the catalytic performance of these catalysts until these experiments are repeated.

3.4 Discussion

Recently, the high oligomerization activity of nickel supported on structured mesoporous silica-alumina and amorphous silica alumina has been attributed to the presence of nickel in coordination with the moderately acidic silanols and aluminols of the support and low-coordinate nickel on the corners and edges of nickel oxide nanoparticles.⁴⁸ In this work, the support electronic donor/acceptor properties were hypothesized to impact the electrophilicity and resulting catalytic activity of nickel sites. In initial experiments, the inactivity of nickel on basic MgO demonstrated the need for electron withdrawing capacity of the support, while trace butenes produced from ethylene over Ni/TiO₂ evidenced a very weak potential for a purely Lewis acidic support to generate active nickel. Nickel was then shown to be active when supported on a silica alumina having combined properties of Brønsted and Lewis acidity.

Amorphous silica alumina was shown to be superior to mesostructured Al-MCM-41 in terms of cost and commercial-readiness and was selected for further studies to demonstrate the conversion of mixed olefins to liquids, and to evaluate the impact of synthesis conditions on material properties and resulting catalytic activity.

The oligomerization of mixed olefins over Ni/ASA resulted in a higher average product molecular weight than for a pure ethylene feed. This is thought to be due to the incorporation of the higher carbon number propylene in the growing oligomer chains, as well as a greater

involvement of the Brønsted-catalyzed pathway that proceeds through an activation of propylene and higher olefins. The formation of C₅ as the lightest oligomer product suggested that initial coupling was favored between ethylene and propylene, rather than direct ethylene-ethylene or propylene-propylene coupling. The coupling of ethylene to propylene was nickel-catalyzed, as the nickel-free support showed no activity for ethylene conversion. The predominance of C₈ over C₇ and C₉ species in the liquid product stream suggested that the carbon chain was initiated by ethylene coordination, followed by subsequent additions of propylene. This may be an electronic effect, where the insertion of propylene into the nickel-ethylene complex occurs more readily due to its greater nucleophilicity and by its capacity to spread charge transfer over two resonance structures. As the conversion of ethylene increased in the presence of propylene, it is proposed that insertion of the second olefin is the rate-limiting step and that the more-favored insertion of propylene mitigates this limitation. Conversely, this argument is extended to the case where nickel first coordinates to propylene, followed by ethylene coordination and insertion. Further investigation into the literature may yield insights into the favored order of insertion.

The incorporation of nickel was found to reduce the Brønsted acidity of the support and increase Lewis acidity. The number of Brønsted acid sites were relatively invariant between catalyst preparations except when further exchanged with Na, which reduced both the number of Brønsted sites and nickel content of the catalysts.

The material properties of nickel content, nickel oxide content, and acidity were evaluated as metrics for catalytic activity in terms of ethylene and propylene conversion. The conversion of ethylene increased proportionally to the Lewis acidity of the nickel-containing, sodium-free catalysts, and is considered to reflect the amount of cationic nickel species present that are available for coordination with gas-phase species.

Although both nickel oxide and total nickel content overestimated the number of active sites when the lines of best fit were extrapolated to zero conversion, nickel oxide content proved to be a more accurate measure of active sites. This result indicated that a portion of the nickel content was inactive, and the active portion was reducible by H₂ in the range of 350 to 750 °C. The nickel species not reduced under these conditions may be either in very strong interaction with the support or are occluded by non-reducible support phases. It is consequently of interest to evaluate the activity of catalysts after reducing pretreatments that scan this window of reduction to assess the relative catalytic contribution of nickel oxides based on their reducibility. These experiments were not performed in this work due to time limitations.

Finally, the effect of alumina concentration and coordination in the ASA support on nickel speciation was studied. The lower alumina content support, ASA₁₅, was found to possess a greater fraction of tetrahedral aluminum, and correspondingly higher ratio of Brønsted to Lewis sites. These Brønsted sites were more readily exchanged, or diminished, by the incorporation of nickel, and resulted in the formation of fewer Lewis sites than on the higher alumina content ASA₂₅. The formed nickel species on ASA₁₅ were less reducible than those formed on ASA₂₅. It is concluded from this comparison that Lewis-acidic aluminum species having coordination numbers of 5 and 6 aid in the formation of cationic nickel species that are active for oligomerization and remain susceptible to reduction due to their environment.

Tests to evaluate the catalytic differences of these materials and complete the analysis of structure-property-performance relations were halted by hardware issues but remain a high priority once facilities become available.

3.5 Conclusion

A rigorous support study was performed to investigate the role of support acceptor/donor properties and acid type on nickel-containing oligomerization catalysts. The presence of a Brønsted acid support functionality was essential for the formation of a highly active catalyst, while the purely Lewis acidic TiO₂ support showed only weak activity for butene production and the basic support MgO was inactive. ASAs were selected for further detailed study based on their activity and cost relative to well-ordered, mesoporous silica-aluminas. A set of Ni/ASAs were evaluated for the oligomerization of mixed olefins based on their acid properties and nickel content. The Lewis site density of the finished catalysts was well correlated with ethylene conversion. No relation was found between Brønsted acidity and olefin conversion.

Nickel addition improves the conversion of propylene. A comparison of two ASA supports containing 15 and 25 wt% Al₂O₃ found the interaction between nickel and the support to be substantially different. Upon nickel incorporation, Brønsted sites were more readily exchanged on ASA₁₅, while more Lewis sites were created on ASA₂₅. The nickel species on Ni/ASA₂₅ were found to be more reducible in TPR experiments than those on Ni/ASA₁₅. The higher coordinate aluminums are thought to be involved in the formation of these reducible, cationic nickel species. XPS found the surface concentration of nickel and aluminum to be higher on Ni/ASA₂₅, and the predominant nickel feature on both supports aligned with a peak position of 856.0 eV, consistent with the peak position of Ni(OH)₂. Future work will be to repeat catalytic experiments to compare the activity of these two catalysts.

3.6 Acknowledgements

This work was supported by the Department of Energy's Bioenergy Technology Office under Contract no. DE-AC36-08-GO28308. Dr. Erica Gjersing is gratefully thanked for

performing ^{27}Al NMR experiments. Mike Dzara and Sam Gage are gratefully acknowledged for the collection and analysis of XPS data.

CHAPTER 4

RU-SN/AC FOR THE AQUEOUS PHASE REDUCTION OF SUCCINIC ACID TO 1,4-BUTANEDIOL UNDER CONTINUOUS PROCESS CONDITIONS

Reprinted in part from a paper published in *ACS Catalysis*¹

Derek R. Vardon,^{*} Amy E. Settle,² Vassili Vorotnikov,² Martin J. Menart,^{‡,2} Todd R. Eaton,² Kinga A. Unocic,³ K. Xerxes Steirer,⁴ Kevin N. Wood,⁴ Nicholas S. Cleveland,² Kathleen E. Moyer,² William E. Michener,² and Gregg T. Beckham²

4.1 Abstract

Succinic acid is a biomass-derived platform chemical that can be catalytically converted in the aqueous phase to 1,4-butanediol (BDO), a prevalent building block used in the polymer and chemical industries. Despite significant interest, limited work has been reported regarding sustained catalyst performance and stability under continuous aqueous-phase process conditions.

¹ Reprinted with permission from DOI: [10.1021/acscatal.7b02015](https://doi.org/10.1021/acscatal.7b02015) (article) *ACS Catal.* 2016, 7, 6207-6219. Copyright 2016 American Chemical Society.

² National Bioenergy Center, National Renewable Energy Laboratory, 15013 Denver West Parkway, Golden, CO 80401.

³ Materials Science and Technology Division, Oak Ridge National Laboratory, Oak Ridge, TN 37831.

⁴ Interfacial and Surface Science, National Renewable Energy Laboratory, 15013 Denver West Parkway, Golden, CO 80401.

^{*} Primary researcher and corresponding author.

[‡] Performed all chemisorption experiments and analysis.

As such, this work examines Ru-Sn on activated carbon (AC) for the aqueous-phase conversion of succinic acid to BDO under batch and flow reactor conditions. Initially, powder Ru-Sn catalysts were screened to determine the most effective bimetallic ratio and provide a comparison to other monometallic (Pd, Pt, Ru) and bimetallic (Pt-Sn, Pd-Re) catalysts. Batch reactor tests determined that a ~1:1 metal weight ratio of Ru to Sn was effective for producing BDO in high yields, with complete conversion resulting in 82% molar yield. Characterization of the fresh Ru-Sn catalyst suggests that the sequential loading method results in Ru sites that are collocated and surface-enriched with Sn. Postbatch reaction characterization confirmed stable Ru-Sn material properties; however, upon a transition to continuous conditions, significant Ru-Sn/AC deactivation occurred due to stainless steel leaching of Ni that resulted in Ru-Sn metal crystallite restructuring to form discrete Ni-Sn sites. Computational modeling confirmed favorable energetics for Ru-Sn segregation and Ni-Sn formation at submonolayer Sn incorporation. To address stainless steel leaching, reactor walls were treated with an inert silica coating by chemical vapor deposition. With leaching reduced, stable Ru-Sn/AC performance was observed that resulted in a molar yield of 71% BDO and 15% tetrahydrofuran for 96 h of time on stream. Postreaction catalyst characterization confirmed low levels of Ni and Cr deposition, although early-stage islanding of Ni-Sn will likely be problematic for industrially relevant time scales (i.e., thousands of hours). Overall, these results (i) demonstrate the performance of Ru-Sn/AC for aqueous phase succinic acid reduction, (ii) provide insight into the Ru-Sn bimetallic structure and deactivation in the presence of leached Ni, and (iii) underscore the importance of compatible reactor metallurgy and durable catalysts.

4.2 Catalyst Synthesis

Catalysts were loaded onto nitric acid treated Darco activated carbon powder and granular supports (Sigma). Activated carbon powder was initially sieved to < 270 mesh (53 μm) and granular pellets (30-50 mesh; 300-600 μm) were used as received. Activated carbon support was initially treated with concentrated nitric acid for 12 h at room temperature. After acid treatment, the carbon was washed with DI water until a neutral wash pH was observed. Following acid treatment, the support point of zero charge was measured by adding pH-adjusted water solutions in an amount slightly above the pore volume of the support to form dense slurry.¹⁶² Three initial solution pH values were used (pH 4, 6, 8) and the slurry was allowed to reach equilibrium. The final slurry equilibrium pH reading was measured for each starting pH, and the average value reported as the point of zero charge. Primary platinum group metals were loaded onto the support by strong electrostatic adsorption.¹⁶³⁻¹⁶⁴ Catalysts were prepared by adding 9.6 g of activated carbon into a large beaker with ~300 mL of deionized water. Due to the acidic nature of the carbon support, the pH of the solution was raised to 11.5-12.0 using NH_4OH to deprotonate the support. In a separate beaker, the target metal cationic precursor was added to ~150 mL of DI water. Precursors were obtained from Sigma Aldrich and included tetraamineplatinum (II) nitrate, tetraaminepalladium (II) chloride monohydrate, and hexamine ruthenium (III) chloride. Both solutions were then combined and allowed to stir at 350 rpm for at least 2 h. After stirring, the catalyst particles were vacuum filtered, dried, and reduced in 200 sccm of pure H_2 for 4 h. Pt and Ru were reduced at 300 $^\circ\text{C}$, while Pd was reduced at 150 $^\circ\text{C}$ to minimize sintering.¹⁶⁵ The filtrate was recovered, and the primary metal loading process was repeated until the filtrate appeared colorless. Secondary oxophilic metals (e.g., Re, Sn) were loaded onto the monometallic catalysts by incipient wetness impregnation. Sn bimetallics were

prepared using tin(II) chloride (Sigma Aldrich) dissolved in a minimal amount of acetone. Re bimetallics were prepared using ammonium perrhenate dissolved in water. Precursor solutions were added drop-wise with continuous manual stirring. Loaded catalysts were then dried and reduced in 200 sccm of pure H₂ at 350 °C for Pd-Re and at 450 °C for Sn bimetallics for at least 2 h at temperature. For pyridine DRIFTS control experiments, monometallic Sn was prepared on powder activated carbon by incipient wetness and reduced at 450°C. All catalysts were stored under ambient conditions with air exposure following synthesis.

4.3 Chemisorption Methods

Chemisorption and TPR of catalyst materials were performed using an Autochem II instrument (Micrometrics). The metal surface area of Pt and Pt-Sn was determined by H₂ pulse, Ru and Ru-Sn by H₂ TPD, Ru-Sn by CO pulse, and Pd and Pd-Re by H₂-O₂ titration. Prior to chemisorption analysis, samples were reduced at 250 °C (2 °C min⁻¹, 2 h) under flowing H₂ (10% in Ar, 50 sccm). For H₂ pulse, CO pulse, and H₂-O₂ titration experiments, samples were cooled to a dosing temperature of 40 °C under inert flow prior to analysis. TPR experiments were performed by pretreatment under flowing inert (60 °C, 1 h) followed by ramping to 650 °C under H₂. Calculations for metal dispersion and surface area were performed using the Autochem II software on the basis of metal content as determined by elemental analysis.

4.4 CO and H₂ Affinity and TPRs of Bifunctional Catalysts

Chemisorption of the Pd-Re catalyst showed a significant increase in H₂ uptake (456 μmol g⁻¹) in comparison to monometallic Pd (70 μmol g⁻¹), highlighting the effect of Re addition on hydrogen affinity. Surprisingly, Pt-Sn and Ru-Sn catalysts displayed extremely low H₂ uptake (<5 μmol g⁻¹) (Table 4.2) in comparison to their monometallic counterparts (Pt, 70 μmol g⁻¹; Ru, 47 μmol g⁻¹) (Table 4.1), highlighting the suppression of H₂ affinity by Sn.

Further testing of Ru-Sn by CO pulse chemisorption also showed muted uptake ($5.9 \mu\text{mol g}^{-1}$) (Table S2), suggestive of a Sn-enriched surface that decreases the binding affinity for both molecules.¹⁶⁶⁻¹⁶⁷

Table 4.1 H₂ chemisorption of fresh monometallic catalysts used in batch screening reactions for succinic acid reduction to BDO.

Monometallic Catalyst	H ₂ uptake ($\mu\text{mol g}^{-1}$)	Dispersion (%)	Particle dia. (nm)
5.2% Pt/PAC	70.2 ^a	53	2.2
4.6% Pd/PAC	44.2 ^b	21	5.5
4.3% Ru/PAC	46.8 ^c	22	5.0

^aPt measured by H₂ pulse; ^bPd measured by H₂-O₂ pulse; ^cRu measured by H₂ TPD.

The incorporation of Sn had a muting effect on H₂ activation, where H₂ chemisorption showed only 9% of the H₂ uptake in comparison to monometallic Ru (Table 4.1 and Table 4.2). This effect was also observed when Sn was added to the Pt/PAC system. The promotion of Pd by Re induced a dramatic increase in chemisorbed hydrogen.

Temperature-programmed reduction (TPR) profiles further highlighted the influence of Sn on catalyst behavior (Figure 4.1 and Figure 4.2). The monometallic Ru catalyst showed a low-temperature peak between 60 and 80 °C, suggestive of amorphous RuO₂ reduction,¹⁶⁸ as well as a smaller reduction peak between 180 and 220 °C, suggestive of bulk RuO₂ reduction. At temperatures above 250 °C, the onset of a broad peak is observed that is suggestive of autoreduction or CO and CO₂ evolution from the support, as noted above.¹⁶⁹

Table 4.2 Properties of fresh powder bimetallic catalysts used in batch screening reactions for succinic acid reduction to BDO.

Catalyst (~wt. ratio)	ICP (wt.%)	H ₂ uptake ($\mu\text{mol g}^{-1}$)	CO uptake ($\mu\text{mol g}^{-1}$)
Ru-Sn/PAC (1:1)	4.8% Ru 4.1% Sn	4.3 ^a	5.9 ^c
Pt-Sn/PAC (1:1)	5.1% Pt 3.9% Sn	0.3 ^a	Not measured
Pd-Re/PAC (1:1)	4.5% Pd 3.7% Re	456 ^b	Not measured

^aMeasured by H₂ TPD; ^bMeasured by H₂-O₂ titration; ^cMeasured by CO pulse.

For the Ru-Sn (1:1) catalyst, a low-temperature reduction peak during TPR was observed between 50 and 100 °C. The early onset peak (< 100 °C) was attributed to the reduction of surface Ru, while the late onset peak (> 400 °C) was attributed to auto-reduction or the evolution of CO and CO₂ the nitric acid-treated activated carbon support. As a control, the catalyst was heated under inert flow gas to confirm the identity of early onset peaks as reduction events.

In comparison to other Ru-Sn bimetallic systems, reduction peaks were not observed between 250 and 350 °C,¹⁷⁰⁻¹⁷³ suggesting significant Sn surface enrichment of Ru sites that influences H₂ uptake. At high temperatures above 400 °C, a broad low-magnitude peak was observed (Figure 4.2), potentially due to the reduction of oxygenated functional groups on the support or reduction of SnO₂.¹⁷⁴

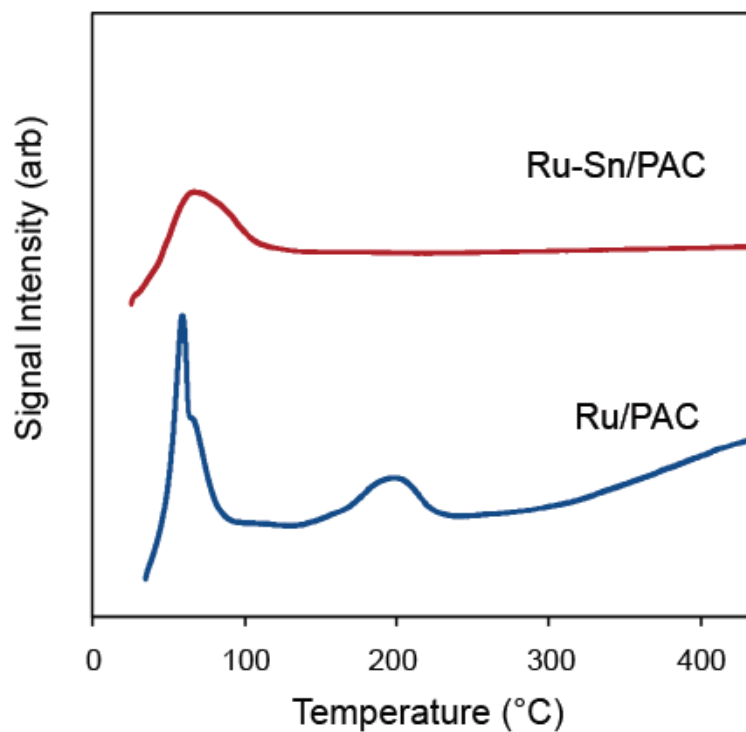


Figure 4.1 Characterization of the Ru-Sn (1:1) and Ru powder activated carbon catalysts by temperature-programmed reduction.

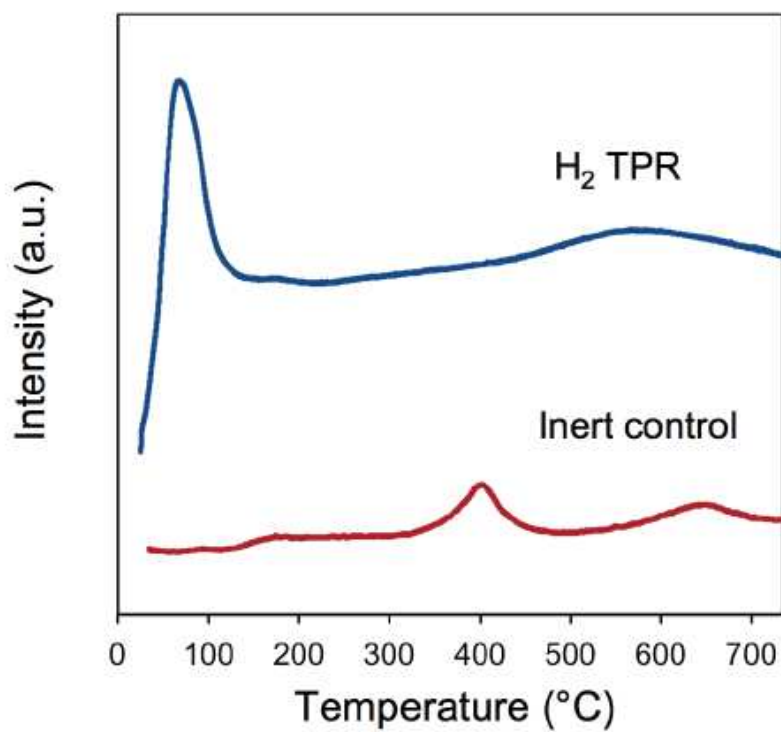


Figure 4.2 High temperature TPR profile of Ru-Sn/PAC and inert control.

4.5 Conclusion

As demonstrated in this work, bimetallic Ru-Sn/GAC can facilitate the continuous aqueous-phase reduction of succinic acid to BDO in high yields for prolonged time on stream. The addition of Sn to Ru dramatically affects the catalyst affinity for H₂ and CO, resulting in negligible uptake by chemisorption. TPR suggested the lack of a surface Ru-Sn alloy, while high-resolution STEM-EDS confirmed the collocation of Ru and Sn. XPS analysis following reduction confirmed the presence of partially oxidized Ru-Sn, which may be responsible for surface acidity that promotes GBL ring opening. However, further work is needed to understand the nature of the active site after synthesis and under operando conditions, which will be addressed in future studies. With prolonged exposure to reaction conditions in a trickle bed reactor, leaching of stainless steel resulted in catalyst metal crystallite restructuring to form Ni-Sn species. Computational modeling confirmed favorable energetics for Ru-Sn segregation and Ni-Sn formation at submonolayer Sn incorporation, highlighting potential driving forces for Sn migration from Ru-Sn to Ni particles. To address reactor leaching, the reactor tube was coated with an inert silica layer by CVD. After silica coating, stainless steel leaching was greatly reduced, and the Ru-Sn catalyst displayed stable performance with an activation energy of 62.2 MJ kg⁻¹ under partial conversion conditions (WHSV of 4 h⁻¹). Reducing the WHSV to 0.06 h⁻¹ resulted in complete conversion of succinic acid and a major molar product distribution of 71% BDO and 15% THF. These results highlight the potential of Ru-Sn/AC as a bimetallic catalyst for converting succinic acid to BDO, while underscoring the need for chemically compatible reactor metallurgy and catalyst active site design for continuous processing.

4.6 Author Information

*E-mail for D.R.V.: derek.vardon@nrel.gov.

4.7 Acknowledgements

We thank the U.S. Department of Energy (DOE) Bioenergy Technologies Office for funding this work via Contract No. DE-AC36-08GO28308 at the National Renewable Energy Laboratory. In addition, this work was performed in collaboration with the Chemical Catalysis for Bioenergy Consortium (ChemCatBio), a member of the Energy Materials Network (EMN), and was supported by the DOE Bioenergy Technologies Office under Contract No. DE-AC05-00OR22725 with the ORNL and Contract No. DE-AC36-08-GO28308 with the NREL. STEM experiments were performed using instrumentation (FEI Talos F200X STEM) provided by the DOE, Office of Nuclear Energy, Fuel Cycle R&D Program, and the Nuclear Science User Facilities. The computational work was supported in part by the Consortium for Computational Physics and Chemistry funded by the DOE's Bioenergy Technologies Office (DE-AC36-08GO28308). The authors are grateful for supercomputer time on Stampede provided by the Texas Advanced Computing Center (TACC) under the National Science Foundation Extreme Science and Engineering Discovery Grant MCB09159 and the NREL Computational Sciences Center, which is supported by the DOE Office of Energy Efficiency and Renewable Energy under Contract No. DE-AC36-08GO28308. Support for K.X.S. was provided by the NREL's intellectual property licensing program. We also thank Glenn Teeter at the NREL for his assistance with XPS analysis. The U.S. Government retains and the publisher, by accepting the article for publication, acknowledges that the U.S. Government retains a nonexclusive, paid up, irrevocable, worldwide license to publish or reproduce the published form of this work, or allow others to do so, for U.S. Government purposes.

CHAPTER 5

CIS,CIS-MUCONIC ACID: SEPARATION AND CATALYSIS TO BIO-ADIPIC ACID FOR NYLON-6,6 POLYMERIZATION

Reprinted in part from a paper published in *Green Chemistry*¹

Derek R. Vardon,^{†,2} Nicholas A. Rorrer,^{2,3} Davinia Salvachúa,² Amy E. Settle,²

Christopher W. Johnson,² Martin J. Menart,² Nicholas S. Cleveland,² Peter N. Ciesielski,⁴ K.

Xerxes Steirer,⁵ John R. Dorgan³ and Gregg T. Beckham^{*,2}

5.1 Abstract

cis,cis-Muconic acid is a polyunsaturated dicarboxylic acid that can be produced renewably *via* the biological conversion of sugars and lignin-derived aromatic compounds. Subsequently, muconic acid can be catalytically converted to adipic acid – the most

¹ Reprinted with permission from DOI: [10.1039/c5gc02844b](https://doi.org/10.1039/c5gc02844b) (article) *Green Chem.*, 2016, 18, 3397-3413. Copyright 2016 Royal Society of Chemistry.

² National Bioenergy Center, National Renewable Energy Laboratory, Golden, CO 80401, USA.

³ Department of Chemical and Biological Engineering, Colorado School of Mines, Golden, CO 80401, USA.

⁴ Biosciences Center, National Renewable Energy Laboratory, Golden, CO 80401, USA.

⁵ Interfacial and Surface Science, National Renewable Energy Laboratory, 15013 Denver West Parkway, Golden, CO 80401.

[†] Primary researcher and corresponding author.

[‡] Performed all chemisorption experiments and analysis.

* Corresponding author.

commercially significant dicarboxylic acid manufactured from petroleum. Nylon-6,6 is the major industrial application for adipic acid, consuming 85% of market demand; however, high purity adipic acid (99.8%) is required for polymer synthesis. As such, process technologies are needed to effectively separate and catalytically transform biologically derived muconic acid to adipic acid in high purity over stable catalytic materials. To that end, this study: (1) demonstrates bioreactor production of muconate at 34.5 g L^{-1} in an engineered strain of *Pseudomonas putida* KT2440, (2) examines the staged recovery of muconic acid from culture media, (3) screens platinum group metals (e.g., Pd, Pt, Rh, Ru) for activity and leaching stability on activated carbon (AC) and silica supports, (4) evaluates the time-on-stream performance of Rh/AC in a trickle bed reactor, and (5) demonstrates the polymerization of bio-adipic acid to nylon-6,6. Separation experiments confirmed AC effectively removed broth color compounds, but subsequent pH/temperature shift crystallization resulted in significant levels of Na, P, K, S and N in the crystallized product. Ethanol dissolution of muconic acid precipitated bulk salts, achieving a purity of 99.8%. Batch catalysis screening reactions determined that Rh and Pd were both highly active compared to Pt and Ru, but Pd leached significantly (1–9%) from both AC and silica supports. Testing of Rh/AC in a continuous trickle bed reactor for 100 h confirmed stable performance after 24 h, although organic adsorption resulted in reduced steady-state activity. Lastly, polymerization of bio-adipic acid with hexamethyldiamine produced nylon-6,6 with comparable properties to its petrochemical counterpart, thereby demonstrating a path towards bio-based nylon production *via* muconic acid.

5.2 Catalyst Synthesis

Platinum group metal catalysts (Pt, Rh, Ru, Pd) were synthesized on powder carbon and silica supports to evaluate their activity and stability for muconic acid hydrogenation. For batch

reaction studies, Darco activated carbon (Sigma Aldrich) and Davisil Grade 633 high surface area silica (Sigma Aldrich) were used. Supports were initially sieved >270 mesh (<53 μm) to minimize the impact of mass transfer on observed kinetics. The silica support was calcined at 500 °C in air prior to loading metals, while the activated carbon support was used as received. Catalysts were prepared with the following metal salt precursors: palladium acetate (Sigma Aldrich), rhodium nitrate hydrate (Sigma Aldrich), ruthenium chloride hydrate (Sigma Aldrich), chloroplatinic acid (CPA) (Sigma Aldrich), and ammonium tetraammineplatinum nitrate (PTA) (Sigma Aldrich). Pd, Ru, and Rh catalysts were prepared by incipient wetness, while Pt catalysts were prepared by strong electrostatic adsorption (SEA) to improve dispersion due to the low activity. For SEA catalyst synthesis,¹⁷⁵⁻¹⁷⁶ 1.9 g of support was added to 50 mL of DI water, and the pH was adjusted to facilitate protonation/deprotonation of the support (pH 12 with NaOH for silica, pH 2.9 with HCl for AC). In another bottle, the appropriate catalyst precursor was dissolved in 50 mL of DI water (PTA for silica, CPA for activated carbon). The two bottles were mixed together with stirring for 1 h, followed by vacuum filtration to recover the catalyst. The catalyst was washed twice with 50 mL of DI water and left to dry overnight in air at room temperature. After loading, catalysts were dried at 110 °C and reduced in hydrogen flowing at 200 sccm for 2 h at temperature. Due to the sensitivity of Pd dispersion with temperature,¹⁶⁵ Pd catalysts were reduced at 125 °C while Pt, Rh, and Ru catalysts were reduced at 250 °C. For flow reactor time-on-stream stability experiments, extruded activated carbon pellets (Norit Rx 3 Extra, Cabot Norit) were initially crushed and sieved between 80–100 mesh (150–180 μm) to allow for a moderate catalyst bed pressure drop (<5 psig). Rh was loaded onto the support by incipient wetness using rhodium nitrate hydrate (Sigma Aldrich), dried at 110 °C, and reduced *ex situ* prior to use at 250 °C in flowing hydrogen.

Batch reactor catalyst screening experiments were conducted with platinum group metals to evaluate their activity and stability against leaching during muconic acid hydrogenation. Catalysts were synthesized using powdered Darco activated carbon (AC) and Davisil silica supports sieved to >270 mesh (<53 μm) to minimize the impact of mass transfer during batch conditions previously studied.¹⁷⁷ Metal precursors were loaded onto their respective supports, and catalysts were reduced in hydrogen prior to characterization for determination of their metal loading and dispersion, support surface area, pore volume and pore diameter, and X-ray diffraction (XRD) spectra.

5.3 Chemisorption Methods

Chemisorption was used to evaluate crystallite metal dispersion, defined as the percentage of metal surface sites compared to the total metal loaded. Analysis was performed on an Autochem II 2920 chemisorption instrument (Micromeritics). The metal surface area of platinum and rhodium was determined by CO pulse chemisorption (10% CO/He, 25 sccm). A stoichiometry of one CO molecule per surface metal atom was assumed. For palladium, a hydrogen–oxygen titration was performed (10% H₂/Ar, 10% O₂/He, 25 sccm). Ruthenium metal surface area was measured by H₂ temperature-programmed desorption (TPD) in flowing Ar (25 sccm). The samples were ramped to 500 °C at 10 °C min⁻¹. For reductive pretreatment, samples were ramped to 250 °C at 2 °C min⁻¹ under flowing 10% H₂/Ar (20 sccm) and held for 2 h. Samples were then purged for 1 h under flowing He or Ar (20 sccm) before cooling to 40 °C for CO pulse chemisorption and hydrogen–oxygen titration. The inert purge for H₂-TPD was performed at 40 °C.

5.4 Chemisorption Results

Metal dispersions for the catalysts prepared for batch studies on AC and SiO₂ supports were within the range of 10–62% (Table 5.1), likely due to differing metal precursor and support material interactions during synthesis.¹⁶⁴ Due to varying active metal crystallite surface areas, observed catalyst activities for muconic acid hydrogenation were normalized to dispersion values to allow for turn-over-frequency (TOF) comparisons between metals (i.e., moles of compound reacted per second, divided by the moles of surface metal atoms measured by dispersion).

Table 5.1 Metal dispersion based on chemisorption and metal content determined by ICP for the virgin activated carbon (AC) and silica powdered catalysts used in batch screening reactions for muconic acid hydrogenation.

Catalyst (nominal)	Dispersion
1% Pd/AC	13
1% Rh/AC	69
5% Ru/AC	10
5% Pt/AC	60
1% Pd/AC	28
1% Rh/AC	62
1% Ru/SiO ₂	17
5% Pt/SiO ₂	47

Based on the activity and stability of Rh during batch reactions, the time-on-stream performance of a 1% Rh/AC granular catalyst was evaluated for 100 h in a trickle bed reactor. The 1% Rh catalyst was prepared on 150–180 μm activated carbon granules (100–80 mesh) to minimize the catalyst bed pressure drop. Methods for metal loading and pretreatment of the catalyst were identical to the powder catalyst used in the batch study.

The metal crystallite dispersion of the granule 1% Rh/AC catalyst was reduced (40%) compared to the powder catalyst (69%), likely due to differing support-precursor interactions

during incipient wetness impregnation. Measurements of the catalyst metal surface area by CO chemisorption after the reaction (Table 5.2) showed a 60% decrease in metal surface area (16% dispersion) when compared to fresh catalyst (40% dispersion).

Table 5.2 Metal content and dispersion of the fresh and post-reaction 1% Rh/AC granule catalyst used in the 100 h time-on-stream stability test for muconic acid hydrogenation.

Catalyst (nominal)	ICP (wt.%)	Dispersion (%)
Fresh 1% Rh/AC	1.0	40
Spent 1% Rh/AC	0.9	16

5.5 Conclusion

As demonstrated in this work, muconic acid can serve as a biologically derived precursor for high purity adipic acid and nylon-6,6 polymerization through downstream separation and catalysis. In addition to fuels, the production of value-added chemicals from biomass holds promise for improving the economic and environmental outlook of modern biorefineries. However, effective strategies are needed to remove problematic impurities generated during biomass depolymerization and biological conversion, while meeting the stringent purity requirements for renewable polymer precursor production through integrated biological conversion, separation, and catalytic unit processes. Moreover, robust catalytic materials are needed to mitigate leaching and organic fouling from bioderived substrates to alleviate upstream separation demands, while still achieving the desired catalytic activity and selectivity with biomass-derived substrates.

5.6 Author Information

*E-mail for D.R.V.: Derek.Vardon@nrel.gov.

*Email for G.T.B.: Gregg.Beckham@nrel.gov.

5.7 Acknowledgements

We thank the US Department of Energy Bioenergy Technologies Office for funding the biological and batch catalysis sections of this work. Support for NAR is provided by the U.S. Department of Energy, Office of Science, Office of Workforce Development for Teachers and Scientists, Office of Science Graduate Student Research (SCGSR) program. The SCGSR program is administered by the Oak Ridge Institute for Science and Education for the DOE under contract number DE-AC05-06OR23100. Efforts for the flow catalysis and stability section were funded by the Direct Catalytic Conversion of Biomass to Biofuels (C3Bio), an Energy Frontier Research Center funded by the U.S. Department of Energy, Office of Science, Office of Basic Energy Sciences, Award Number DE-SC0000997. Support for KXS was provided by proceeds from NREL's intellectual property licensing program. We would like to thank Todd Vander Wall for help with fed-batch biological conversion runs and Bill Michener for help with analytics. We would also like to thank Susan Habas for assistance with TEM.

CHAPTER 6

DEACTIVATION OF MULTILAYERED MFI NANOSHEET ZEOLITE DURING UPGRADING OF BIOMASS PYROLYSIS VAPORS

Reprinted in part from a paper in *ACS Sustainable Chemistry & Engineering*¹

Mengze Xu,^{†,1,2} Calvin Mukarakate,^{*,2} Kristiina Iisa,² Sridhar Budhi,^{1,2} Martin Menart,¹
Malcolm Davidson,¹ David J. Robichaud,² Mark R. Nimlos,² Brian G. Trewyn,¹ and Ryan M.
Richards^{*,1,2}

6.1 Abstract

The catalytic fast pyrolysis (CFP) of biomass is a promising technology for producing renewable transportation fuels and chemicals. MFI-type catalysts have shown promise for CFP because they produce gasoline range hydrocarbons from oxygenated pyrolysis compounds; however, rapid catalyst deactivation due to coking is one of the major technical barriers inhibiting the commercialization of this technology. Coke deposited on the surface of the catalysts blocks access to active sites in the micropores leading to rapid catalyst deactivation.

¹ Reprinted with permission from DOI: [10.1021/acssuschemeng.7b00817](https://doi.org/10.1021/acssuschemeng.7b00817) (article), *ACS*

Sustainable Chem. Eng. 2017, 5, 5477-5484. Copyright 2017 American Chemical Society.

² Department of Chemistry, Colorado School of Mines, Golden, Colorado 80401, United States

³ National Renewable Energy Laboratory, 15523 Denver West Parkway, Golden, Colorado 80401, United States

[†] Primary researcher.

[‡] Performed all DRIFTS experiments and analysis and contributed to chemisorption experiments.

* Corresponding authors.

Our strategy is to minimize rapid catalyst deactivation by adding mesoporosity through formation of MFI nanosheet materials. The synthesized MFI nanosheet catalysts were fully characterized and evaluated for cellulose pyrolysis vapor upgrading to produce olefins and aromatic hydrocarbons. The data obtained from pyrolysis-GCMS (py-GCMS) showed that fresh MFI nanosheets produced similar aromatic hydrocarbon and olefin yields compared to those of conventional HZSM-5. However, MFI nanosheets demonstrated a longer lifetime than HZSM-5 even though coke contents were also higher than those for HZSM-5 because the mesopores enabled better accessibility to active acid sites. This conclusion was supported by results from postreaction analysis of various spent catalysts collected at different points during the deactivation experiments.

6.2 Chemisorption and DRIFTS Methods

Total amounts of acid sites and were measured using a Micromeritics Autochem 2920 instrument. Approximately 100 mg samples were loaded in a U-shape quartz tube. Samples were preheated to 550 °C for 30 min and cooled to 120 °C under He flow. A mixed flow of 10 % NH₃/He was dosed on the samples at 120 °C for 10 min during which the adsorption process occurred. Subsequently, the carrier gas, He, was flushed at 120 °C for 90 min to remove physisorbed ammonia. The desorption process was performed by heating to 550 °C at a ramp rate of 20 °C·min⁻¹ and measured with a thermal conductivity detector (TCD). A standard profile of known ammonia volume was used to calibrate TCD signals and quantify the amount of ammonia desorbed from the samples. The relative amounts of Brønsted and Lewis acid sites were determined using pyridine adsorption diffuse-reflectance FT-IR spectroscopy (py-DRIFTS). Spectra were recorded at a resolution of 4 cm⁻¹ on a Thermo Nicolet iS50 FT-IR spectrometer equipped with a Harrick Praying Mantis reaction chamber and CaF windows.

Samples were loaded into the chamber and pretreated in flowing N₂ (100 mL min⁻¹) at 200 °C for 3 h. After cooling to 150 °C, samples were purged with N₂ for 0.5 h, and pyridine vapor was introduced. After 5 min of pyridine exposure, the samples were heated to 200 °C and held for 1 h under flowing N₂ to remove excess and/or physisorbed pyridine. The adsorption bands⁸¹ near 1454 cm⁻¹ (Lewis) and 1545 cm⁻¹ (Brønsted) and their relative adsorption coefficients ($\epsilon_B/\epsilon_L = 0.76$)⁸² were used to determine the relative Brønsted/Lewis acid site ratios.

6.3 Results

By comparison of the breakthrough time for primary pyrolysis vapors as a function of cellulose doses, it was determined that HZSM-5 deactivated faster than the MFI nanosheet, despite having a higher density of acid sites (Table 6.1). This indicates that more active sites were accessible for the MFI nanosheet compared to the HZSM-5 catalyst despite having fewer initial acid sites and a lower Brønsted to Lewis ratio. These results emphasized the importance of active site accessibility for extending catalyst lifetime.

Table 6.1 Quantified acid sites and Brønsted to Lewis ratios of fresh and recovered MFI nanosheet and HZSM-5 samples after exposure to 5, 25, and 50 doses of cellulose during MBMS experiments.

Cellulose doses	Total acid sites ^a ($\mu\text{mol g}^{-1}$)		Brønsted/Lewis ratio ^b	
	MFI nanosheet	HZSM-5	MFI nanosheet	HZSM-5
Fresh	269	320	4.76	9.40
5	147	144	3.88	Not measured ^c
25	103	121	0.31	4.79
50	5	4	N/A ^d	N/A ^c

^aDetermined by NH₃ TPD; ^bDetermined by pyridine-DRIFTS; ^cInsufficient sample recovered for measurement; ^dInsufficient signal due to coking of acid sites.

6.4 Conclusion

In conclusion, the introduced mesoporosity was found to have effects on both catalyst lifetime and coke formation. During the deactivation process in CFP of cellulose, MFI nanosheets exhibited unique activities compared to those of HZSM-5 with comparable texture properties. The introduced mesopores provided better accessibility to active acid sites so that the MFI nanosheet displayed longer lifetimes than HZSM-5 but formed coke. Additional research will be conducted in the future to carefully optimize the mesopore diameters to allow coke precursors to escape the pores before forming coke and modify the acid sites in mesopores to promote the formation of hydrocarbons.

6.5 Author Information

*(C.M.) E-mail: calvin.mukarakate@nrel.gov.

*(R.M.R.) E-mail: rrichard@mines.edu.

6.6 Acknowledgements

This work was performed in collaboration with the Chemical Catalysis for Bioenergy Consortium, an Energy Materials Network Consortium funded by the U.S. Department of Energy's Bioenergy Technologies Contract No. DE-AC36-08GO28308 with the National Renewable Energy Laboratory. We thank Professor Don L. Williamson for assistance with SAXS and Professor David Diercks for support with HRTEM.

CHAPTER 7

SUMMARY, CONCLUSIONS, AND FUTURE WORK

7.1 Summary and Conclusions

This work evaluated the material and catalytic properties of heterogeneous nickel-containing oligomerization catalysts. The primary goals were to determine the influence of support electron donor/acceptor properties and nickel-acid site interactions that resulted in the formation of active catalysts, and to demonstrate the oligomerization of a bio-derived light olefin stream containing ethylene and propylene to liquids. The series of supports studied included TiO₂, MgO, SiO₂, Al₂O₃, mesostructured silica alumina, and amorphous silica alumina. The supports lacking Brønsted acidity, MgO and TiO₂, were inactive and poorly active, respectively, for ethylene oligomerization. An amorphous silica alumina support possessing Brønsted and Lewis acidity, Davicat 3125 (denoted ASA₂₅), was down-selected for detailed catalytic studies based on cost, commercial-availability, and performance.

A set of Ni/ASAs were prepared by ion exchange under varying synthesis conditions. The variables of reflux duration and concentration of nickel precursor had a weak and moderate effects on nickel content and Lewis acidity, respectively. The Ni-free support was active for propylene oligomerization through a Brønsted-catalyzed pathway but inactive for ethylene conversion. Nickel addition improved the conversion of propylene and enabled ethylene activation. The Lewis site density of the Ni-containing catalysts was well correlated with ethylene conversion. However, no correlation between Brønsted acidity and either ethylene or propylene conversion was found.

Further exchange of the Ni-containing samples with sodium had no effect on Brønsted acidity but reduced the nickel content and Lewis acidity of the catalysts. The catalytic activity was consequently reduced towards both ethylene and propylene by Na-addition. The content of reducible nickel oxide on the catalysts was a more accurate predictor of catalytic activity than the total nickel content estimated by elemental analysis, suggesting that non-reducible, inactive nickel species were also present on the catalysts. The reduction events occurred at higher temperatures than bulk nickel oxide in regions comparable to nickel phyllosilicates and nickel on alumina which indicated a strong interaction between the nickel oxide-like phase and the support. Altogether, the presence of catalytic activity resulted from the formation of reducible, Lewis acidic nickel sites on the support.

A comparison of two ASA supports having different aluminum content found their interactions with nickel to be substantially different. Upon nickel incorporation, Brønsted sites were more readily exchanged on ASA₁₅, while a greater number of Lewis sites were created on the more aluminum-rich ASA₂₅. The nickel species on Ni/ASA₂₅ were found to be more reducible in TPR experiments than those on Ni/ASA₁₅. The XPS binding energy for the primary Ni 2p_{3/2} peak appeared at 856.0 eV on both supports, consistent with an electronic environment similar to that of Ni(OH)₂. In total, the incorporation of nickel on ASA₂₅ produced more reducible nickel species, introduced greater Lewis acidity, and had a lower impact on Brønsted acidity than on ASA₁₅.

The coordination of aluminum in ASA₂₅ was impacted by both nickel incorporation and thermal pretreatment. The thermal removal of water from the support reduced the intensity of predominantly 6-coordinate species in ²⁷Al MAS NMR. Upon nickel incorporation, 5-coordinate Al was generated at the expense of 4- and 6- coordinate species. These results evidence a pliable

network of aluminum in ASA₂₅ that responds coordinatively to the presence of surface species. The generated 5-coordinate Al species are proposed to abridge nickel oxide-like phases to the support, in analogy to reports of 5-coordinate Al that adjoin the interfacial regions of silica- and alumina-rich domains in ASAs.¹⁰⁵

The electrophility and coordinative environment of incorporated nickel were probed by low temperature CO DRIFTS and *in situ* XAS experiments. The shifts in CO infrared stretch position were consistent with nickel Lewis sites having an electrophilicity intermediate to nickel cations on zeolites and bulk nickel oxides. The XAS spectra, pre-edge features, and Ni-O distances fitted from EXAFS of Ni/ASA and Ni/Al-MCM-41 were very close matches to the 5-coordinate Ni model compound, KNiPO₄. The XAS features of the less active catalysts Ni/Al₂O₃ and Ni/SiO₂ were more characteristic of 6-coordinate bulk NiO.

The exposure of Ni/ASA catalysts to gas phase CO and ethylene resulted in changes to the local environment of nickel. The coordination number of nickel in the pretreated catalysts did not vary after exposure to ethylene regardless of the support material. However, perturbations in the EXAFS fits of the more active materials suggested changes in the local environment of nickel. In CO DRIFTS experiments on Ni/ASA₂₅, a reduction in terminal silanol stretches was observed upon exposure to CO that occurred without corresponding observation of CO-silanol interactions. These results are concluded to describe the active nickel sites on Ni/ASA₂₅ as 5-coordinate species having hemilabile support interactions. Upon coordination of nickel to a strongly binding gas phase species, such as CO or ethylene, a nickel-support bond dissociates, and the resulting charge becomes stabilized by adjacent support atoms. These hemilabile bond exchanges are proposed to be facilitated by interactions between nickel, terminal silanols, and coordinatively-flexible aluminum sites in ASA.

7.2 Future Work

Ni/ASAs are promising catalysts for the oligomerization of light olefins. They are readily prepared and utilized, possess high activity towards ethylene and propylene, and are made from earth-abundant, cost-effective, and commercially-available materials. Although simple to prepare, Ni/ASAs contain complex speciations of nickel, silicon, and aluminum. The interactions of these phases appear unlike that of the well-studied transition metal-acid site interactions in zeolites. Consequently, these materials require their own avenues of research. The structural and coordinative evolution of these phases in response to nickel incorporation, pretreatment, and olefin exposure occludes understanding of the structural origins of their activity and warrants deeper study, especially by *in situ* and *operando* techniques that characterize working catalysts.

Based on the results of this work, there are several areas that warrant future investigation: (1) selective poisoning experiments during mixed olefin oligomerization, (2) catalytic comparison of Ni/ASA₁₅ and Ni/ASA₂₅, (3) the effect of reductive pretreatment temperature on activity and nickel speciation, (4) analysis of mixed 4- and 6-coordinate model compounds by XAS, (5) *in situ* DRIFTS experiments in the presence of ethylene and CO, (6) silicon characterization by ²⁹Si MAS NMR, and (7) electron paramagnetic resonance (EPR) experiments.

Regarding (1), experiments in this work showed that nickel activated both ethylene and propylene for oligomerization. The selective poisoning of nickel sites by CO is needed to determine the relative contributions of nickel and support Brønsted acidity for propylene oligomerization. A recent study has shown the activation of ethylene by Ni/Al-MCM-41 to be poisoned by both CO and a non-coordinating, bulky base, 2,6-di-*tert*-butylpyridine. The deactivation by base was concluded to occur by deprotonation of the proposed active site, a

hydroxylated Ni²⁺ monomer anchored to an exchanged Brønsted support site.¹⁷⁸ The results of this work neither confirm nor deny the presence of such an active site, and the presence of a hydroxyl group must be further considered as a potential component of the hemilabile site proposed here.

In Chapter 3, the material properties of Ni/ASA₁₅ and Ni/ASA₂₅ were shown to differ strongly in terms of nickel's effect on acidity and the reducibility of nickel oxide phases. Initial experiments performed at low ethylene conversion suggested substantial differences in the turnover frequency of nickel sites and isomerization of products obtained over these two catalysts. However, hardware issues during the experiments prevented conclusive interpretation, and these experiments must be repeated. The structural nature of reducible Ni phases must also be characterized by direct observation with transmission electron microscopy.

Reducible nickel content was found to be a more accurate predictor of catalytic activity than total nickel content. Catalytic experiments must be performed that examine the effect of reductive pretreatment temperature to determine the catalytic contributions of nickel having varying degrees of reducibility. To then construct a completed picture of structure-property-performance relations for these materials, analagous reductive pretreatments prior to CO DRIFTS and acid site measurements by NH₃ TPD and pyridine DRIFTS need be performed to relate the material properties of reducibility, electrophilicity, and acidity to catalytic properties.

For (3), the observation of terminal silanol interactions during CO DRIFTS experiments evidenced a restructuring of the support as nickel coordinated with CO. This conclusion is hypothesized to extend to interactions with ethylene, as CO and ethylene are both known to bind strongly and competitively with nickel cations.⁴⁶ To address this, DRIFTS experiments must be performed in the presence of ethylene as changes in the hydroxyl region are monitored.

In Chapter 2, the Ni^{II} species in active catalysts were shown by XAS to exhibit highly similar characteristics to the 5-coordinate model compound KNiPO₄. As XAS is a bulk technique, mixtures of 4- and 6-coordinate species can result in pre-edge features and Ni-O bond distances intermediate of one another, such that a 50:50 mixture resembles a 5-coordinate compound.¹⁰⁶ However, the EXAFS fits of mixed compounds exhibit higher Debye-Waller factors, in accordance with the “disorder” introduced by the fitting of two phases, and can be differentiated thusly.¹⁰⁶ To address this possibility in Ni/ASA materials, further experiments are planned to evaluate such a mixture of 4- and 6-coordinate Ni compounds to compare Debye-Waller terms to the Ni/ASA and Ni/Al-MCM-41 catalysts.

This work has focused efforts on the characterization of nickel and aluminum to draw structure-property-performance relations in Ni/ASA catalysts. The last main component of these materials, silicon, must be evaluated by ²⁹Si MAS NMR to assess if coordinative changes arise in silicon from the incorporation of nickel, thermal pretreatment, and exposure to olefins. Special sample preparation procedures would be required to encapsulate the pretreated and CO-exposed samples in the MAS sample rotor without further exposure to air.

Finally, ²⁷Al MAS NMR experiments showed a redistribution of aluminum coordinations in the ASA support upon nickel incorporation. Depending on pretreatment, paramagnetic Ni^I is known to form in these materials³⁸ and would be expected to interfere with the NMR signal. Consequently, EPR experiments must be performed on the Ni/ASA catalyst studied in this work to confirm the presence or absence of Ni^I species and ground interpretation of the ²⁷Al MAS NMR results.

REFERENCES

1. Giebelhaus, A. W., Encyclopedia of Energy. *Elsevier* **2004**, 4.
2. Klass, D. L., Biomass for Renewable Energy, Fuels and Chemicals. *Academic Press: San Diego* **1998**.
3. Perlack, R. D.; Wright, L. L.; Turhollow, A. F.; Graham, R. L.; Stokes, B. J.; Erbach, D. C. *Biomass as Feedstock for a Bioenergy and Bioproducts Industry: The Technical Feasibility of a Billion-Ton Annual Supply*; Oak Ridge National Laboratory: Oak Ridge, TN, 2005.
4. *Technology Roadmap: Biofuels for Transport*; International Energy Agency: Paris, France, 2011.
5. Crude oil and petroleum products supplied. U.S. Energy Information Administration: Washington D.C., 2015.
6. *Energy Information Administration Annual Outlook 2015*; U.S. Department of Energy: Washington, D.C., 2015.
7. *International Energy Outlook 2014*; U.S. Energy Information Administration: Washington D.C., 2014.
8. Directive 2009/28/EC. European Parliament and of the Council, 2009.
9. Directive 2009/30/EC. European Parliament and of the Council, 2009.
10. Energy Independence and Security Act of 2007. United States, 2007.
11. Wang, M.; Wu, M.; Huo, H., Life-cycle energy and greenhouse gas emission impacts of different corn ethanol plant types. *Environmental Research Letters* **2007**, 2.
12. McCormick, R. L.; Ratcliff, M. A.; Christensen, E.; Fouts, L.; Luecke, J.; Chupka, G. M.; Yanowitz, J.; Tian, M.; Boot, M., Properties of oxygenates found in upgraded biomass pyrolysis oil as components of spark and compression ignition engine fuels. *Energy Fuels* **2015**, 29, 2453-2461.
13. Christensen, E.; Chupka, G.; Luecke, J.; Alleman, T. L.; Iisa, K.; McCormick, R. L.; Franz, J. A.; Elliott, D. C., *Energy Fuels* **2011**, 25 (11), 5462-5471.
14. Talmadge, M. S.; Baldwin, R. M.; Bidy, M. J.; McCormick, R. L.; Beckham, G. T.; Ferguson, G. A.; Czernik, S.; Magrini-Bair, K. A.; Foust, T. D.; Metelski, P. D.; Hetrick, C.; Nimlos, M. R., A perspective on oxygenated species in the refinery integration of pyrolysis oil. *Green Chemistry* **2011**, 16, 407-453.

15. Climent, M. J.; Corma, A.; Iborra, S., Conversion of biomass platform molecules into fuel additives and liquid hydrocarbon fuels. *Green Chemistry* **2013**, *16*, 516-547.
16. Corma, A.; Torre, O. d. l.; Renz, M., Production of high quality diesel from cellulose and hemicellulose by the Sylvan process: catalysts and process variables. *Energy & Environmental Science* **2012**, *5*, 6328-6344.
17. T. N. Pham, D. S., D. E. Resasco, *Applied Catalysis B: Environmental* **2013**.
18. The Clean Air Act. United States, 2004.
19. *Waiver Requests Under Section 211(f) of the Clean Air Act*; United States Environmental Protection Agency: Washington, D.C., 2013.
20. D975 - Standard Specification for Diesel Fuel Oils. ASTM International: West Conshohocken, PA, 2013.
21. D1655 - Standard Specification for Aviation Turbine Fuels. ASTM International: West Conshohocken, PA, 2013.
22. D7566 - Standard Specification for Aviation Turbine Fuel Containing Synthesized Hydrocarbons. ASTM International: West Conshohocken, PA, 2013.
23. Y. Cheng, J. J., J. Shi, W. Fan, G.W. Huber, *Angew. Chem.* **2012**, *124*, 1416-1419.
24. W. Shen, G. A. T., K.D. Hammond, R. Xing, F. Dogan, C.P. Grey, W.C. Conner Jr., S.M. Auerbach, G.W. Huber, 392. *Appl. Cat. A: Gen* **2011**, 57-68.
25. Ruddy, D. A.; Schaidle, J. A.; Ferrell III, J. R.; Wang, J.; Moens, L.; Hensley, J. E., Recent advances in heterogeneous catalysts for bio-oil upgrading via “ex situ catalytic fast pyrolysis”: catalyst development through the study of model compounds. *Green Chemistry* **2014**, *16* (2), 454-490.
26. Arcoumanis, C.; Bae, C.; Crookes, R.; Kinoshita, E., The potential of di-methyl ether (DME) as an alternative fuel for compression-ignition engines: a review. *Fuel* **2008**, *87* (7), 1014-1030.
27. Agarwal, A. K., Biofuels (alcohols and biodiesel) applications as fuels for internal combustion engines. *Progress in energy and combustion science* **2007**, *33* (3), 233-271.
28. Sawyer, R. F., *Environmental Health Perspectives Supplements* **1993**, *101*, 5-12.
29. P. Pepiot-Desjardins, H. P., R. Malhotra, S. Kirby, and A. Boehman, *Combustion and Flame* **2008**, *154*, 191-205.
30. Dutta, A.; Talmadge, M.; Hensley, J. E., *Process Design and Economics for Conversion of Lignocellulosic Biomass to Ethanol*. National Renewable Energy Laboratory: Golden, Colorado, 2011; Vol. NREL/TP-5100-10863

31. Dutta, A.; Talmadge, M.; Hensley, J.; Worley, M.; Dudgeon, D.; Barton, D.; Groenendijk, P.; Ferrari, D.; Stears, B.; Searcy, E.; Wright, C.; Hess, J. R., Techno-economics for conversion of lignocellulosic biomass to ethanol by indirect gasification and mixed alcohol synthesis. *Environmental Progress & Sustainable Energy* **2012**, *31* (2), 182-190.
32. Song, J.; Cheenkachorn, K.; Wang, J.; Perez, J.; Boehman, A. L.; Young, P. J.; Waller, F. J., Effect of Oxygenated Fuel on Combustion and Emissions in a Light-Duty Turbo Diesel Engine. *Energy & Fuels* **2002**, *16* (2), 294-301.
33. Nash, C., Catalyst Screening for Mixed Alcohol Dehydration. *FY15 Q2 progress milestone W.B.S. 2.3.1.305*.
34. Mokrani, T.; Scurrall, M., Gas conversion to liquid fuels and chemicals: the methanol route-catalysis and process development. *Catalysis Reviews* **2009**, *51*, 1-145.
35. Hensley, J. E.; Lovestead, T. M.; Christensen, E.; Dutta, A.; Bruno, T. J.; McCormick, R., Compositional Analysis and Advanced Distillation Curve for Mixed Alcohols Produced via Syngas on a K-CoMoS_x Catalyst. *Energy & Fuels* **2013**, *27* (6), 3246-3260.
36. Nash, C. P.; Ramanathan, A.; Ruddy, D. A.; Behl, M.; Gjersing, E.; Griffin, M.; Zhu, H.; Subramaniam, B.; Schaidle, J. A.; Hensley, J. E., Mixed alcohol dehydration over Brønsted and Lewis acidic catalysts. *Applied Catalysis A: General* **2016**, *510*, 110-124.
37. Corma, A.; Iborra, S., Oligomerization of Alkenes. In *Catalysts for Fine Chemical Synthesis*, Derouane, E. G., Ed. John Wiley & Sons, Ltd: New Jersey, 2006; pp 125-140.
38. Finiels, A.; Fajula, F.; Hulea, V., Nickel-based Solid Catalysts for Ethylene Oligomerization. *Catalysis Science & Technology* **2014**, *4*, 2412-2426.
39. Skupinska, J., Oligomerization of Alpha-olefins to Higher Oligomers. *Chemical Reviews* **1991**, *91* (4), 613-648.
40. Metzger, E. D.; Brozek, C. K.; Comito, R. J.; Dincă, M., Selective Dimerization of Ethylene to 1-Butene with a Porous Catalyst. *ACS Central Science* **2016**, *2* (3), 148-153.
41. de Souza, M. O.; Rodrigues, L. R.; Gauvin, R. M.; de Souza, R. F.; Pastore, H. O.; Gengembre, L.; Ruiz, J. A. C.; Gallo, J. M. R.; Milanesi, T. S.; Milani, M. A., Support effect in ethylene oligomerization mediated by heterogenized nickel catalysts. *Catalysis Communications* **2010**, *11* (7), 597-600.
42. Lallemand, M.; Rusu, O. A.; Dumitriu, E.; Finiels, A.; Fajula, F. o.; Hulea, V., NiMCM-36 and NiMCM-22 catalysts for the ethylene oligomerization: Effect of zeolite texture and nickel cations/acid sites ratio. *Applied Catalysis A: General* **2008**, *338*, 37-43.
43. Brogaard, R. Y.; Olsbye, U., Ethene Oligomerization in Ni-Containing Zeolites: Theoretical Discrimination of Reaction Mechanisms. *ACS Catalysis* **2016**, *6* (2), 1205-1214.

44. Sohn, J. R., Correlation between acidic properties of nickel catalysts and catalytic activities for ethylene dimerization and butene isomerization. *Catalysis Surveys from Asia* **2004**, *8* (4), 249-263.
45. Matsuda, T.; Miura, H.; Sugiyama, K.; Ohno, N.; Keino, S.; Kaise, A., Selectivity in ethylene dimerization over supported nickel oxide catalysts. *Journal of the Chemical Society, Faraday Transactions 1: Physical Chemistry in Condensed Phases* **1979**, *75* (0), 1513-1520.
46. Martínez, A.; Arribas, M. A.; Concepción, P.; Moussa, S., New bifunctional Ni–H-Beta catalysts for the heterogeneous oligomerization of ethylene. *Applied Catalysis A: General* **2013**, *467*, 509-518.
47. Martínez, A.; Arribas, M. A.; Moussa, S., Development of Bifunctional Ni-Based Catalysts for the Heterogeneous Oligomerization of Ethylene to Liquids. In *Small-Scale Gas to Liquid Fuel Synthesis*, CRC Press: 2015; pp 377-400.
48. Moussa, S.; Arribas, M. A.; Concepción, P.; Martínez, A., Heterogeneous oligomerization of ethylene to liquids on bifunctional Ni-based catalysts: The influence of support properties on nickel speciation and catalytic performance. *Catalysis Today* **2016**, *277*, Part 1, 78-88.
49. Lewis, J. D.; Van de Vyver, S.; Román-Leshkov, Y., Acid–Base Pairs in Lewis Acidic Zeolites Promote Direct Aldol Reactions by Soft Enolization. *Angewandte Chemie International Edition* **2015**, *54* (34), 9835-9838.
50. Delley, M. F.; Núñez-Zarur, F.; Conley, M. P.; Comas-Vives, A.; Siddiqi, G.; Norsic, S.; Monteil, V.; Safonova, O. V.; Copéret, C., Proton transfers are key elementary steps in ethylene polymerization on isolated chromium(III) silicates. *Proceedings of the National Academy of Sciences of the United States of America* **2014**, *111* (32), 11624-11629.
51. Hasanayn, F.; Achord, P.; Braunstein, P.; Magnier, H. J.; Krogh-Jespersen, K.; Goldman, A. S., Theoretical Structure–Reactivity Study of Ethylene Insertion into Nickel–Alkyl Bonds. A Kinetically Significant and Unanticipated Role of *trans* Influence in Determining Agostic Bond Strengths. *Organometallics* **2012**, *31* (13), 4680-4692.
52. Wichterlová, B.; Žilková, N.; Uvarova, E.; Čejka, J.; Sarv, P.; Paganini, C.; Lercher, J. A., Effect of Brønsted and Lewis sites in ferrierites on skeletal isomerization of n-butenes. *Applied Catalysis A: General* **1999**, *182* (2), 297-308.
53. Cai, T., Studies of a new alkene oligomerization catalyst derived from nickel sulfate. *Catalysis Today* **1999**, *51* (1), 153-160.
54. Penkova, A.; Dzwigaj, S.; Kefirov, R.; Hadjiivanov, K.; Che, M., Effect of the Preparation Method on the State of Nickel Ions in BEA Zeolites. A Study by Fourier Transform Infrared Spectroscopy of Adsorbed CO and NO, Temperature-Programmed Reduction, and X-Ray Diffraction. *The Journal of Physical Chemistry C* **2007**, *111* (24), 8623-8631.

55. Hadjiivanov, K.; Knözinger, H.; Mihaylov, M., FTIR Study of CO Adsorption on Ni-ZSM-5. *The Journal of Physical Chemistry B* **2002**, *106* (10), 2618-2624.
56. Bentaleb, F.; Che, M.; Dubreuil, A.-C.; Thomazeau, C.; Marceau, E., Influence of organic additives on the properties of impregnation solutions and on nickel oxide particle size for Ni/Al₂O₃ catalysts. *Catalysis Today* **2014**, *235*, 250-255.
57. Bentaleb, F.; Marceau, E., Influence of the textural properties of porous aluminas on the reducibility of Ni/Al₂O₃ catalysts. *Microporous and Mesoporous Materials* **2012**, *156*, 40-44.
58. de Bokx, P. K.; Wassenberg, W. B. A.; Geus, J. W., Interaction of nickel ions with a γ -Al₂O₃ support during deposition from aqueous solution. *Journal of Catalysis* **1987**, *104* (1), 86-98.
59. Mosqueda-Jiménez, B. I.; Jentys, A.; Seshan, K.; Lercher, J. A., Reduction of nitric oxide by propene and propane on Ni-exchanged mordenite. *Applied Catalysis B: Environmental* **2003**, *43* (2), 105-115.
60. Borfecchia, E.; Lomachenko, K. A.; Giordanino, F.; Falsig, H.; Beato, P.; Soldatov, A. V.; Bordiga, S.; Lamberti, C., Revisiting the nature of Cu sites in the activated Cu-SSZ-13 catalyst for SCR reaction. *Chemical Science* **2015**, *6* (1), 548-563.
61. Strömberg, S.; Svensson, M.; Zetterberg, K., Binding of ethylene to anionic, neutral, and cationic nickel (II), palladium (II), and platinum (II) cis/trans chloride ammonia complexes. A theoretical study. *Organometallics* **1997**, *16* (14), 3165-3168.
62. Carney, C. S.; Chinn, R. E.; Doğan, Ö. N.; Gao, M. C., Isothermal decomposition kinetics of nickel (II) hydroxide powder. *Journal of Alloys and Compounds* **2015**, *644*, 968-974.
63. Rascon, F.; Wischert, R.; Coperet, C., Molecular nature of support effects in single-site heterogeneous catalysts: silicav. alumina. *Chemical Science* **2011**, *2* (8), 1449-1456.
64. McDaniel, M. P.; Schwerdtfeger, E. D.; Jensen, M. D., The “comonomer effect” on chromium polymerization catalysts. *Journal of Catalysis* **2014**, *314*, 109-116.
65. Conant, J. B.; Kistiakowsky, G. B., Energy Changes Involved in the Addition Reactions of Unsaturated Hydrocarbons. *Chemical Reviews* **1937**, *20* (2), 181-194.
66. Corma, A.; Iborra, S., *Catalysts for Fine Chemical Synthesis, Vol. 4, Microporous and Mesoporous Solids*. John Wiley & Sons: New York, New York, 2006.
67. Deimund, M. A.; Labinger, J.; Davis, M. E., Nickel-Exchanged Zincosilicate Catalysts for the Oligomerization of Propylene. *ACS Catalysis* **2014**, *4* (11), 4189-4195.
68. Gan, S.-N.; Chen, S.-I.; Ohnishi, R.; Soga, K., Homo- and copolymerization of ethylene and propylene using a heterogeneous chromium catalyst system. *Polymer* **1987**, *28* (8), 1391-1395.

69. Tanaka, M.; Itadani, A.; Kuroda, Y.; Iwamoto, M., Effect of Pore Size and Nickel Content of Ni-MCM-41 on Catalytic Activity for Ethene Dimerization and Local Structures of Nickel Ions. *The Journal of Physical Chemistry C* **2012**, *116* (9), 5664-5672.
70. Nicholas, C. P., Applications of light olefin oligomerization to the production of fuels and chemicals. *Applied Catalysis A: General* **2017**, *543*, 82-97.
71. Ziegler, K.; Holzkamp, E.; Breil, H.; Martin, H., Das Mülheimer Normaldruck-Polyäthylen-Verfahren. *Angewandte Chemie* **1955**, *67* (19-20), 541-547.
72. Lallemand, M.; Finiels, A.; Fajula, F.; Hulea, V., Nature of the Active Sites in Ethylene Oligomerization Catalyzed by Ni-Containing Molecular Sieves: Chemical and IR Spectral Investigation. *The Journal of Physical Chemistry C* **2009**, *113* (47), 20360-20364.
73. Brückner, A.; Bentrup, U.; Zanthoff, H.; Maschmeyer, D., The role of different Ni sites in supported nickel catalysts for butene dimerization under industry-like conditions. *Journal of Catalysis* **2009**, *266* (1), 120-128.
74. Rabeah, J.; Radnik, J.; Briois, V.; Maschmeyer, D.; Stochniol, G.; Peitz, S.; Reeker, H.; La Fontaine, C.; Brückner, A., Tracing Active Sites in Supported Ni Catalysts during Butene Oligomerization by Operando Spectroscopy under Pressure. *ACS Catalysis* **2016**, *6* (12), 8224-8228.
75. Mlinar, A. N.; Baur, G. B.; Bong, G. G.; Getsoian, A. B.; Bell, A. T., Propene oligomerization over Ni-exchanged Na-X zeolites. *Journal of Catalysis* **2012**, *296*, 156-164.
76. Cai, T.; Cao, D.; Song, Z.; Li, L., Catalytic behavior of NiSO₄/γ-Al₂O₃ for ethene dimerization. *Applied Catalysis A: General* **1993**, *95* (2), L1-L7.
77. Hulea, V.; Fajula, F., Ni-exchanged AlMCM-41—An efficient bifunctional catalyst for ethylene oligomerization. *Journal of Catalysis* **2004**, *225* (1), 213-222.
78. Espinoza, R. L.; Snel, R.; Korf, C. J.; Nicolaidis, C. P., Catalytic oligomerization of ethene over nickel-exchanged amorphous silica-aluminas; effect of the acid strength of the support. *Applied Catalysis* **1987**, *29* (2), 295-303.
79. Suchomel, M. R.; Shoemaker, D. P.; Ribaud, L.; Kemei, M. C.; Seshadri, R., Spin-induced symmetry breaking in orbitally ordered NiCr₂O₄ and CuCr₂O₄. *Physical Review B* **2012**, *86* (5), 054406.
80. Trobajo, C.; Salvadó, M. A.; Pertierra, P.; Alfonso, B. F.; Blanco, J. A.; Khainakov, S. A.; García, J. R., Synthesis, Structure and Magnetic Characterization of Two Phosphate Compounds Related with the Mineral Struvite: KNiPO₄·μ₆H₂O and NaNiPO₄·μ₇H₂O. *Zeitschrift für anorganische und allgemeine Chemie* **2007**, *633* (11-12), 1932-1936.
81. Parry, E., An infrared study of pyridine adsorbed on acidic solids. Characterization of surface acidity. *Journal of Catalysis* **1963**, *2* (5), 371-379.

82. Emeis, C. A., Determination of Integrated Molar Extinction Coefficients for Infrared Absorption Bands of Pyridine Adsorbed on Solid Acid Catalysts. *Journal of Catalysis* **1993**, *141* (2), 347-354.
83. Momma, K.; Izumi, F., VESTA 3 for three-dimensional visualization of crystal, volumetric and morphology data. *Journal of Applied Crystallography* **2011**, *44* (6), 1272-1276.
84. Grazulis, S.; Chateigner, D.; Downs, R. T.; Yokochi, A. F. T.; Quiros, M.; Lutterotti, L.; Manakova, E.; Butkus, J.; Moeck, P.; Le Bail, A., Crystallography Open Database - an open-access collection of crystal structures. *Journal of Applied Crystallography* **2009**, *42* (4), 726-729.
85. Burattin, P.; Che, M.; Louis, C., Characterization of the Ni(II) Phase Formed on Silica Upon Deposition–Precipitation. *The Journal of Physical Chemistry B* **1997**, *101* (36), 7060-7074.
86. Chen, B.-H.; Chao, Z.-S.; He, H.; Huang, C.; Liu, Y.-J.; Yi, W.-J.; Wei, X.-L.; An, J.-F., Towards a full understanding of the nature of Ni(ii) species and hydroxyl groups over highly siliceous HZSM-5 zeolite supported nickel catalysts prepared by a deposition-precipitation method. *Dalton Transactions* **2016**, *45* (6), 2720-2739.
87. Jabbour, K.; El Hassan, N.; Davidson, A.; Casale, S.; Massiani, P., Factors affecting the long-term stability of mesoporous nickel-based catalysts in combined steam and dry reforming of methane. *Catalysis Science & Technology* **2016**, *6* (12), 4616-4631.
88. Horiguchi, J.; Kobayashi, Y.; Kobayashi, S.; Yamazaki, Y.; Omata, K.; Nagao, D.; Konno, M.; Yamada, M., Mesoporous NiO–Al₂O₃ catalyst for high pressure partial oxidation of methane to syngas. *Applied Catalysis A: General* **2011**, *392* (1–2), 86-92.
89. Barrio, V. L.; Arias, P. L.; Cambra, J. F.; Güemez, M. B.; Campos-Martin, J. M.; Pawelec, B.; Fierro, J. L. G., Evaluation of silica-alumina-supported nickel catalysts in dibenzothiophene hydrodesulphurisation. *Applied Catalysis A: General* **2003**, *248* (1–2), 211-225.
90. Barrio, V. L.; Arias, P. L.; Cambra, J. F.; Güemez, M. B.; Pawelec, B.; Fierro, J. L. G., Aromatics hydrogenation on silica–alumina supported palladium–nickel catalysts. *Applied Catalysis A: General* **2003**, *242* (1), 17-30.
91. Fang, K.; Ren, J.; Sun, Y., Effect of nickel precursors on the performance of Ni/AlMCM-41 catalysts for n-dodecane hydroconversion. *Journal of Molecular Catalysis A: Chemical* **2005**, *229* (1), 51-58.
92. Lewandowska, A.; Monteverdi, S.; Bettahar, M.; Ziolk, M., MCM-41 mesoporous molecular sieves supported nickel—physico-chemical properties and catalytic activity in hydrogenation of benzene. *Journal of Molecular Catalysis A: Chemical* **2002**, *188* (1), 85-95.

93. Bhat, R.; Babu, G. P.; Bhat, A. N., Nickel ion-exchanged zeolite-4A: reduction behaviour of nickel and structure stability. *Journal of the Chemical Society, Faraday Transactions* **1995**, *91* (21), 3983-3986.
94. Gamliel, D. P.; Baillie, B. P.; Augustine, E.; Hall, J.; Bollas, G. M.; Valla, J. A., Nickel impregnated mesoporous USY zeolites for hydrodeoxygenation of anisole. *Microporous and Mesoporous Materials* **2017**.
95. Andrei, R. D.; Popa, M. I.; Fajula, F.; Hulea, V., Heterogeneous oligomerization of ethylene over highly active and stable Ni-*Al*SBA-15 mesoporous catalysts. *Journal of Catalysis* **2015**, *323*, 76-84.
96. Wang, Z.; Jiang, Y.; Lafon, O.; Trébosc, J.; Duk Kim, K.; Stampfl, C.; Baiker, A.; Amoureux, J.-P.; Huang, J., Brønsted acid sites based on penta-coordinated aluminum species. *Nature Communications* **2016**, *7*, 13820.
97. Trombetta, M.; Busca, G.; Rossini, S.; Piccoli, V.; Cornaro, U.; Guercio, A.; Catani, R.; Willey, R. J., FT-IR Studies on Light Olefin Skeletal Isomerization Catalysis. *Journal of Catalysis* **1998**, *179* (2), 581-596.
98. Omegna, A.; van Bokhoven, J. A.; Prins, R., Flexible Aluminum Coordination in Alumino-Silicates. Structure of Zeolite H-USY and Amorphous Silica-Alumina. *The Journal of Physical Chemistry B* **2003**, *107* (34), 8854-8860.
99. Wouters, B. H.; Chen, T. H.; Grobet, P. J., Reversible Tetrahedral-Octahedral Framework Aluminum Transformation in Zeolite Y. *Journal of the American Chemical Society* **1998**, *120* (44), 11419-11425.
100. Parker, W. O. N.; Wegner, S., Aluminum in mesoporous silica-alumina. *Microporous and Mesoporous Materials* **2012**, *158* (Supplement C), 235-240.
101. Chen, T.-H.; Houthoofd, K.; Grobet, P. J., Toward the aluminum coordination in dealuminated mordenite and amorphous silica-alumina: A high resolution ²⁷Al MAS and MQ MAS NMR study. *Microporous and Mesoporous Materials* **2005**, *86* (1-3), 31-37.
102. Hensen, E. J. M.; Poduval, D. G.; Magusin, P. C. M. M.; Coumans, A. E.; Veen, J. A. R. v., Formation of acid sites in amorphous silica-alumina. *Journal of Catalysis* **2010**, *269* (1), 201-218.
103. Crépeau, G.; Montouillout, V.; Vimont, A.; Mariey, L.; Cseri, T.; Maugé, F., Nature, Structure and Strength of the Acidic Sites of Amorphous Silica Alumina: An IR and NMR Study. *The Journal of Physical Chemistry B* **2006**, *110* (31), 15172-15185.
104. Williams, M. F.; Fonfé, B.; Sievers, C.; Abraham, A.; van Bokhoven, J. A.; Jentys, A.; van Veen, J. A. R.; Lercher, J. A., Hydrogenation of tetralin on silica-alumina-supported Pt catalysts I. Physicochemical characterization of the catalytic materials. *Journal of Catalysis* **2007**, *251* (2), 485-496.

105. De Witte, B.; Grobet, P.; Uytterhoeven, J., Pentacoordinated aluminum in noncalcined amorphous aluminosilicates, prepared in alkaline and acid mediums. *The Journal of Physical Chemistry* **1995**, *99* (18), 6961-6965.
106. Farges, F.; Brown, G. E.; Petit, P.-E.; Munoz, M., Transition elements in water-bearing silicate glasses/melts. part I. a high-resolution and anharmonic analysis of Ni coordination environments in crystals, glasses, and melts. *Geochimica et Cosmochimica Acta* **2001**, *65* (10), 1665-1678.
107. Lyutin, V. I.; Tutov, A. G.; Ilyukhin, V. V.; Belov, N. V., Crystal structure of the antiferromagnetic K, Ni phosphate KNiPO₄. *Soviet Physics - Doklady* **1973**, *18* (1), 12-14.
108. Galois, L.; Calas, G., XANES and crystal field spectroscopy of five-coordinated Nickel(II) in potassium-nickel phosphate. *Materials Research Bulletin* **1993**, *28* (3), 221-228.
109. Colpas, G. J.; Maroney, M. J.; Bagyinka, C.; Kumar, M.; Willis, W. S.; Suib, S. L.; Mascharak, P. K.; Baidya, N., X-ray spectroscopic studies of nickel complexes, with application to the structure of nickel sites in hydrogenases. *Inorganic Chemistry* **1991**, *30* (5), 920-928.
110. Smith, T. A.; Penner-Hahn, J. E.; Berding, M. A.; Doniach, S.; Hodgson, K. O., Polarized x-ray absorption edge spectroscopy of single-crystal copper(II) complexes. *Journal of the American Chemical Society* **1985**, *107* (21), 5945-5955.
111. Bonneviot, L.; Olivier, D.; Che, M., Dimerization of olefins with nickel-surface complexes in X-type zeolite or on silica. *Journal of Molecular Catalysis* **1983**, *21* (1), 415-430.
112. Hadjiivanov, K.; Ivanova, E.; Klissurski, D., Site-specified and complex-specified formation of geminal species during adsorption of small molecules on cationic sites. *Catalysis Today* **2001**, *70* (1), 73-82.
113. Little, L.; Amberg, C. H., INFRARED SPECTRA OF CARBON MONOXIDE AND CARBON DIOXIDE ADSORBED ON CHROMIA-ALUMINA AND ON ALUMINA. *Canadian Journal of Chemistry* **1962**, *40* (10), 1997-2006.
114. Busca, G., Spectroscopic characterization of the acid properties of metal oxide catalysts. *Catalysis Today* **1998**, *41* (1-3), 191-206.
115. Cairon, O.; Chevreau, T.; Lavalley, J.-C., Brnsted acidity of extraframework debris in steamed Y zeolites from the FTIR study of CO adsorption. *Journal of the Chemical Society, Faraday Transactions* **1998**, *94* (19), 3039-3047.
116. Leydier, F.; Chizallet, C.; Costa, D.; Raybaud, P., CO adsorption on amorphous silica-alumina: electrostatic or Bronsted acidity probe? *Chemical Communications* **2012**, *48* (34), 4076-4078.

117. Henry, R.; Komurcu, M.; Ganjkhanlou, Y.; Brogaard, R. Y.; Lu, L.; Jens, K.-J.; Berlier, G.; Olsbye, U., Ethene oligomerization on nickel microporous and mesoporous-supported catalysts: Investigation of the active sites. *Catalysis Today* **2017**.
118. Jystad, A. M.; Biancardi, A.; Caricato, M., Simulations of Ammonia Adsorption for the Characterization of Acid Sites in Metal-Doped Amorphous Silicates. *The Journal of Physical Chemistry C* **2017**, *121* (40), 22258-22267.
119. Peri, J., Infrared study of adsorption of carbon dioxide, hydrogen chloride, and other molecules on “acid” sites on dry silica—alumina and γ -alumina¹. *The Journal of Physical Chemistry* **1966**, *70* (10), 3168-3179.
120. Hadjiivanov, K. I.; Vayssilov, G. N., Characterization of oxide surfaces and zeolites by carbon monoxide as an IR probe molecule. In *Advances in Catalysis*, Academic Press: 2002; Vol. Volume 47, pp 307-511.
121. Mihaylov, M.; Hadjiivanov, K.; Panayotov, D., FTIR mechanistic studies on the selective catalytic reduction of NO_x with methane over Ni-containing zeolites: comparison between NiY and Ni-ZSM-5. *Applied Catalysis B: Environmental* **2004**, *51* (1), 33-42.
122. Goursot, A.; Coq, B.; Fajula, F., Toward a molecular description of heterogeneous catalysis: transition metal ions in zeolites. *Journal of Catalysis* **2003**, *216* (1), 324-332.
123. Hartmann, M.; Kevan, L., Transition-Metal Ions in Aluminophosphate and Silicoaluminophosphate Molecular Sieves: Location, Interaction with Adsorbates and Catalytic Properties. *Chemical Reviews* **1999**, *99* (3), 635-664.
124. Klier, K., Transition-metal ions in zeolites: the perfect surface sites. *Langmuir* **1988**, *4* (1), 13-25.
125. Rice, M. J.; Chakraborty, A. K.; Bell, A. T., Site Availability and Competitive Siting of Divalent Metal Cations in ZSM-5. *Journal of Catalysis* **2000**, *194* (2), 278-285.
126. Mihaylov, M.; Hadjiivanov, K., FTIR Study of CO and NO Adsorption and Coadsorption on Ni-ZSM-5 and Ni/SiO₂. *Langmuir* **2002**, *18* (11), 4376-4383.
127. Zhao, B.; Ke, X.-K.; Bao, J.-H.; Wang, C.-L.; Dong, L.; Chen, Y.-W.; Chen, H.-L., Synthesis of Flower-Like NiO and Effects of Morphology on Its Catalytic Properties. *The Journal of Physical Chemistry C* **2009**, *113* (32), 14440-14447.
128. Garbarino, G.; Campodonico, S.; Perez, A. R.; Carnasciali, M. M.; Riani, P.; Finocchio, E.; Busca, G., Spectroscopic characterization of Ni/Al₂O₃ catalytic materials for the steam reforming of renewables. *Applied Catalysis A: General* **2013**, *452*, 163-173.
129. Hadjiivanov, K.; Mihaylov, M.; Klissurski, D.; Stefanov, P.; Abadjieva, N.; Vassileva, E.; Mintchev, L., Characterization of Ni/SiO₂ Catalysts Prepared by Successive Deposition and Reduction of Ni²⁺ Ions. *Journal of Catalysis* **1999**, *185* (2), 314-323.

130. Bordiga, S.; Garrone, E.; Lamberti, C.; Zecchina, A.; Arean, C. O.; Kazansky, V. B.; Kustov, L. M., Comparative IR-spectroscopic study of low-temperature H₂ and CO adsorption on Na zeolites. *Journal of the Chemical Society, Faraday Transactions* **1994**, *90* (21), 3367-3372.
131. Góra-Marek, K.; Glanowska, A.; Datka, J., Quantitative IR studies of the concentration of different nickel sites in NiZSM-5 zeolites. *Microporous and Mesoporous Materials* **2012**, *158*, 162-169.
132. Li, P.; Xiang, Y.; Grassian, V. H.; Larsen, S. C., CO Adsorption as a Probe of Acid Sites and the Electric Field in Alkaline Earth Exchanged Zeolite Beta Using FT-IR and ab Initio Quantum Calculations. *The Journal of Physical Chemistry B* **1999**, *103* (24), 5058-5062.
133. Busca, G.; Lorenzelli, V.; Sanchez Escribano, V., Preparation, solid-state characterization, and surface chemistry of high-surface-area nickel-aluminum (Ni_xAl_{2-2x}O_{3-2x}) mixed oxides. *Chemistry of Materials* **1992**, *4* (3), 595-605.
134. Beebe, T. P.; Gelin, P.; Yates, J. T., Infrared spectroscopic observations of surface bonding in physical adsorption: The physical adsorption of CO on SiO₂ surfaces. *Surface Science* **1984**, *148* (2), 526-550.
135. Tsyganenko, A. A.; Filimonov, V. N., Infrared spectra of surface hydroxyl groups and crystalline structure of oxides. *Journal of Molecular Structure* **1973**, *19*, 579-589.
136. Kermarec, M.; Carriat, J. Y.; Burattin, P.; Che, M.; Decarreau, A., FTIR Identification of the Supported Phases Produced in the Preparation of Silica-Supported Nickel Catalysts. *The Journal of Physical Chemistry* **1994**, *98* (46), 12008-12017.
137. Svelle, S.; Sommer, L.; Barbera, K.; Vennestrøm, P. N. R.; Olsbye, U.; Lillerud, K. P.; Bordiga, S.; Pan, Y.-H.; Beato, P., How defects and crystal morphology control the effects of desilication. *Catalysis Today* **2011**, *168* (1), 38-47.
138. Tarach, K.; Góra-Marek, K.; Tekla, J.; Brylewska, K.; Datka, J.; Mlekodaj, K.; Makowski, W.; Igualada López, M. C.; Martínez Triguero, J.; Rey, F., Catalytic cracking performance of alkaline-treated zeolite Beta in the terms of acid sites properties and their accessibility. *Journal of Catalysis* **2014**, *312*, 46-57.
139. Stepanov, A. G.; Luzgin, M. V.; Romannikov, V. N.; Sidelnikov, V. N.; Paukshtis, E. A., The Nature, Structure, and Composition of Adsorbed Hydrocarbon Products of Ambient Temperature Oligomerization of Ethylene on Acidic Zeolite H-ZSM-5. *Journal of Catalysis* **1998**, *178* (2), 466-477.
140. Bernauer, M.; Tabor, E.; Pashkova, V.; Kaucký, D.; Sobalík, Z.; Wichterlová, B.; Dedecek, J., Proton proximity – New key parameter controlling adsorption, desorption and activity in propene oligomerization over H-ZSM-5 zeolites. *Journal of Catalysis* **2016**, *344* (Supplement C), 157-172.

141. Arlman, E. J.; Cossee, P., Ziegler-Natta catalysis III. Stereospecific polymerization of propene with the catalyst system $\text{TiCl}_3 \cdot \text{AlEt}_3$. *Journal of Catalysis* **1964**, *3* (1), 99-104.
142. Cossee, P., On the reaction mechanism of the ethylene polymerization with heterogeneous ziegler-natta catalysts. *Tetrahedron Letters* **1960**, *1* (38), 12-16.
143. Cossee, P., The formation of isotactic polypropylene under the influence of ziegler-natta catalysts. *Tetrahedron Letters* **1960**, *1* (38), 17-21.
144. Cossee, P., Ziegler-Natta catalysis I. Mechanism of polymerization of α -olefins with Ziegler-Natta catalysts. *Journal of Catalysis* **1964**, *3* (1), 80-88.
145. Lepetit, C.; Che, M., Discussion on the Coordination of Ni^{2+} Ions to Lattice Oxygens in Calcined Faujasite-Type Zeolites Followed by Diffuse Reflectance Spectroscopy. *The Journal of Physical Chemistry* **1996**, *100* (8), 3137-3143.
146. Winkler, J. R.; Gray, H. B., Electronic Structures of Oxo-Metal Ions. In *Molecular Electronic Structures of Transition Metal Complexes I*, Mingos, D. M. P.; Day, P.; Dahl, J. P., Eds. Springer Berlin Heidelberg: Berlin, Heidelberg, 2012; pp 17-28.
147. Sarazen, M. L.; Iglesia, E., Stability of bound species during alkene reactions on solid acids. *Proceedings of the National Academy of Sciences* **2017**, *114* (20), E3900-E3908.
148. Louisfremea, W.; Paillaud, J.-L.; Porcher, F.; Perrin, E.; Onfroy, T.; Massiani, P.; Boutin, A.; Rotenberg, B., Cation Migration and Structural Deformations upon Dehydration of Nickel-Exchanged NaY Zeolite: A Combined Neutron Diffraction and Monte Carlo Study. *The Journal of Physical Chemistry C* **2016**, *120* (32), 18115-18125.
149. Corma, A.; Iborra, S., *Oligomerization of Alkenes*. John Wiley & Sons, Ltd: Hoboken, New Jersey, 2006; Vol. 4.
150. Souza, M. O. d.; Rodrigues, L. R.; Gauvin, R. M.; Souza, R. F. d.; Pastore, H. O.; Gengembr, L.; Ruiz, J. A. C.; Gallo, J. M. R.; Milanese, T. S.; Milani, M. A., Support effect in ethylene oligomerization mediated by heterogenizednickel catalysts. *Catalyst Communications* **2010**, *11*, 597-600.
151. Ruddy, D.; Baddour, F.; Pan, M.; Griffin, M.; Habas, S.; Yung, M.; Schaidle, J., Characterization and Stability Studies of Catalyst Support Materials. *FY15 Q3 progress milestone Internal publication*.
152. Lucy, A. R. Production of Middle Distillate Hydrocarbon Composition. 2014.
153. Air Liquide Gas Encyclopedia. <https://encyclopedia.airliquide.com/> (accessed March 7, 2018).
154. Awudza, J. A. M.; Tait, P. J. T., The “comonomer effect” in ethylene/ α -olefin copolymerization using homogeneous and silica-supported $\text{Cp}_2\text{ZrCl}_2/\text{MAO}$ catalyst systems: Some insights from the kinetics of polymerization, active center studies, and

- polymerization temperature. *Journal of Polymer Science Part A: Polymer Chemistry* **2008**, *46* (1), 267-277.
155. Maier, S. M.; Jentys, A.; Lercher, J. A., Steaming of Zeolite BEA and Its Effect on Acidity: A Comparative NMR and IR Spectroscopic Study. *The Journal of Physical Chemistry C* **2011**, *115* (16), 8005-8013.
 156. Kentgens, A. P. M., A practical guide to solid-state NMR of half-integer quadrupolar nuclei with some applications to disordered systems. *Geoderma* **1997**, *80* (3), 271-306.
 157. Beers, A. E. W.; van Bokhoven, J. A.; de Lathouder, K. M.; Kapteijn, F.; Moulijn, J. A., Optimization of zeolite Beta by steaming and acid leaching for the acylation of anisole with octanoic acid: a structure–activity relation. *Journal of Catalysis* **2003**, *218* (2), 239-248.
 158. Bhering, D. L.; Ramírez-Solís, A.; Mota, C. J. A., A Density Functional Theory Based Approach to Extraframework Aluminum Species in Zeolites. *The Journal of Physical Chemistry B* **2003**, *107* (18), 4342-4347.
 159. Benco, L.; Demuth, T.; Hafner, J.; Hutschka, F.; Toulhoat, H., Extraframework Aluminum Species in Zeolites: Ab Initio Molecular Dynamics Simulation of Gmelinite. *Journal of Catalysis* **2002**, *209* (2), 480-488.
 160. Biesinger, M. C.; Payne, B. P.; Lau, L. W. M.; Gerson, A.; Smart, R. S. C., X-ray photoelectron spectroscopic chemical state quantification of mixed nickel metal, oxide and hydroxide systems. *Surface and Interface Analysis* **2009**, *41* (4), 324-332.
 161. Li, C. Y.; Zhang, H. J.; Chen, Z. Q., Reaction between NiO and Al₂O₃ in NiO/ γ -Al₂O₃ catalysts probed by positronium atom. *Applied Surface Science* **2013**, *266*, 17-21.
 162. Park, J.; Regalbuto, J. R., A Simple, Accurate Determination of Oxide PZC and the Strong Buffering Effect of Oxide Surfaces at Incipient Wetness. *Journal of Colloid and Interface Science* **1995**, *175* (1), 239-252.
 163. Hao, X.; Quach, L.; Korah, J.; Spieker, W. A.; Regalbuto, J. R., The control of platinum impregnation by PZC alteration of oxides and carbon. *Journal of Molecular Catalysis A: Chemical* **2004**, *219* (1), 97-107.
 164. Jiao, L.; Zha, Y.; Hao, X.; Regalbuto, J. R., Simple, Scientific Syntheses with Common Catalyst Precursors. In *Studies in Surface Science and Catalysis*, Gaigneaux, E. M.; Devillers, M.; De Vos, D. E.; Hermans, S.; Jacobs, P. A.; Martens, J. A.; Ruiz, P., Eds. Elsevier: 2006; Vol. 162, pp 211-218.
 165. Gurrath, M.; Kuretzky, T.; Boehm, H. P.; Okhlopkova, L. B.; Lisitsyn, A. S.; Likholobov, V. A., Palladium catalysts on activated carbon supports: Influence of reduction temperature, origin of the support and pretreatments of the carbon surface. *Carbon* **2000**, *38* (8), 1241-1255.

166. Toba, M.; Tanaka, S.-i.; Niwa, S.-i.; Mizukami, F.; Koppány, Z.; Guzzi, L.; Cheah, K.-Y.; Tang, T.-S., Synthesis of alcohols and diols by hydrogenation of carboxylic acids and esters over Ru–Sn–Al₂O₃ catalysts. *Applied Catalysis A: General* **1999**, *189* (2), 243-250.
167. Wettstein, S. G.; Bond, J. Q.; Alonso, D. M.; Pham, H. N.; Datye, A. K.; Dumesic, J. A., RuSn bimetallic catalysts for selective hydrogenation of levulinic acid to γ -valerolactone. *Applied Catalysis B: Environmental* **2012**, *117-118*, 321-329.
168. Huang, S.-Y.; Chang, S.-M.; Yeh, C.-t., Characterization of Surface Composition of Platinum and Ruthenium Nanoalloys Dispersed on Active Carbon. *The Journal of Physical Chemistry B* **2006**, *110* (1), 234-239.
169. Dandekar, A.; Baker, R. T. K.; Vannice, M. A., Characterization of activated carbon, graphitized carbon fibers and synthetic diamond powder using TPD and DRIFTS. *Carbon* **1998**, *36* (12), 1821-1831.
170. Zhu, Z.; Lu, Z.; Li, B.; Guo, S., Characterization of bimetallic Ru-Sn supported catalysts and hydrogenation of 1,4-cyclohexanedicarboxylic acid. *Applied Catalysis A: General* **2006**, *302* (2), 208-214.
171. Mendes, M. J.; Santos, O. A. A.; Jordão, E.; Silva, A. M., Hydrogenation of oleic acid over ruthenium catalysts. *Applied Catalysis A: General* **2001**, *217* (1), 253-262.
172. Pouilloux, Y.; Autin, F.; Guimon, C.; Barrault, J., Hydrogenation of Fatty Esters over Ruthenium–Tin Catalysts; Characterization and Identification of Active Centers. *Journal of Catalysis* **1998**, *176* (1), 215-224.
173. Hara, Y.; Endou, K., The drastic effect of platinum on carbon-supported ruthenium-tin catalysts used for hydrogenation reactions of carboxylic acids. *Applied Catalysis A: General* **2003**, *239* (1), 181-195.
174. de Miguel, S. R.; Román-Martínez, M. C.; Jablonski, E. L.; Fierro, J. L. G.; Cazorla-Amorós, D.; Scelza, O. A., Characterization of Bimetallic PtSn Catalysts Supported on Purified and H₂O₂-Functionalized Carbons Used for Hydrogenation Reactions. *Journal of Catalysis* **1999**, *184* (2), 514-525.
175. Miller, J. T.; Schreier, M.; Kropf, A. J.; Regalbuto, J. R., A fundamental study of platinum tetraammine impregnation of silica: 2. The effect of method of preparation, loading, and calcination temperature on (reduced) particle size. *Journal of Catalysis* **2004**, *225* (1), 203-212.
176. Hao, X.; Barnes, S.; Regalbuto, J. R., A fundamental study of Pt impregnation of carbon: Adsorption equilibrium and particle synthesis. *Journal of Catalysis* **2011**, *279* (1), 48-65.
177. Vardon, D. R.; Franden, M. A.; Johnson, C. W.; Karp, E. M.; Guarnieri, M. T.; Linger, J. G.; Salm, M. J.; Strathmann, T. J.; Beckham, G. T., Adipic acid production from lignin. *Energy & Environmental Science* **2015**, *8* (2), 617-628.

178. Agirrezabal-Telleria, I.; Iglesia, E., Stabilization of active, selective, and regenerable Ni-based dimerization catalysts by condensation of ethene within ordered mesopores. *Journal of Catalysis* **2017**, *352*, 505-514.

APPENDIX A

PERMISSIONS

Permissions for use of Figure 1.3 and Figure 1.4 in Chapter 1 are provided under the terms of the Standard ACS *AuthorChoice* usage agreement given as follows:

SCOPE OF GRANT

ACS grants You non-exclusive and nontransferable permission to access and use this ACS article subject to the terms and conditions set forth in this Agreement.

PERMITTED USES

- a. For non-commercial research and education purposes only, You may access, download, copy, display and redistribute articles as well as adapt, translate, text and data mine content contained in articles, subject to the following conditions:
 - i. The authors' moral right to the integrity of their work under the Berne Convention (Article 6bis) is not compromised.
 - ii. Where content in the article is identified as belonging to a third party, it is your responsibility to ensure that any reuse complies with copyright policies of the owner.
 - iii. Copyright notices or the display of unique Digital Object Identifiers (DOI's), ACS or journal logos, bibliographic (e.g. authors, journal, article title, volume, issue, page numbers) or other references to ACS journal titles, web links, and any other journal-specific "branding" or notices that are included in the article or that are provided by the ACS with instructions that such should accompany its display, should not be removed or tampered with in any way. The display of ACS *AuthorChoice* or *ACS Editors' Choice* articles on non-ACS websites must be accompanied by prominently displayed links to the definitive published versions of those articles on the ACS

website.

iv. Any adaptations for non-commercial purposes must prominently link to the definitive published version on the ACS website and prominently display the statement: “This is an unofficial adaptation of an article that appeared in an ACS publication. ACS has not endorsed the content of this adaptation or the context of its use.”

v. Any translations for non-commercial purposes, for which a prior translation agreement with ACS has not been established, must prominently link to the definitive published version on the ACS website and prominently display the statement: “This is an unofficial translation of an article that appeared in an ACS publication. ACS has not endorsed the content of this translation or the context of its use.”

b. Each time You distribute this ACS article or an adaptation, ACS offers to the recipient a license to this ACS article on the same terms and conditions as the license granted to You under this License.

c. For permission to use ACS copyrighted articles beyond that permitted here, visit: <http://pubs.acs.org/copyright/permissions.html>.

PROHIBITED USES

a. Use of this ACS article for commercial purposes is prohibited. Examples of such prohibited commercial purposes include but are not limited to:

i. Copying or downloading of articles, or linking to such postings, for further distribution, sale or licensing, for a fee;

ii. Copying, downloading or posting by a site or service that incorporates advertising with such content;

- iii. The inclusion or incorporation of article content in other works or services (other than normal quotations with an appropriate citation) that is then available for sale or licensing, for a fee;
- iv. Use of articles or article content (other than normal quotations with appropriate citation) by a for-profit organizations for promotional purposes, whether for a fee or otherwise;
- v. Sale of translated versions of the article that have not been authorized by license or other permission from the ACS

TERMINATION

ACS reserves the right to limit, suspend, or terminate your access to and use of the ACS Publications Division website and/or all ACS articles immediately upon detecting a breach of this License.

COPYRIGHTS; OTHER INTELLECTUAL PROPERTY RIGHTS

Except as otherwise specifically noted, ACS is the owner of all right, title and interest in the content of this ACS article, including, without limitations, graphs, charts, tables illustrations, and copyrightable supporting information. This ACS article is protected under the Copyright Laws of the United States Codified in Title 17 of the U.S. Code and subject to the Universal Copyright Convention and the Berne Copyright Convention. You agree not to remove or obscure copyright notices. You acknowledge that You have no claim to ownership of any part of this ACS article or other proprietary information accessed under this Agreement.

The names “American Chemical Society,” “ACS” and the titles of the journals and other ACS products are trademarks of ACS.

DISCLAIMER OF WARRANTIES; LIMITATION OF LIABILITY

ACS warrants that it is entitled to grant this Agreement.

EXCEPT AS SET FORTH IN THE PRECEDING SENTENCE, ACS MAKES NO WARRANTY OR REPRESENTATION OF ANY KIND, EXPRESS OR IMPLIED, WITH RESPECT TO THIS ACS ARTICLE INCLUDING, BUT NOT LIMITED TO WARRANTIES AS TO THE ACCURACY OR COMPLETENESS OF THE ACS ARTICLE, ITS QUALITY, ORIGINALITY, SUITABILITY, SEARCHABILITY, OPERATION, PERFORMANCE, COMPLIANCE WITH ANY COMPUTATIONAL PROCESS, MERCHANTABILITY OR FITNESS FOR A PARTICULAR PURPOSE.

ACS SHALL NOT BE LIABLE FOR: EXEMPLARY, SPECIAL, INDIRECT, INCIDENTAL, CONSEQUENTIAL OR OTHER DAMAGES ARISING OUT OF OR IN CONNECTION WITH THE AGREEMENT GRANTED HEREUNDER, THE USE OR INABILITY TO USE ANY ACS PRODUCT, ACS'S PERFORMANCE UNDER THIS AGREEMENT, TERMINATION OF THIS AGREEMENT BY ACS OR THE LOSS OF DATA, BUSINESS OR GOODWILL EVEN IF ACS IS ADVISED OR AWARE OF THE POSSIBILITY OF SUCH DAMAGES. IN NO EVENT SHALL THE TOTAL AGGREGATE LIABILITY OF ACS OUT OF ANY BREACH OR TERMINATION OF THIS AGREEMENT EXCEED THE TOTAL AMOUNT PAID BY YOU TO ACS FOR ACCESS TO THIS ACS ARTICLE FOR THE CURRENT YEAR IN WHICH SUCH CLAIM, LOSS OR DAMAGE OCCURRED, WHETHER IN CONTRACT, TORT OR OTHERWISE, INCLUDING, WITHOUT LIMITATION, DUE TO NEGLIGENCE.

The foregoing limitations and exclusions of certain damages shall apply regardless of the success or effectiveness of other remedies. No claim may be made against ACS unless suit is filed within one (1) year after the event giving rise to the claim.

GENERAL

This Agreement sets forth the entire understanding of the Parties. The validity, construction and performance of this Agreement shall be governed by and construed in accordance with the laws of the District of Columbia, USA without reference to its conflicts of laws principles. You acknowledge that the delivery of the ACS article will occur in the District of Columbia, USA. You shall pay any taxes lawfully due from it, other than taxes on ACS's net income, arising out of your use of this ACS article and/or other rights granted under this Agreement. You may not assign or transfer its rights under this Agreement without the express written consent of ACS.

ACCEPTANCE

You warrant that You have read, understand, and accept the terms and conditions of this Agreement. ACS reserves the right to modify this Agreement at any time by posting the modified terms and conditions on the ACS Publications Web site. Any use of this ACS article after such posting shall constitute acceptance of the terms and conditions as modified.

Permission for use of Figure 1.6 in Chapter 1 and Figure 3.1 in Chapter 3 is given as follows:

This Agreement between Martin J Menart ("You") and Elsevier ("Elsevier") consists of your license details and the terms and conditions provided by Elsevier and Copyright Clearance Center.

License Number	4325730426884
License date	Apr 11, 2018
Licensed Content Publisher	Elsevier
Licensed Content Publication	Catalysis Communications
Licensed Content Title	Support effect in ethylene oligomerization mediated by heterogenized nickel catalysts
Licensed Content Author	Michèle O. de Souza, Larissa R. Rodrigues, Régis M. Gauvin, Roberto F. de Souza, Heloise O. Pastore, Léon Gengembre, Juan A.C. Ruiz, Jean Marcel R. Gallo, Thiago S. Milanesi, Marcéo A. Milani
Licensed Content Date	Mar 10, 2010
Licensed Content Volume	11
Licensed Content Issue	7
Licensed Content Pages	4
Start Page	597
End Page	600
Type of Use	reuse in a thesis/dissertation
Portion	figures/tables/illustrations
Number of figures/tables/illustrations	1
Format	both print and electronic
Are you the author of this Elsevier article?	No
Will you be translating?	No
Original figure numbers	Figure 3
Title of your thesis/dissertation	THE ROLE OF ACIDITY IN HETEROGENEOUS NICKEL CATALYSTS FOR THE OLIGOMERIZATION OF LIGHT OLEFINS
Expected completion date	May 2018
Estimated size (number of pages)	180

Permission for use of Figure 1.7 in Chapter 1 is given as follows:

This Agreement between Martin J Menart ("You") and Elsevier ("Elsevier") consists of your license details and the terms and conditions provided by Elsevier and Copyright Clearance Center.

License Number	4325730511349
License date	Apr 11, 2018
Licensed Content Publisher	Elsevier
Licensed Content Publication	Applied Catalysis A: General
Licensed Content Title	NiMCM-36 and NiMCM-22 catalysts for the ethylene oligomerization: Effect of zeolite texture and nickel cations/acid sites ratio
Licensed Content Author	Michael Lallemand,Oana Alice Rusu,Emil Dumitriu,Annie Finiels,François Fajula,Vasile Hulea
Licensed Content Date	Apr 1, 2008
Licensed Content Volume	338
Licensed Content Issue	1-2
Licensed Content Pages	7
Start Page	37
End Page	43
Type of Use	reuse in a thesis/dissertation
Intended publisher of new work	other
Portion	figures/tables/illustrations
Number of figures/tables/illustrations	1
Format	both print and electronic
Are you the author of this Elsevier article?	No
Will you be translating?	No
Original figure numbers	Scheme 1
Title of your thesis/dissertation	THE ROLE OF ACIDITY IN HETEROGENEOUS NICKEL CATALYSTS FOR THE OLIGOMERIZATION OF LIGHT OLEFINS
Expected completion date	May 2018
Estimated size (number of pages)	180

Permission for use of Figure 1.11 in Chapter 1 is given as follows:

Copyright Clearance Center RightsLink®

Home Account Info Help

ACS Publications
Most Trusted. Most Cited. Most Read.

Title: Ethene Oligomerization in Ni-Containing Zeolites: Theoretical Discrimination of Reaction Mechanisms

Author: Rasmus Y. Brogaard, Unni Olsbye

Publication: ACS Catalysis

Publisher: American Chemical Society

Date: Feb 1, 2016

Copyright © 2016, American Chemical Society

Logged in as:
Martin Menart
LOGOUT

PERMISSION/LICENSE IS GRANTED FOR YOUR ORDER AT NO CHARGE

This type of permission/license, instead of the standard Terms & Conditions, is sent to you because no fee is being charged for your order. Please note the following:

- Permission is granted for your request in both print and electronic formats, and translations.
- If figures and/or tables were requested, they may be adapted or used in part.
- Please print this page for your records and send a copy of it to your publisher/graduate school.
- Appropriate credit for the requested material should be given as follows: "Reprinted (adapted) with permission from (COMPLETE REFERENCE CITATION). Copyright (YEAR) American Chemical Society." Insert appropriate information in place of the capitalized words.
- One-time permission is granted only for the use specified in your request. No additional uses are granted (such as derivative works or other editions). For any other uses, please submit a new request.

If credit is given to another source for the material you requested, permission must be obtained from that source.

BACK

CLOSE WINDOW

Permission for use of Figure 1.12 in Chapter 1 is given as follows:

This Agreement between Martin J Menart ("You") and Elsevier ("Elsevier") consists of your license details and the terms and conditions provided by Elsevier and Copyright Clearance Center.

License Number	4325731111654
License date	Apr 11, 2018
Licensed Content Publisher	Elsevier
Licensed Content Publication	Catalysis Today
Licensed Content Title	Studies of a new alkene oligomerization catalyst derived from nickel sulfate
Licensed Content Author	Tianxi Cai
Licensed Content Date	Jun 1, 1999
Licensed Content Volume	51
Licensed Content Issue	1
Licensed Content Pages	8
Start Page	153
End Page	160
Type of Use	reuse in a thesis/dissertation
Intended publisher of new work	other
Portion	figures/tables/illustrations
Number of figures/tables/illustrations	1
Format	both print and electronic
Are you the author of this Elsevier article?	No
Will you be translating?	No
Original figure numbers	Fig. 2
Title of your thesis/dissertation	THE ROLE OF ACIDITY IN HETEROGENEOUS NICKEL CATALYSTS FOR THE OLIGOMERIZATION OF LIGHT OLEFINS
Expected completion date	May 2018
Estimated size (number of pages)	180

Permission for use of Figure 1.13 in Chapter 1 is given as follows:



RightsLink®

Home

Account
Info

Help



ACS Publications
Most Trusted. Most Cited. Most Read.

Title: Effect of Pore Size and Nickel Content of Ni-MCM-41 on Catalytic Activity for Ethene Dimerization and Local Structures of Nickel Ions
Author: Masashi Tanaka, Atsushi Itadani, Yasushige Kuroda, et al
Publication: The Journal of Physical Chemistry C
Publisher: American Chemical Society
Date: Mar 1, 2012
Copyright © 2012, American Chemical Society

Logged in as:
Martin Menart

LOGOUT

PERMISSION/LICENSE IS GRANTED FOR YOUR ORDER AT NO CHARGE

This type of permission/license, instead of the standard Terms & Conditions, is sent to you because no fee is being charged for your order. Please note the following:

- Permission is granted for your request in both print and electronic formats, and translations.
- If figures and/or tables were requested, they may be adapted or used in part.
- Please print this page for your records and send a copy of it to your publisher/graduate school.
- Appropriate credit for the requested material should be given as follows: "Reprinted (adapted) with permission from (COMPLETE REFERENCE CITATION). Copyright (YEAR) American Chemical Society." Insert appropriate information in place of the capitalized words.
- One-time permission is granted only for the use specified in your request. No additional uses are granted (such as derivative works or other editions). For any other uses, please submit a new request.

If credit is given to another source for the material you requested, permission must be obtained from that source.

BACK

CLOSE WINDOW

Permissions from co-authors from parts of papers reprinted in Chapter 4 are as follows:

 **Vardon, Derek** Apr 8 (1 day ago) ☆  
to me ▾

I, Derek Vardon, hereby authorize Martin J. Menart to use any part or all of DOI: 10.1021/acscatal.7b02015 in his published thesis.

 **Vorotnikov, Vassili** Apr 8 (1 day ago) ☆  
to me ▾

I, Vassili Vorotnikov, hereby authorize Martin J. Menart to use any part or all of DOI: 10.1021/acscatal.7b02015 in his published thesis.

 **Settle, Amy** 2:26 PM (21 hours ago) ☆  
to me ▾

I, Amy Settle, hereby authorize Martin J. Menart to use any part or all of DOI: 10.1021/acscatal.7b02015 in his published thesis.

 **Wood, Kevin** 6:42 AM (5 hours ago) ☆  
to me ▾

I, Kevin N. Wood, hereby authorize Martin J. Menart to use any part or all of DOI: 10.1021/acscatal.7b02015 in his published thesis.

 **Kathleen Moyer** 9:25 AM (2 hours ago) ☆  
to me ▾

Hi Martin,

I, Kate Moyer, hereby authorize Martin J. Menart to use any part or all of DOI: 10.1021/acscatal.7b02015 in his published thesis.

 **Cleveland, Nicholas** 10:05 AM (2 hours ago) ☆  
to me ▾

I, Nicholas Cleveland, hereby authorize Martin J. Menart to use any part or all of DOI: 10.1021/acscatal.7b02015 in his published thesis.

 **Beckham, Gregg** Apr 8 (1 day ago) ☆  
to me ▾

Works for me, Martin, on both this and the RuSn paper.
-gregg

Permissions from co-authors from parts of papers reprinted in Chapter 5 are as follows:

 **Vardon, Derek** Apr 8 (1 day ago) ☆  
to me ▾

Congrats on your defense!

I, Derek Vardon, hereby authorize Martin J. Menart to use any part or all of DOI:
10.1039/c5gc02844b in his published thesis.

 **Settle, Amy** 2:25 PM (21 hours ago) ☆  
to me ▾

I, Amy Settle, hereby authorize Martin J. Menart to use any part or all of DOI:
10.1039/c5gc02844b in his published thesis.

 **Beckham, Gregg** Apr 8 (1 day ago) ☆  
to me ▾

Works for me, Martin, on both this and the RuSn paper.
-gregg

 **Salvachua, Davinia** 7:24 AM (4 hours ago) ☆  
to me ▾

Hi Martin,

I, Davinia Salvachua, hereby authorize Martin J. Menart to use any part or all of DOI:
10.1039/c5gc02844b in his published thesis

 **Cleveland, Nicholas** 10:05 AM (2 hours ago) ☆  
to me ▾

I, Nicholas Cleveland, hereby authorize Martin J. Menart to use any part or all of DOI:
10.1039/c5gc02844b in his published thesis.

 **Johnson, Christopher** 9:50 AM (2 hours ago) ☆  
to me ▾

I, Christopher Johnson, hereby authorize Martin J. Menart to use any part or all of DOI:
10.1039/c5gc02844b in his published thesis.

 **Rorrer, Nicholas** 10:40 AM (1 hour ago) ☆  
to me ▾

To Whom it May Concern,

I, Nicholas A. Rorrer, hereby authorize Martin J. Menart to use any part or all of DOI: 10.1039/c5gc02844b in his published thesis.

 **Ciesielski, Peter** 8:48 AM (3 hours ago) ☆  
to me ▾

Hi Martin,

This is fine with me, although I don't know that can give final approval on this.

Either way, here is the official statement in the format you requested:

I, Peter Ciesielski, hereby authorize Martin J. Menart to use any part or all of DOI: 10.1039/c5gc02844b in his published thesis.

Permissions from co-authors from parts of papers reprinted in Chapter 6 are as follows:

 **Malcolm Davidson** Apr 5 (4 days ago) ☆  
to me ▾

I, Malcolm Davidson, hereby authorize Martin J. Menart to use any part or all of DOI: 10.1021/acssuschemeng.7b00817 in his published thesis.

...

 **Mengze Xu** Apr 5 (4 days ago) ☆  
to me ▾

I, Mengze Xu, hereby authorize Martin J. Menart to use any part or all of DOI: 10.1021/acssuschemeng.7b00817 in his published thesis.

...

 **Nimlos, Mark** Apr 5 (4 days ago) ☆  
to me ▾

I, Mark Nimlos, hereby authorize Martin J. Menart to use any part or all of DOI: 10.1021/acssuschemeng.7b00817 in his published thesis.

 **Mukarakate, Calvin** Apr 6 (3 days ago) ☆  
to me ▾

Dear Martin,

I, Calvin Mukarakate, hereby authorize Martin J. Menart to use any part or all of DOI: 10.1021/acssuschemeng.7b00817 in his published thesis.

 **lisa, Kristiina**

Apr 6 (3 days ago) ☆

to me ▾

I, Kristiina lisa, hereby authorize Martin J. Menart to use any part or all of DOI: 10.1021/acssuschemeng.7b00817 in his published thesis.

 **Robichaud, David**

Apr 5 (4 days ago) ☆

to me ▾

I, David Robichaud, hereby authorize Martin J. Menart to use any part or all of DOI: 10.1021/acssuschemeng.7b00817 in his published thesis.

Permission from publisher for use of parts of papers in Chapter 4 is as follows:



The screenshot shows the RightsLink interface. At the top left is the Copyright Clearance Center logo. To its right is the RightsLink logo. Further right are navigation buttons for Home, Create Account, and Help. Below the logo is the ACS Publications logo with the tagline "Most Trusted. Most Cited. Most Read." The main content area displays the following information:

Title:	Ru-Sn/AC for the Aqueous-Phase Reduction of Succinic Acid to 1,4-Butanediol under Continuous Process Conditions
Author:	Derek R. Vardon, Amy E. Settle, Vassili Vorotnikov, et al
Publication:	ACS Catalysis
Publisher:	American Chemical Society
Date:	Sep 1, 2017

Below the table is the copyright notice: Copyright © 2017, American Chemical Society.

On the right side of the screenshot, there is a "LOGIN" button and a text box that reads: "If you're a copyright.com user, you can login to RightsLink using your copyright.com credentials. Already a RightsLink user or want to learn more?"

PERMISSION/LICENSE IS GRANTED FOR YOUR ORDER AT NO CHARGE

This type of permission/license, instead of the standard Terms & Conditions, is sent to you because no fee is being charged for your order. Please note the following:

- Permission is granted for your request in both print and electronic formats, and translations.
- If figures and/or tables were requested, they may be adapted or used in part.
- Please print this page for your records and send a copy of it to your publisher/graduate school.
- Appropriate credit for the requested material should be given as follows: "Reprinted (adapted) with permission from (COMPLETE REFERENCE CITATION). Copyright (YEAR) American Chemical Society." Insert appropriate information in place of the capitalized words.
- One-time permission is granted only for the use specified in your request. No additional uses are granted (such as derivative works or other editions). For any other uses, please submit a new request.

[BACK](#)

[CLOSE WINDOW](#)

Copyright © 2018 Copyright Clearance Center, Inc. All Rights Reserved. [Privacy statement](#). [Terms and Conditions](#). Comments? We would like to hear from you. E-mail us at customercare@copyright.com

Permission from publisher for use of parts of papers in Chapter 5 is as follows:

Re-use permission requests

Material published by the Royal Society of Chemistry and other publishers is subject to all applicable copyright, database protection, and other rights. Therefore, for any publication, whether printed or electronic, permission must be obtained to use material for which the author(s) does not already own the copyright. This material may be, for example, a figure, diagram, table, photo or some other image.

Author reusing their own work published by the Royal Society of Chemistry

You do not need to request permission to reuse your own figures, diagrams, etc, that were originally published in a Royal Society of Chemistry publication. However, permission should be requested for use of the whole article or chapter except if reusing it in a thesis. If you are including an article or book chapter published by us in your thesis please ensure that your co-authors are aware of this.

Reuse of material that was published originally by the Royal Society of Chemistry must be accompanied by the appropriate acknowledgement of the publication. The form of the acknowledgement is dependent on the journal in which it was published originally, as detailed in 'Acknowledgements'.

Permission from publisher for use of parts of papers in Chapter 6 is as follows:



The screenshot shows the Copyright Clearance Center RightsLink interface. At the top left is the Copyright Clearance Center logo. To its right is the RightsLink logo. Further right are navigation buttons for Home, Create Account, and Help. On the far right is a chat bubble icon. Below the logos is the ACS Publications logo with the tagline "Most Trusted. Most Cited. Most Read." The main content area displays the following information:

Title: Deactivation of Multilayered MFI Nanosheet Zeolite during Upgrading of Biomass Pyrolysis Vapors

Author: Mengze Xu, Calvin Mukarakate, Kristiina Iisa, et al

Publication: ACS Sustainable Chemistry & Engineering

Publisher: American Chemical Society

Date: Jun 1, 2017

Copyright © 2017, American Chemical Society

On the right side of the interface, there is a LOGIN button and a text box that reads: "If you're a copyright.com user, you can login to RightsLink using your copyright.com credentials. Already a RightsLink user or want to learn more?"

PERMISSION/LICENSE IS GRANTED FOR YOUR ORDER AT NO CHARGE

This type of permission/license, instead of the standard Terms & Conditions, is sent to you because no fee is being charged for your order. Please note the following:

- Permission is granted for your request in both print and electronic formats, and translations.
- If figures and/or tables were requested, they may be adapted or used in part.
- Please print this page for your records and send a copy of it to your publisher/graduate school.
- Appropriate credit for the requested material should be given as follows: "Reprinted (adapted) with permission from (COMPLETE REFERENCE CITATION). Copyright (YEAR) American Chemical Society." Insert appropriate information in place of the capitalized words.
- One-time permission is granted only for the use specified in your request. No additional uses are granted (such as derivative works or other editions). For any other uses, please submit a new request.

BACK

CLOSE WINDOW

Copyright © 2018 Copyright Clearance Center, Inc. All Rights Reserved. [Privacy statement](#). [Terms and Conditions](#). Comments? We would like to hear from you. E-mail us at customercare@copyright.com